UNIVERSITY OF CALIFORNIA,
IRVINE

Advances in multiphoton microscopy for non-invasive assessment of human skin biology and disease

DISSERTATION

submitted in partial satisfaction of the requirements for the degree of

DOCTOR OF PHILOSOPHY

in Materials Science and Engineering

by

Griffin Lentsch

Dissertation Committee:
Professor Vasan Venugopalan, Chair
Professor Emeritus Bruce J. Tromberg
Associate Professor Allon I. Hochbaum

2021

DEDICATION

To my parents Melody and Richard, and sister Samantha- you have been there for me from the beginning and made me into who I am.

And to my wife Katelyn- your unrelenting love and support means more to me than you know.

TABLE OF CONTENTS

LIST OF FIGURES

LIST OF TABLES

ACKNOWLEDGEMENTS

I thank my Ph.D. dissertation committee members: Professor Vasan Venugopalan, Professor Bruce J. Tromberg, and Professor Allon I. Hochbaum, and my advancement committee members: Professor Eric O. Potma, and Professor Regina Ragan. Your feedback and direction on my dissertation research at many steps along the way was instrumental and much appreciated.

I would also like to express my deepest gratitude to Dr. Mihaela Balu, my mentor for all of my research at the Beckman Laser Institute. I feel extremely fortunate to have ended up in your lab, and without your leadership, my passion for science would not be what it is today. Thank you for the countless hours of discussion and guidance. You are an inspiration and role model to me, and I am very lucky I was able to learn from you.

Thank you to the many current and former mentors and colleagues at UC Irvine that I had the opportunity to study under and collaborate with, including: Dr. Tatiana Krasieva, Dr. Anthony Durkin, Dr. Gordon Kennedy, Dr. Thomas O'Sullivan, Dr. Michael Ghijsen, Dr. Inga Saknite, and Dr. Sanghoon Lee. Your expertise made me into a better scientist.

I would like to acknowledge the current and former Nonlinear Optical Microscopy Lab members at the Beckman Laser Institute: Dr. Alexander Fast, Amanda Durkin, Dr. Kristina Shrestha, Joshua Williams, and Dr. Juvinch Viscente. Lab meetings with you allowed me to refine my research and everyday discussions sharpened my mind.

Thank you to my collaborators at Tufts University, who contributed enormously to the research presented in Chapter 2: Dr. Irene Georgakoudi, Craig Mizzoni, and Christopher Polleys.

Thank you to Dr. Karsten Konig for allowing me to use the MPTflex, the instrument that generated much of the data found in this dissertation.

I would like to thank the many members of the UC Irvine Dermatology Department that I was able to learn from and collaborate with, including: Dr. Anand Ganesan, Dr. Kristen Kelly, Dr. Christopher B. Zachary, Dr. Janellen Smith, Dr. Natasha Mesinkovska, Dr. Patrick Lee, Dr. Kenneth Linden, Dr. Ronald Harris, Dr. Jessica Shiu, Dr. Pezhman Mobasher, and Dr. Manuel Valdebran. I learned more about skin biology and dermatology from these Doctors than I could have imagined.

A huge thank you goes out to the many friends I have made in my time at UCI. Especially the basketball squad that I played with on many mornings and evenings. Thank you for pushing me to stay in shape through the years. Specifically, Christian Crouzet, Ben Lertsakdadet, Wesley Moy, Justin Moy, Robert Wilson, Sarkis Daglian, Hector Limon, Lee Swindlehurst, Edwin Amenta, Janahan Arulmoli, Drew Bailey, Shauhin Talesh, and David Lutman, who were on the court consistently with me.

I thank Jon Wiley and Sons for permission to include chapter 4 of my dissertation, which was originally published in Pigment Cell and Melanoma Research.

Financial support was provided by: the NSF UCI Biophotonics across Energy, Space, and Time (BEST), Interdisciplinary Graduate Education and Research Traineeship (IGERT), the NIH/NCI/NIBIB (R01EB026705, R01CA19546), and Unilever (UNI202090).

Lastly, I would like to thank my family. My parents Melody and Richard, my sister Samantha, my wife Katelyn, and my father and mother-in-law Lori and Robert Kampa. Thank you for believing in me and caring for me in everything I do.

VITA

Griffin Lentsch

2013	B.A. in General Science – Biology, Grinnell College
2015	M.S in Materials Science and Engineering, University of California, Irvine
2021	Ph.D. in Materials Science and Engineering, University of California, Irvine

PUBLICATIONS

Lentsch, G, Valdebran, M, Saknite, I, Smith, J, Linden, K, König, K, Barr, RJ, Harris, RM, Tromberg, BJ, Ganesan, AK, Zachary, CB, Kelly, KM, Balu, M, "Non-invasive optical biopsy by multiphoton microscopy identifies the live morphology of common melanocytic nevi," Pigment Cell and Melanoma Research, 33: 869-877, 2020.

Lentsch, G, Balu, M, Williams, J, Lee, S, Harris, RM, Koenig, K, Tromberg, BJ, Nair, N, Santhanam, U, Misra, M, "In vivo multiphoton microscopy imaging of melasma," Pigment Cell and Melanoma Research, 32: 403– 411, 2019.

Lentsch, G, Balu, M, Koenig, K, Tromberg, BJ, Zachary, CB, Smith, J, "In vivo multiphoton microscopy of scabies," JAAD Case Reports, 4(10), 2018.

Mobasher, P, Shiu, J, Lentsch, G, & Ganesan, AK, Comparing the Efficacy of 2 Different Harvesting Techniques for Melanocyte Keratinocyte Transplantation in Vitiligo, Dermatologic Surgery, 47(5), 732-733, 2021

Mehrabi, JN, Baugh, EG, Fast, A, Lentsch, G, Balu, M, Lee, BL, Kelly, KM, "A Clinical Perspective on the Automated Analysis of Reflectance Confocal Microscopy in Dermatology," Lasers In Surgery And Medicine, 2021.

Fast A, Lal A, Durkin AF, Lentsch G, Harris RM, Zachary CB, Ganesan AK, Balu M. Fast, large area multiphoton exoscope (FLAME) for macroscopic imaging with microscopic resolution of human skin. Sci Rep. 10(1), 2020.

Mehrabi JN, Doong J, Lentsch G, Mesinkovska N. Imaging of in vivo pseudoxanthoma elasticum via multiphoton microscopy and optical coherence tomography. JAAD Case Rep. 6(8):702-704, 2020.

Ghijsen, M, Lentsch, G, Gioux, S, Brenner, M, Durkin, A J, Choi, B, Tromberg, BJ, "Quantitative real-time optical imaging of the tissue metabolic rate of oxygen consumption," J. Biomed Opt, 23(3), 2018.

Lin, J, Saknite, I , Valdebran, M , Balu, M, Lentsch, G, Williams, J, Koenig, K, Tromberg, BJ, Atanaskova Mesinkovska, N, "Feature characterization of scarring and non-scarring types of alopecia by multiphoton microscopy," Lasers Surg Med, 2018.

Verdel, N, Lentsch, G, Balu, M, Tromberg, BJ, Majaron, B, "Noninvasive assessment of skin structure by combined photothermal radiometry and optical spectroscopy: coregistration with multiphoton microscopy," Applied Optics, 57(18), 2018.

Balu, M, Lentsch, G, Korta, DZ, Koenig, K, Kelly, KM, Tromberg, BJ, Zachary, CB, "In vivo multiphoton-microscopy of picosecond-laser-induced optical breakdown in human skin," Lasers Surg Med, 49(6), 555–562, 2017.

Kennedy, GT, Lentsch, G, Trieu, B, Ponticorvo, A, Saager, RB, Durkin, AJ, "Solid tissue simulating phantoms having absorption at 970 nm for diffuse optics," J Biomed Opt., 22, 2017.

CONFERENCE PRESENTATIONS

Lentsch, G, et al., (2021, March), "In-vivo optical microscopy and single cell transcriptomics approaches provide insights into therapeutic response of vitiligo" Presented virtually at the annual meeting of the SPIE Photonics West Conference, San Francisco, CA.

Lentsch, G, Mobasher, P, Mizzoni, C, Koenig, K, Tromberg, BJ, Georgakoudi, I, Ganesan, AG, Balu, M, (2020, January), "In vivo optical imaging of vitiligo skin grafting treatment using multiphoton microscopy and reflectance confocal microscopy" Presented at the annual meeting of the SPIE Photonics West Conference, San Francisco, CA.

Lentsch, G, Balu, M, Koenig, K, Seongjin, J, Tromberg, BJ, Ganesan, AG (2019, January), “In vivo multiphoton microscopy imaging of vitiligo” Presented at the annual meeting of the SPIE Photonics West Conference, San Francisco, CA.

Lentsch, G, Balu, M, Williams, J, Lee, S, Harris, RM, Koenig, K, Tromberg, BJ, Nair, N, Santhanam, U, Misra, M (2018, January), “In vivo multiphoton microscopy imaging of melasma’” Presented at the annual meeting of the SPIE Photonics West Conference, San Francisco, CA.

ABSTRACT OF THE DISSERTATION

Advances in multiphoton microscopy for non-invasive assessment of human skin biology and disease

by

Griffin Lentsch

Doctor of Philosophy in Materials Science and Engineering

University of California, Irvine, 2021

Professor Vasan Venugopalan, Chair

Human skin is a highly complex and dynamic biological organ providing many critical functions for the human body. Thus, non-invasive and non-destructive technologies capable of providing multi-scale visualization of human skin with subcellular resolution would provide a means for robust characterization of skin structure and function. Recent advances in optical imaging technologies, such as multiphoton microscopy (MPM), have enhanced the feasibility of these approaches for clinical skin imaging. MPM allows for real time, *in vivo*, non-invasive, label-free imaging with sub-micrometer resolution and molecular contrast. In this work, we have used a commercial clinical MPM device to address critical unmet needs in skin biology, skin disease, and dermatology. Specifically, we used MPM, reflectance confocal microscopy, and single cell transcriptomics, to provide insights into the basic understanding of the biology of vitiligo and therapeutic response. Other applications included a characterization of benign melanocytic nevi in order to understand the specific morphology related to the evolution towards malignant melanoma, a cancer of the melanocytes; and an assessment of the biological hallmarks of melasma, a skin disorder associated with hyperpigmentation. Finally, based on the studies

performed in this work, we identified and addressed technical limitations of the commercial MPM instrument related to limited scanning area and speed. Preliminary data on the performance of an MPM imaging platform, recently developed in our lab, demonstrate the ability of this new device to provide stable *in vivo* images of skin over macroscopic spatial scales with microscopic resolution and enhanced molecular contrast. This advanced imaging tool, highly optimized for efficient skin imaging, is a promising instrument that facilitates further understanding of the microscopic and molecular processes that underlie skin biology.

1. Introduction

1.1 Background and Motivation

Materials science is the investigation of the properties of a material to understand its underlying structure and how that structure relates to its functionality. The study of materials relies on the ability to accurately characterize and quantify the structural and functional properties of a material during normal performance, as well as post failure. In the case of biological materials, a complete view of the behavior of the material necessitates a robust qualitative and quantitative analysis while the material is in its natural state, such that its properties are not affected by the analysis. The work described in this dissertation focuses on studying human skin as a biological material. Recent advances in optical imaging technologies have made possible studying this type of material in its native environment, such that its morphological and functional properties are not affected through processing.

Human skin creates a dynamic barrier between the body's internal organs and external threats, keeping harmful chemicals and bacteria out, and water in, while at the same time acting as a sensor to keep the brain informed of its surroundings. As a highly complex biological material, it requires multi-scale investigation to obtain a full picture of the structure and function required to maintain homeostasis. Direct access to skin from the outside world allows for the use of real time, *in vivo*, non-invasive, label-free optical technologies to address critical needs in skin biology, clinical research, and potentially in clinical practice of dermatology. One such technology, multiphoton microscopy (MPM), provides the above mentioned characteristics, in addition to sub-

micrometer resolution and molecular contrast. The contrast in MPM images of skin is provided by signals generated through light-tissue interactions. The images are formed by raster-scanning focused laser light on the tissue and detecting the light generated from different molecular components in the tissue through their interaction with the laser light. In skin, several endogenous molecular components can be visualized through this interaction without any labeling (staining) required, such as keratin, melanin and co-enzymes in the cells, and elastin and collagen in the dermis.

The ability of MPM to generate high-resolution 3D maps of specific tissue molecular compounds led to its widespread use in biomedical applications. However due to their high complexity and cost, microscopes based on this technology have been primarily used in research labs to drive discovery in cellular and pre-clinical animal models. Recently, innovative designs and engineering advances allowed the development of compact, portable MPM imaging platforms for clinical imaging. The goal of this research is to use the *in vivo* MPM imaging technology to study human skin as a biological material in order to advance our understanding of basic skin biology and disease, and to evaluate the potential of this technology to be utilized at the bedside as a clinical imaging tool for non-invasive skin assessment. Specifically, this research is focused in two main directions. The first is to apply existing optical technologies in clinical research applications to improve our understanding of skin biology and disease, as well as enhance the accuracy of non-invasive early diagnosis of skin conditions. The second direction is the development of innovative ways to design, build, implement, and test opto-mechanical components of a new MPM clinical platform to enhance performance and molecular sensitivity.

The outstanding questions addressed in this work include: 1) can *in vivo* MPM imaging answer fundamental questions about human skin functionality in the context of various

conditions/diseases? 2) Can MPM be used practically in clinic to enhance diagnostic accuracy and early detection of skin conditions/diseases? 3) Can MPM be used practically in dermatology to gain a better understanding of therapy response and for monitoring treatment effects? 4) Can MPM technology performance be improved through innovative engineering to enhance imaging contrast, scanning efficiency and speed in order to accelerate clinical translation?

An imaging tool that can be used efficiently for capturing the live morphology and functionality of skin would broadly impact biological materials characterization by providing real-time biomarkers that could be used to gain a better understanding of basic skin biology, in addition to better detection, diagnosis, and therapy monitoring of skin diseases in a pain-free, patient friendly, and timely manner.

1.2 Anatomy and Physiology of Human skin

1.2.1 Structure-Function

The fundamentals of skin biology have been studied since the early 1800s[1,2]. The top portion of skin consists of two primary layers: the outermost layer, the epidermis, and the second layer, the dermis (Figure 1.1). The epidermis is made up of cells, including: keratinocytes, which provide a physical barrier from the outside world; melanocytes, which produce and transport melanin (the pigment that protects skin from UV damage) to the surrounding keratinocytes; and Langerhans cells, immune cells that monitor the epidermis for incoming pathogens. The epidermis can be further stratified into the following layers (listed from surface of skin to bottom of epidermis): the stratum corneum, the stratum granulosum, the stratum spinosum, and the stratum basale (Figure 1.2). Keratinocytes are the most numerous cell in the epidermis. They begin as

proliferating cells in the basal layer and then, over the course of about one month in normal skin, migrate upwards towards the surface of the skin differentiating into the different cellular layers before ejecting their nucleus and forming the outer layer of dead skin cells that is the stratum corneum.

The dermis, just below the epidermis, contains hair follicles, sweat glands, blood vessels, lymphatic vessels, nerves, and connective tissue, specifically collagen and elastin, which keep the skin firm and tight and cushion the body. The blood and lymphatic vessels in the dermis are the main source of nourishment and waste removal for cells in the dermis and epidermis. Though mostly filled with connective tissue, the dermis also contains cells such as fibroblasts, which synthesize collagen and elastin, and immune cells such as macrophages, which are responsible for cleanup of dermal debris[3], and T cells, important in the skin's defense against invading pathogens[4].

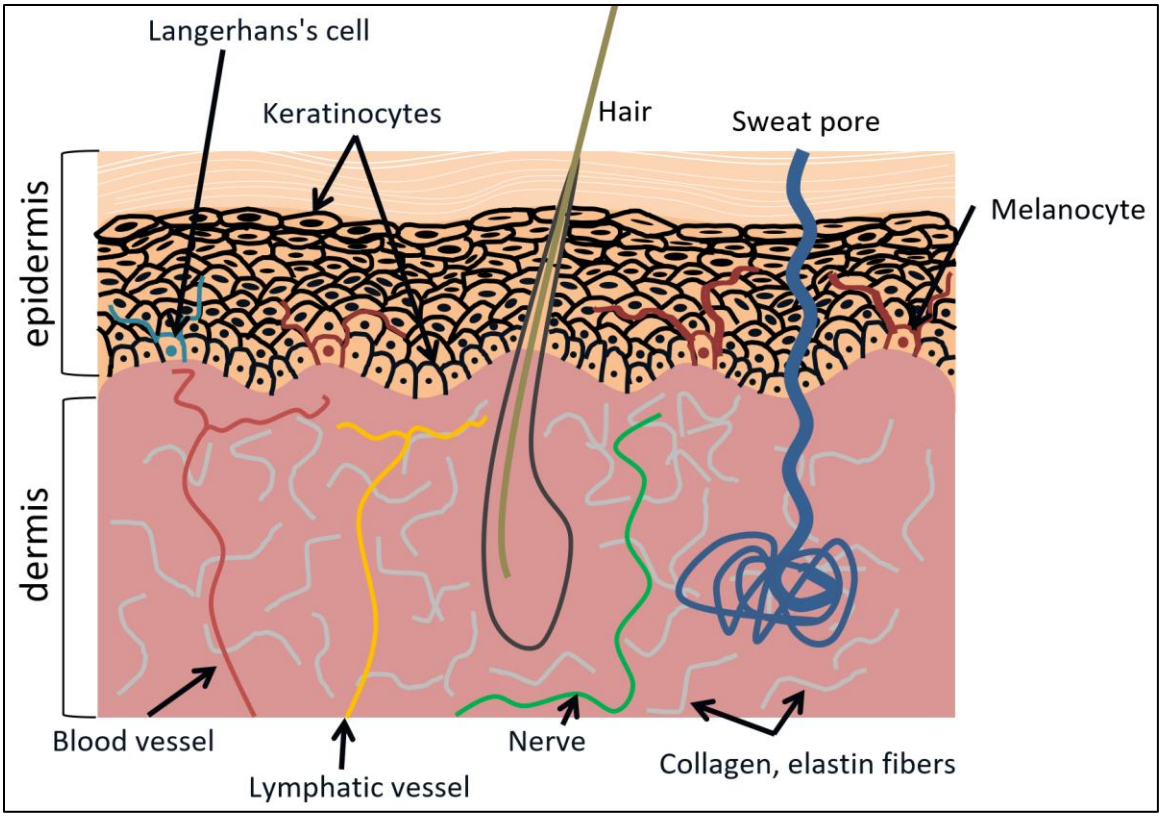

Figure 1.1. Basic skin structure. Cross-sectional schematic of the epidermis and dermis and their components.

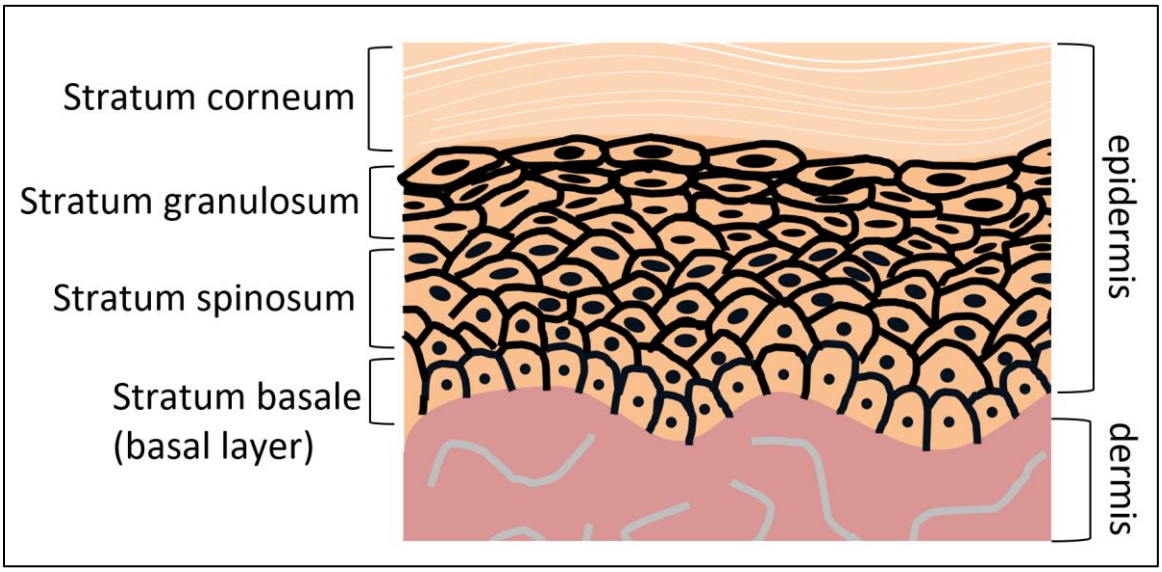

Figure 1.2. Epidermal layers. Cross-sectional schematic of the layers of the epidermis.

Healthy skin requires constant communication between the cells of the epidermis via cell signaling. Each melanocyte and the surrounding 40 or so keratinocytes cooperate together to form a structural and functional unit[5]. An important function of the skin is to protect the body from incoming ultraviolet (UV) radiation. When the skin is irradiated with UV light, the melanocytes are stimulated to produce and transport melanin to the surrounding keratinocytes to protect their DNA from UV-damage. The melanin is transported as melanosomes from the melanocytes to the keratinocytes by way of the melanocyte's dendritic processes. Once the melanosomes reach a keratinocyte, they aggregate around the nucleus where they act as an absorber of UV light, thereby protecting the DNA in the nucleus. The process is tightly regulated by a multitude of factors, including the amount of UV radiation, keratinocyte-secretion factors, and transfer of exosomes[6-8].

Likewise, Langerhans cells have recently been shown to directly communicate with surrounding keratinocytes by way of their dendritic processes[9]. Langerhans cells use their dendrites themselves, and the information they receive from surrounding keratinocytes, to act as an intermediary between the immune system and the skin. Their main function is to continually search the epidermis for pathogens, danger signals, and other environmental hazards.[9]

1.2.2 Skin Disease

When the main functions of healthy skin, including the maintenance of homeostasis, protection of internal structures, and ability to act as a sensory organ, are disrupted, disease may occur. This can manifest as unwanted cosmetic effects, pain, or can even be life-threatening. Some examples of skin being knocked from homeostasis include: the immune system attacking hair follicles preventing the hair from growing (alopecia); the pigment producing melanocytes

becoming malignant (melanoma), the basal keratinocytes becoming malignant (basal cell carcinoma); the melanocytes producing excessive melanin that accumulates in the skin (melasma); the immune system destroying the melanocytes leading to the appearance of white patches on the skin (vitiligo)[10]. Other diseases, such as diabetes[11,12], and pseudoxanthoma elasticum[13,14], although associated with other parts of the body, may be evaluated through skin imaging as they present skin biomarkers.

1.3 Current standard of care clinical skin diagnosis methods and limitations

Dermoscopy, a common tool used to study skin, is a fast and easy-to-use way to obtain a better-than-naked-eye picture of the skin that has been used since the 1950s[15]. The basic components of a dermatoscope are a lens that provides around 10-fold magnification, and a polarized beam of light that illuminates the skin surface. Although it has been shown to be more accurate in the diagnosis of melanoma compared to naked-eye examination,[16] dermoscopy only allows for a view of the surface of the skin, leading to a false-positive rate of around 50% in the diagnosis of melanoma[17], and many unnecessary biopsies.

The use of a UV lamp, or Wood's lamp, is another common way to study the skin. This device is similar to a dermatoscope but uses UV light instead of white light to illuminate the skin and generally provides less magnification. One of the main ways the Wood's lamp is used to study skin is as an aid in determining the location of the hyperpigmentation for skin conditions such as melasma, where knowing the location of the excess pigment is the main factor when guiding therapy decisions. The Wood's lamp is used because in one form of melasma, epidermal melasma, the contrast between hyperpigmented and normally pigmented areas under Wood's lamp

illumination is increased compared to ambient light; while in the other main form of melasma, dermal/mixed melasma, the contrast is decreased under Wood's lamp illumination compared to ambient light[18]. However, in some cases the Wood's lamp has been shown to not correlate with melasma type[19], and cannot predict if the patient will respond to treatment.[20]

The gold standard for the study of skin biology and disease is the biopsy-histology method. This way of studying skin has been used since the early 1800s[1]. The most common form of this method consists of the following steps: (1) cutting out a piece of skin at a suspicious site, (2) fixing the skin in formaldehyde, (3) embedding the fixed skin in paraffin wax, (4) thinly slicing the embedded skin into sections a few micrometers thick, (5) placing the thin sections on a microscope slide, (6) staining the tissue sections with certain chemical dyes that highlight both cellular and extracellular components, (7) and microscopic inspection of the stained tissue section by a dermatopathologist to determine if there is a skin disease or condition present, and if so, what the disease/condition is.

The staining procedure is the most modifiable step in the process, and can be altered to gain different information based on the chemicals used. The most common staining chemicals are hematoxylin and eosin (H&E), which stain cell nuclei purple, and the cellular cytoplasm/extracellular matrix pink, respectively (Figure 1.3, a). From skin stained by this method, dermatopathologists can see key structures that are characteristic of different skin diseases. Other chemicals can stain for specific cellular components, like Fontana-Masson, which stains melanin black[21] (Figure 1.3, b), and CD3, which stains T-cells brown[22,23] (Figure 1.3, c).

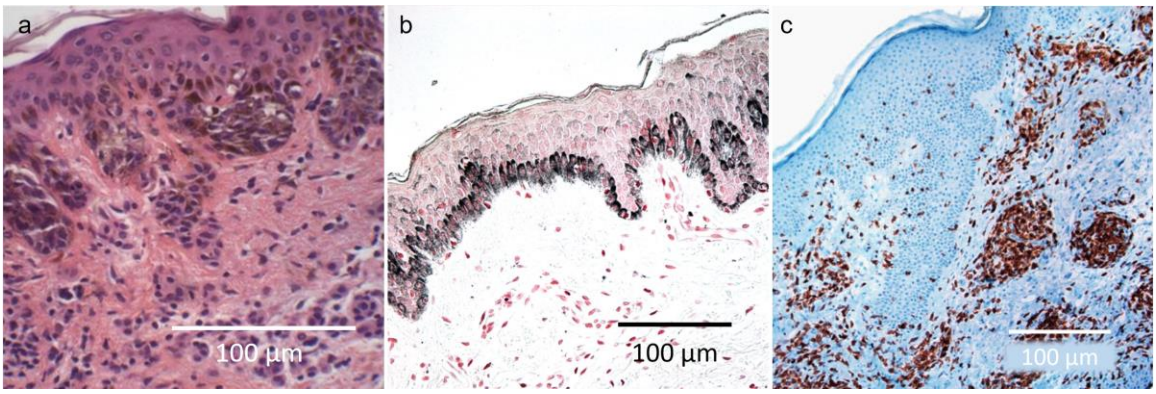

Figure 1.3. Microscopic histological images. (a) H&E stained skin from a nevus. Nuclei are stained purple by hematoxylin, the cytoplasm and extracellular matrix are stained pink by eosin. Image from Balu et al.[24] (b) Fontana-Masson stained normal skin. Melanin is stained black. Image from Kubanov et al.[25] (c) CD3+ stained skin from the disease mycosis fungoides. CD3+ cells are stained brown. Image from Kelemen et al.[26]

Though the tissue processing preserves the overall tissue morphology and the chemical stains allow for some degree of molecular contrast, the main features related to skin functionality are lost. In addition to this, the biopsy is often painful and can lead to complications. The entire process can also be lengthy and costly, highlighting the need for a way to study skin real-time in its native environment with microscopic detail and molecular contrast.

1.4 Advanced clinical skin imaging technologies for noninvasive biological materials characterization

The biopsy and tissue processing method for microscopic evaluation preserves the overall tissue morphology, but the main features related to its functionality are lost. Laser-based optical microscopy technologies recently introduced in the field of dermatology address this limitation by providing access to the live morphology and functionality of the skin through *in vivo*, label free, real-time imaging. These noninvasive imaging tools have great potential to address critical needs

in skin biology, clinical research, and potentially clinical practice of dermatology. Examples include: understanding the underlying mechanism of the immune response in melanoma[27] and pigmentary skin disorders,[28] identifying key optical biomarkers for enhancing the diagnosis accuracy of early melanoma,[29] and to better understand skin therapy effects[30].

1.4.1 Confocal Microscopy

Confocal microscopy is an optical imaging technique that uses a tightly focused raster-scanned laser beam to illuminate an object, and a spatial pinhole to block the out-of-focus light created by the interaction between the laser and the object before it reaches the detector for image formation. Developed by Minsky in 1955,[31] confocal microscopy allows for high resolution three-dimensional reconstructions of objects by capturing multiple two-dimensional images at different depths within the object, known as optical sectioning.

Reflectance confocal microscopy (RCM), a type of confocal microscopy, was translated to the clinic in the early 2000s and demonstrated the potential to address some of the problems with dermoscopy and histology. An example of a clinical RCM device can be found in Figure 1.4, a. RCM uses focused near-infrared light from a diode laser to raster-scan the skin surface. The backscattered light is collected through the spatial pinhole to provide gray-scale images with sub-cellular resolution in thick tissue. The contrast mechanism for RCM is based on differences in the refractive indices of tissue components[32,33], which makes this approach applicable to skin lesions that can be characterized based on morphological assessment alone. RCM imaging has been shown to significantly improve diagnostic accuracy and early detection of melanocytic and nonmelanocytic skin cancers compared to clinical and dermatoscopic examination alone[34-37], but due to its limited contrast, the specificity remains low[38].

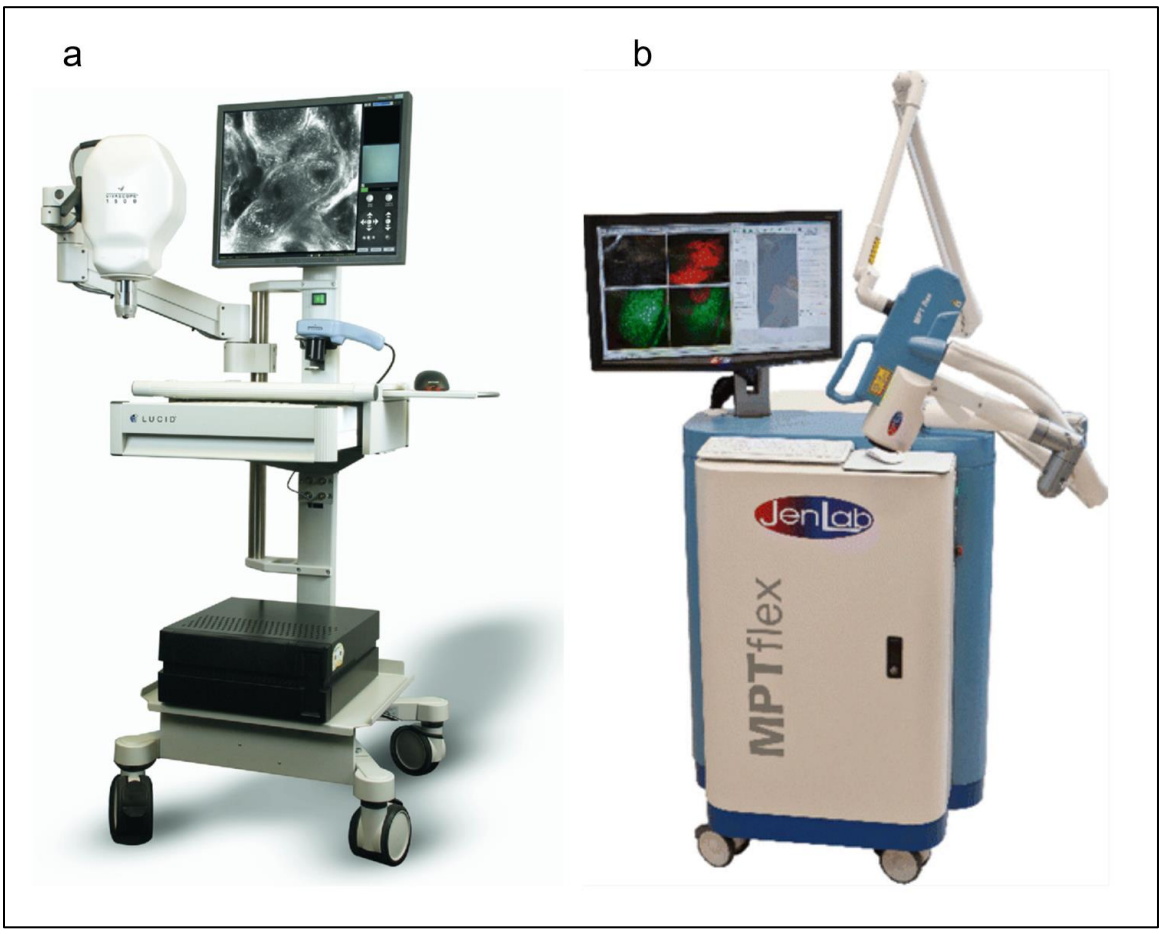

Figure 1.4. Advanced *in vivo* clinical imaging technologies. (a) Reflectance confocal microscopy device (Vivascope 1500, Caliber ID, USA). Image from Nehal et al[39]. (b) Multiphoton microscopy device (MPTflex, JenLab GmbH, Germany). Image from Raphael and Prow[40].

1.4.2 Multiphoton Microscopy

Multiphoton microscopy (MPM), a non-linear optical imaging technique, overcomes some of the limitations of RCM, providing a way to study skin *in vivo* in real time with sub-micron resolution and label-free molecular contrast. MPM images are formed by raster-scanning a tightly focused laser light on the tissue and detecting the light generated from the interactions between

the laser light and different molecular components in the tissue. Two of the most common light-tissue interactions that generate signal in MPM imaging are the nonlinear optical processes two-photon excited fluorescence (TPEF) and second harmonic generation (SHG).

The TPEF process consists of two main steps: two photon absorption, and radiative relaxation, or fluorescence. Two photon absorption involves the near simultaneous absorption of two photons by a molecule, inducing a transition of the molecule from the ground electronic state to an excited electronic state via a virtual state (Figure 1.5, a). The energy required for this transition is equal to the energy difference between the initial and final states of the transition and is realized from the sum of two photon energies. This phenomenon can be explained intuitively in the following manner: although just one photon does not have the requisite energy to induce this transition to the excited state on its own, the energy mismatch between an incoming photon and the nearest one-photon allowed state provides a finite time for a second photon to arrive and complete the transition to the final excited state.[41] The finite time allowed for the second photon to complete the transition is on the order of ~10^{-15} seconds[42], meaning for this event to occur with any detectable probability, there must be a large photon flux incident on the molecule. In TPEF, once the molecule is elevated to an excited state, the molecule may undergo internal conversion to the first singlet state of the excited state, before the system radiatively decays back to the ground state by emitting a fluorescence photon (Figure 1.5, a).

In one photon absorption, one photon provides the necessary energy to promote a molecule to its excited state, thus one photon absorption depends linearly on excitation irradiance. However, since TPEF relies on the absorption of two photons, the process is quadratically dependent on irradiance. This means two photon absorption only occurs in the focal volume, as illustrated in Figure 1.6, which minimizes out-of-focus fluorescence contribution. The spatial confinement of

the TPEF is used in MPM imaging for generating optical sections without the need of a pinhole to remove the out-of-focus fluorescence. An additional advantage of the TPEF over one photon fluorescence excitation is related to the near infrared excitation wavelengths involved in the TPEF process. Longer wavelengths penetrate deeper into highly scattering tissues such as human skin.

SHG is a coherent process in which two incoming photons with the same energy interact with a nonlinear material and are combined to produce a new photon instantaneously with exactly double the energy of the incoming photons (Figure 1.5, b). The second order nonlinear susceptibility of a material determines its tendency for SHG. As an even-order nonlinear optical phenomena, SHG only occurs in materials without inversion symmetry, or non-centrosymmetric materials. Examples of SHG in biological tissues include collagen, myosin, and microtubules, all of which possess high enough second order nonlinear susceptibilities for SHG microscopy.[43-47]

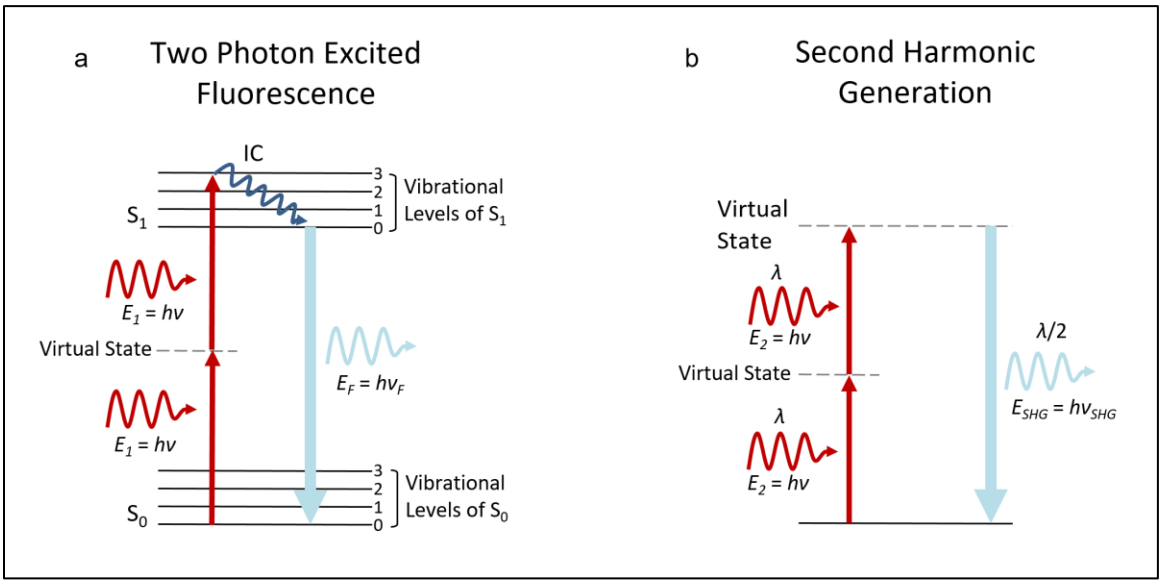

Figure 1.5. Jablonski diagrams for two photon excited fluorescence (TPEF) and second harmonic generation (SHG). In TPEF (a), absorption by the molecule of two photons excites the molecule from a lower energy state (S_0) to a higher energy state (S_1). After the excitation process, the molecule undergoes internal conversion (IC), followed by radiative relaxation back to the lower energy level. In SHG (b), two photons with energy E_2, and wavelength λ, are converted to a single photon with a wavelength of $\lambda/2$. E = energy; h = Plank's constant, v = frequency.

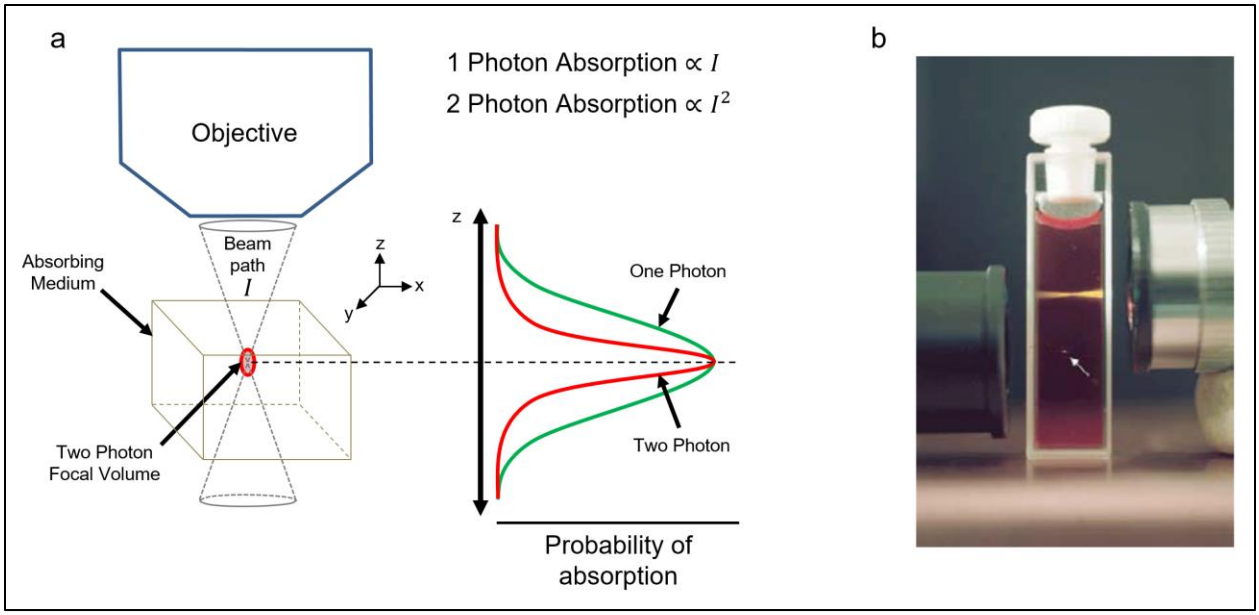

Figure 1.6. One-photon vs two-photon absorption. (a) Schematic illustration of the difference in absorption probabilities in an absorbing medium between one photon (green curve) and two photon (red curve) absorption, and dependence on laser light irradiance, *I*. (b) Photograph showing the fluorescence emission from a solution containing fluorescent molecules by means of one (cone, top) and two photon (dot pointed out by white arrow, bottom) excitation. Adapted from Diaspro, et al.[48]

MPM contrast in the epidermis of human skin arises mainly from the following molecules: TPEF from the coenzymes nicotinamide adenine dinucleotide (NADH), nicotinamide adenine dinucleotide phosphate (NADPH), and flavin adenine dinucleotide (FAD)[49,50], melanin[51], and keratin[52]. In the dermis, contrast comes from TPEF of elastin fibers[47], and SHG of collagen fibers[53]. Certain cells in the dermis can also be visualized with TPEF, and may indicate an immune response[54].

The first certified MPM medical device for imaging human skin *in vivo* was introduced in 2002[55] and has since shown promise as an important research and clinical tool for label-free imaging in human skin. An example of the clinical MPM device can be found in Figure 1.4, b. The applications of *in vivo* label-free MPM span from skin cancer detection and diagnosis[24,56-58],

to characterizing and understanding keratinocyte metabolism[59], skin aging[60], pigment biology[61,62], and cosmetic treatments[63,64]. The first aim of this dissertation is to further evaluate the potential of *in vivo* MPM imaging to enhance the understanding of skin biology by characterizing its structure and function in its native environment. This enhanced understanding may help improve early diagnosis of skin diseases and provide a more informative guide to effective treatment. The second aim involves the design and development of a more efficient, optimized MPM-based clinical platform that addresses critical challenges of the current commercial clinical instrument[65]. These technical challenges are related to limited scanning area, slow frame rate, high cost, and complexity. The capability of scanning large areas is critical for improving the accuracy of the characterization of skin, particularly for non-uniform lesions. Enhancing scanning speed improves the efficiency of the imaging procedure, minimizes motion artifacts and optimizes clinical workflow. Reducing complexity, cost, and footprint are essential for improving adoption of the technology and increasing clinical access.

1.5 Dissertation Outline

This dissertation is focused on research at the intersection of noninvasive biological materials characterization, medical device technology development, and clinical dermatology. Skin components such as NADH and melanin play key roles in skin homeostasis and are two of the main skin components affected in skin disease. They are also readily studied *in vivo* with noninvasive imaging technologies and provide the basis for the bulk of the research herein.

Chapter 2 presents a unique view of vitiligo, a skin disease characterized by the loss of epidermal melanocytes leading to depigmented patches on the skin, using a combination of MPM

imaging, RCM imaging, and single cell transcriptomics, to provide insights into the basic understanding of the biology of the disease, and therapeutic response. The goal of this research is to use these techniques to gain more information on the metabolic state of the skin in vitiligo and observe what happens to the metabolics and pigmentation after treatment for the disease. Data analysis includes a quantification of RCM repigmentation after vitiligo treatment, a quantification of the skin metabolism *in vivo* using MPM, and single cell analysis of the transcriptomics of the cells present in vitiligo compared to normally pigmented skin.

Chapter 3 provides insights into the characteristics that distinguish benign melanocytic nevi from tumors that may be in evolution to become malignant melanoma, a cancer of the melanocytes. The goal of this research is to evaluate the potential of MPM to: a) identify histopathological features of benign nevi using *in vivo* MPM images; b) distinguish between benign nevi and nevi in evolution to melanoma based on optical biomarkers related to MPM signals; c) identify the immune response in the *in vivo* MPM images of benign nevi. Data analysis and interpretation consists of a qualitative component, and a quantitative component. The qualitative component is a comparison of the MPM and histologic images of biopsied nevi with the assistance of a dermatopathologist in order to identify and correlate their morphological features, including the presence of melanophages, the pigment scavenging cells in the dermis. The quantitative component focuses on the appearance and size of the cells that make up the nests of the nevus.

Chapter 4 offers an evaluation of the potential for MPM to characterize the skin condition melasma, another skin disorder related to melanocyte function that leads to a hyperpigmentation of the skin. The goal of this study is to identify and characterize the biological hallmarks of the condition in *in vivo* MPM images. The data analysis and interpretation consists of: a qualitative analysis of the images alongside a dermatopathologist familiar with MPM to assess the melanin

distribution in epidermal cells in relation to sun damage in the dermis and signs of prior immune response; and a quantitative analysis of the amount of pigment in the epidermis of melasma patients.

Chapter 5 seeks to address limitations of the previous studies by way of the development of a new MPM instrument. The new instrument features faster scanning speeds, a larger field of view, and enhanced molecular contrast. Preliminary data on performance of the new device and necessary steps for translation from laboratory to clinic are the focus of this chapter.

Chapter 6 provides a summary of the work and a perspective on the future outlook of the field, including new uses for the current devices and areas of focus in new device development.

2. Insights into keratinocyte homeostasis in vitiligo skin

2.1 Background

Vitiligo is an autoimmune skin disease characterized by the progressive destruction of melanocytes by autoreactive CD8+ T cells, resulting in disfiguring patches of white depigmented skin that causes significant psychological distress among patients[66]. CD8+ T cells play an important role in the elimination of melanocytes and are increased in active vitiligo skin[67-69]. However, in stable vitiligo lesions devoid of melanocytes, T cells are sparse and immune activation levels are low[70]. This makes it unclear why white patches continue to persist in the absence of a robust inflammatory infiltrate.

Development of mouse models representative of human disease have provided important clues on the role of the adaptive immune system[71,72]. Keratinocytes secrete CXCL9 and CXCL10 to attract and activate CD8+ T cells[73], and these chemokines are present in the blister fluid of human vitiligo patients[69]. However, the adoptive transfer of autoreactive CD8+ T cells in the mouse model cannot fully recapitulate the complex interactions between melanocytes, keratinocytes, and immune cells that occurs in situ in human skin since melanocytes are present in the epidermis in only select locations in mice, and the mouse epidermis lacks the keratinocyte stratification of human skin[74]. To date, most translational studies in vitiligo are limited to examining cultured cells in vitro or immunohistochemistry of diseased tissue. It has been difficult to study the contribution of other tissue cells in stable vitiligo because of the lack of tools to characterize the disease noninvasively.

Another understudied topic in vitiligo research is the monitoring of treatment effects to learn more about the biological reasons behind successful treatments. Narrow band ultraviolet B (NBUVB) light therapy and autologous micrografting therapy are two common treatments for vitiligo[75], but neither is uniformly successful, and repigmentation often requires many treatment sessions to achieve an adequate response[76]. Though murine models[77,78] and human studies[79] have defined a melanocyte population that migrates to the epidermis during repigmentation, this process has not been tracked *in vivo* and it is still not clear what signals drive the lateral migration of melanocytes within the epidermis to repigment the vitiligo skin after these treatments.

Optical imaging technologies such as RCM and MPM are unique tools for the study of vitiligo and vitiligo treatment effects. RCM can image a relatively large skin area (mm-scale), allowing for the visualization and tracking of the melanocytes that are repigmenting the skin after successful treatment. MPM provides images with sub-micron resolution and label-free molecular contrast that can be used to characterize keratinocyte metabolism in human skin[57,59]. In addition to the information provided by optical microscopy, we also performed single-cell RNA sequencing (scRNA-seq) on patient-matched pretreatment lesional and nonlesional tissue to identify stressed keratinocyte subpopulations in vitiligo skin.

2.2. Outstanding questions and aims

- What are the reasons for stable vitiligo disease persistence?
- Keratinocytes are known regulators of melanocyte behavior. Are the keratinocytes the cause for melanocyte failure to repigment vitiligo lesions?
- Can potentially altered keratinocytes be distinguished based on their gene expression?

- Is the failure of repigmentation caused by the destruction of the melanocytes during migration, or the inhibition of their migration?

Aims:

1) Assess the presence of sub-populations of keratinocytes in normal and vitiligo skin based on their metabolic state.

2) Assess the gene expression of keratinocytes in vitiligo and normal skin.

3) Evaluate the behavior of melanocytes during repigmentation by monitoring their migration during treatment.

2.3 Method of study

2.3.1 Autologous micrografting procedure

Twelve vitiligo patients were enrolled to undergo autologous punch micrografting performed by Dr. Anand Ganesan, a board certified UC Irvine dermatologist. Punch micrografting is a surgical procedure where 1 mm pieces of normal epidermis are grafted into vitiligo skin to provide a new melanocyte reservoir for re-pigmentation[80]. All patients had stable vitiligo (vitiligo area had not increased in size for at least six months), were unresponsive to past treatment attempts, and had no treatment in the three months before imaging for this study. Vitiligo patient ages were 34-74 with an average age of 56. Vitiligo lesion locations included wrist (2), hand (2), leg (5), arm (1), face (1), and neck (1).

2.3.2 MPM imaging

The twelve vitiligo patients who underwent micrografting therapy as described above, and five volunteers with normal skin were imaged *in vivo* by MPM. All *in vivo* measurements were conducted according to an approved institutional review board protocol of the University of California, Irvine (HS No. 2018-4362), with written informed consent obtained from all patients.

We used an MPM-based clinical tomograph (MPTflex, JenLab, GmbH, Germany) for the *in vivo* imaging of the vitiligo and normal skin. This imaging system consists of a femtosecond laser (Mai Tai Ti:Sapphire oscillator, sub-100 fs, 80 MHz, tunable 690– 1020 nm; Spectra-Physics), an articulated arm with near-infrared optics, and beam scanning module. The imaging head includes two photomultiplier tube detectors used for parallel acquisition of TPEF and SHG signals. The excitation wavelength used in this study was 760 nm. The TPEF and SHG signals were detected over the spectral ranges of 410 to 650 nm and of 385 to 405 nm, respectively. We used a Zeiss objective (40×, 1.3 numerical aperture, oil immersion) for focusing the laser light into the tissue. The laser power used was 5 mW at the surface and up to 30 mW in the superficial dermis of the skin. We acquired the MPM data as z-stacks of en-face images from the stratum corneum to the superficial dermis. The field of view (FOV) for each optical section was 100×100 μm^2 and the step between the optical sections was 5 μm. Imaging on vitiligo patients occurred before they underwent a micrografting procedure, and then and 3, 6, and 10 weeks following the micrografting procedure (patients also underwent UVB phototherapy twice/week after micrografting). Sites imaged before treatment were: 1) the vitiligo area where the normally pigmented skin grafts were to be transplanted, and 2) the donor site where the normally pigmented skin grafts were to be taken. During treatment, sites imaged were: 1) the area near the graft at the border of the repigmenting skin and the still depigmented skin, and 2) an adjacent normally pigmented area >5 cm from the

vitiligo skin. Imaging locations for the volunteers with normal skin were the sun exposed dorsal forearm, and the non-sun exposed volar upper arm to focus on areas with relatively higher pigment amounts (sun-exposed), and relatively lower pigment amounts (non sun-exposed). Due to the limited FOV of each individual scan, we acquired several stacks of images within each site in order to sample a larger area. Thus, a total of 1,908 images were acquired for this study, corresponding to an average of 18 images for each imaging site. Images were 512 × 512 pixels and were acquired at approximately 6 s per frame. All images were color-coded such that green and blue represent the TPEF and SHG signals, respectively.

2.3.3 RCM imaging

We used the VivaScope 1500 device (Caliber ID, Massachusetts, USA) for the *in vivo* RCM imaging of vitiligo patients. The imaging system consists of an 830 nm diode laser and a 30× 0.9 numerical aperture water immersion objective lens for focusing the laser light into the tissue. We acquired the RCM data as z-stacks of en-face images from the stratum corneum to the superficial dermis with a 5 μm step size, and as tiled mosaics of en-face images covering areas of up to 6 × 6 mm. The FOV for each individual en-face image was 500 × 500 μm^2. Due to the RCM device availability and participant drop-out, not all 12 vitiligo patients enrolled in the study were RCM imaged at every time point. Imaging was completed 3 weeks post micrograting treatment for 8 patients, 6 weeks post treatment for 7 of those 8 patients and 1 additional patient, and 10 weeks post treatment for 5 of the 8 original patients, the 1 additional patient imaged at 6 weeks, and 2 more patients. In total, 11 patients were imaged with RCM. All imaging sessions were focused at a specific micrograft and the surrounding few mm. For each patient, comparison of

clinical images taken at each time point was used to ensure the same micrograft was imaged each session.

2.3.4 Mitochondrial clustering analysis

We collaborated with Dr. Irene Georgakoudi's group at Tufts University to perform mitochondrial clustering analysis on the MPM images. Dr. Georgakoudi's group has extensive experience applying this approach, and the methods used for this study were similar to those described in previously published research by Dr. Georgakoudi's group: Xylas et al[81], and Pouli et al[57]. In brief, we performed preprocessing steps to remove keratin and melanin associated fluorescence and image features associated with the nuclear and interstitial spaces. Next, a 2-D Fourier transform was performed on the processed image. This transform describes the relative prevalence of intensity fluctuations at different characteristic spatial frequencies. As spatial frequency, k, is inversely proportional to length scale, the squared amplitude of the Fourier transform of an image, the power spectral density (PSD), or R(k), is a metric that can be used to quantify the occurrence of morphological features of different length scales within the image. The morphology of biological cells and tissue often exhibits PSDs with an inverse power law dependence on spatial frequency [$R(k) \propto k^{-\beta}$]. Increasing values of the power law exponent, β, correlate with an increased degree of clustering in the image features[82]. Thus, to assess clustering, we fit to the PSD an inverse power law equation of the form $R(k) = Ak^{-\beta}$. The power law exponent, β, was computed for each MPM image and indicates the level of mitochondrial clustering.

Comparisons of median β values and β variability for each stack of MPM images were performed using a two-sided student's t test, with p-values < 0.05 considered statistically significant.

2.3.5 Single cell transcriptomics analysis

An ongoing part of this research includes a collaboration with Dr. Anand Ganesan's group, and UC Irvine mathematician and systems biology researcher Dr. Qing Nie's group to analyze gene expression in vitiligo lesional skin compared to patient-matched nonlesional skin using a single-cell transcriptomics approach. Single cell RNA sequencing (scRNA-seq) was performed on skin blisters from the vitiligo lesional and nonlesional skin from seven patients. The donor skin sites were cleaned with ethanol wipes and 5 suction blisters (1 cm diameter) were created by applying a standard suction blister device. We unroofed the blisters and subjected them to scRNA-seq, performed by the Genomics High Throughput Sequencing facility at the University of California, Irvine with the 10x Chromium Single Cell 3' v2 kit (10x Genomics).

Sequencing libraries were prepared using the Chromium Single Cell 3/ v2 protocol (10x genomics). Sequencing was performed on Illumina HiSeq4000 platform (Illumina). FASTQ files were generated from Illumina's binary base call raw output with the cellranger piopeline (v2.1.0, 10x genomics).

All procedures were conducted according to an approved institutional review board protocol of the University of California, Irvine (HS No. 2018-4362), with written informed consent obtained from all patients.

2.4. Results

2.4.1 Assessment of keratinocytes metabolism in vitiligo patients using a mitochondrial clustering approach pretreatment

MPM image based mitochondrial clustering values show consistent depth-dependent trends in normal epidermis[57]. In short, the basal and parabasal keratinocytes present a fragmented mitochondria phenotype characterized by high values of the mitochondrial clustering metric, β. As cell differentiation progresses from the basal to the higher epidermal layers and cells turn from glycolysis to oxidative phosphorylation for energy production, mitochondria fuse and create more extensive networks that correspond to low clustering values, reaching their minima within the spinous layer. Finally, toward the most terminally differentiated layer, as the granular keratinocytes enter an apoptotic state to create the stratum corneum, mitochondrial clustering values recover again, signifying a return to a more fissioned phenotype[57].

Based on the mitochondrial clustering analysis of the MPM images acquired before treatment from the vitiligo and normal pigmented (non lesional) skin of the 12 patients enrolled in the study, we found that vitiligo lesions showed an altered trend of the depth-dependent mitochondrial clustering compared to the non lesional skin (Figure 2.1).

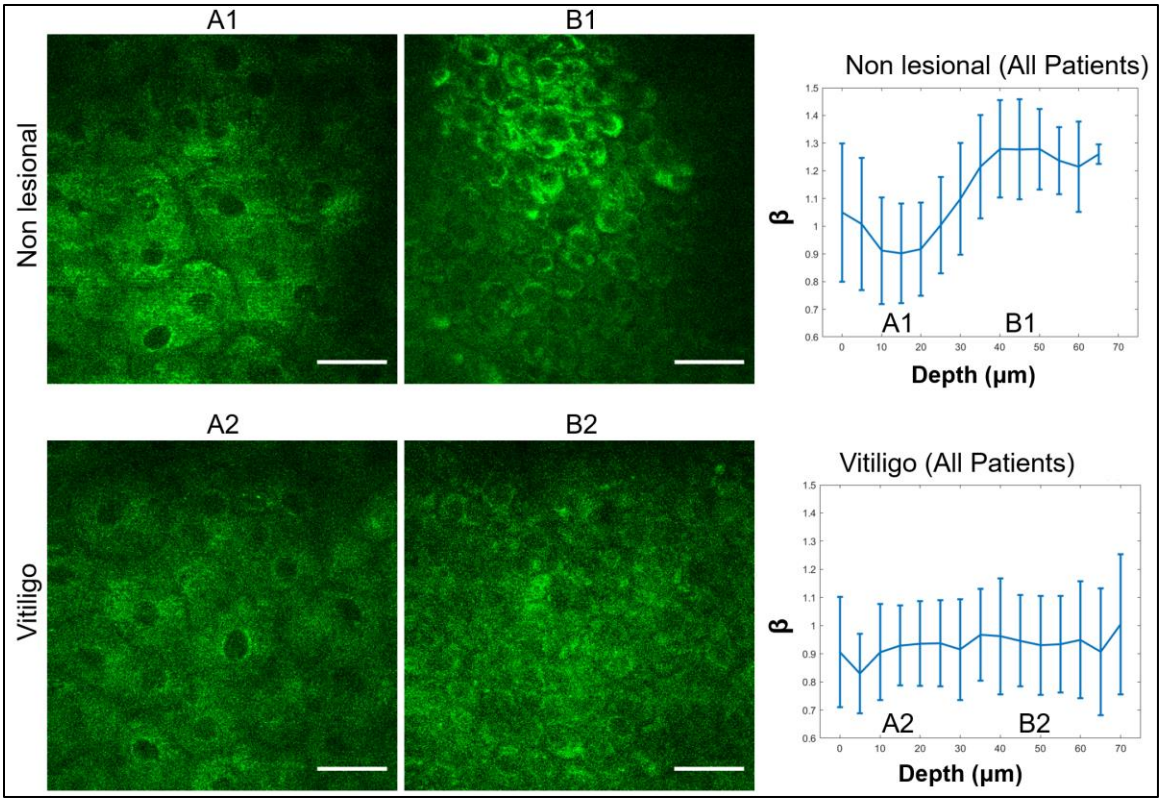

Figure 2.1. *In vivo* MPM images of vitiligo and non lesional (normal) skin showing metabolic changes with depth. Representative en-face MPM images from the stratum granulosum in non lesional (A1) and vitiligo skin (A2) and from the basal layer in non lesional (B1) and vitiligo skin (B2) of one patient. Average mitochondrial clustering (β) values based on z-stacks from all patients as a function of depth for the non lesional area in vitiligo patients (top right) and the vitiligo area (bottom right) are shows as a function of depth in the epidermis. Error bars represent the standard deviation of the measurements for the images in all the z-stacks at each area. The labels A1, A2, B1, and B2 within the mitochondrial clustering panels represent the mitochondrial clustering values extracted from the panel's respective labeled images. Scale bars are 20 μm.

In order to assess whether the changes of the beta values across the epidermis of vitiligo and normal skin are statistically significant, we calculated the mitochondrial clustering (β) median value and its variability. We found that these metrics are significantly different in vitiligo compared to non lesional skin (Figure 2.2).

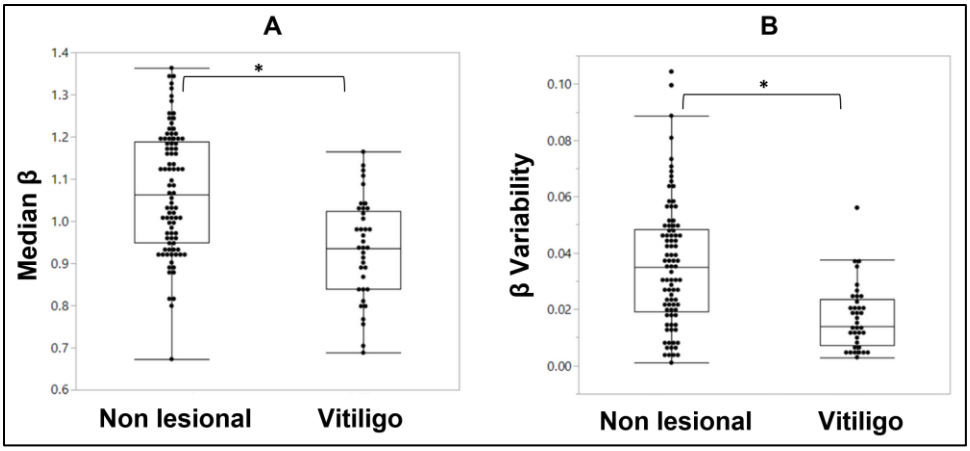

Figure 2.2. Mitochondrial clustering metrics based on MPM imaging are significantly different in vitiligo compared to non lesional skin. (A) Distribution of the median β values; each value corresponds to a z-stack of images acquired in non lesional and vitiligo lesional areas. (B) Distribution of the β variability values; each value corresponds to a z-stack of images acquired in non lesional and vitiligo lesional areas. * = t-test p-value < 0.05.

Since the fluorescence signals from all the skin fluorophores, including NADH, are collected on the same detection channel in the MPTflex clinical microscope, we sought to ensure the mitochondrial clustering measurements were not affected by contributions from fluorophores other than NADH. Melanin requires particular consideration since it is the main source of difference in appearance between the vitiligo and normal skin. In this study, we used a thresholding algorithm we previously demonstrated to efficiently separate NADH from the other fluorophores in keratinocytes based on the observation that pixels corresponding to fluorophores other than NADH create clusters of higher intensity values[57]. To further validate this approach, we measured the NADH clustering in the normal skin keratinocytes of five volunteers based on MPM images acquired at a sun exposed site (dorsal forearm) and a non-sun exposed site with relatively less melanin (volar upper arm).

Based on clustering analysis of the MPM images, we found that the depth dependent β values showed similar trends in the epidermis (Figure 2.3) and the median β values and β

variability values were not statistically significantly different when comparing vitiligo and normal skin (Figure 2.4).

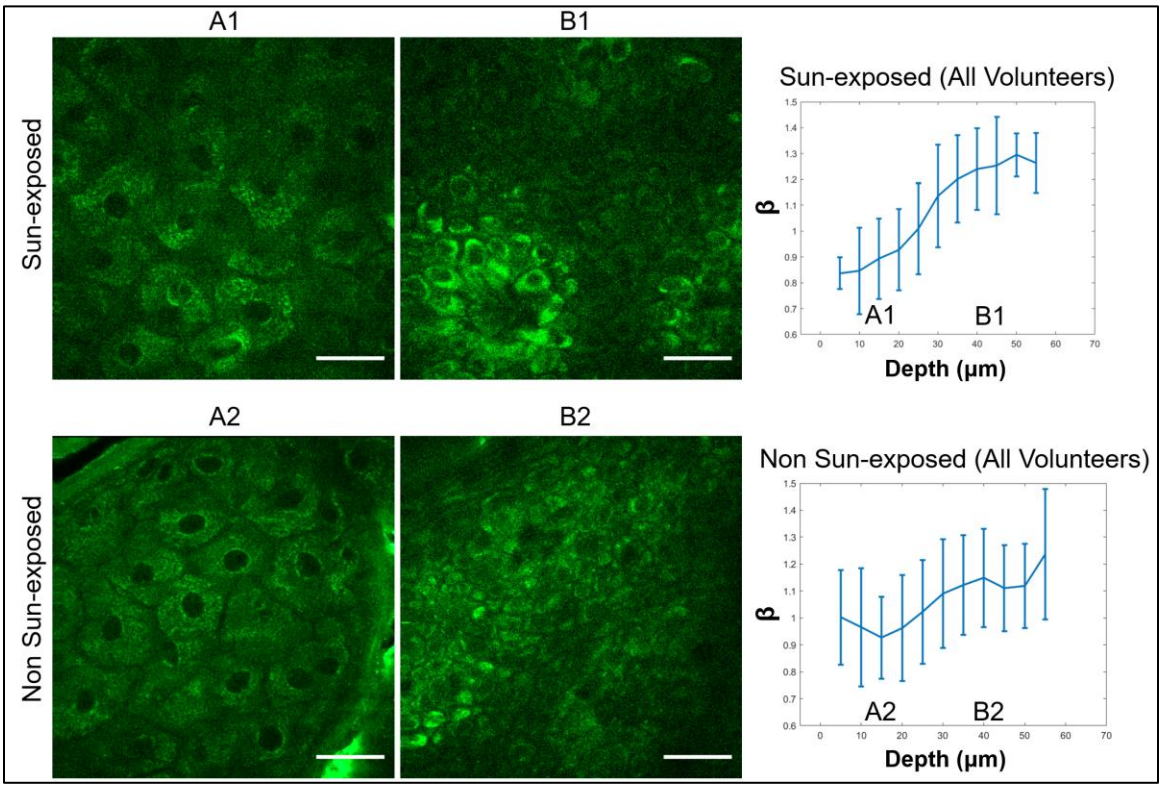

Figure 2.3. *In vivo* MPM images of non sun-exposed and sun-exposed normal skin showing metabolic changes with depth. Representative en-face TPEF images from the stratum granulosum layer of the sun-exposed (A1) and the non sun-exposed (A2) areas and from the basal layer of the sun-exposed (B1) and the non sun-exposed (B2) areas on the forearm and the volar upper arm of a volunteer, respectively. Average mitochondrial clustering (β) values based on z-stacks from all volunteers as a function of depth for the sun-exposed (top) and non sun-exposed (bottom) areas are shown as a function of depth in the epidermis. Error bars represent the standard deviation of the measurements for the images in all the z-stacks at each site. The labels A1, A2, B1, and B2 within the mitochondrial clustering panels represent the mitochondrial clustering values extracted from the panel's respective labeled images. Scale bars are 20 μm.

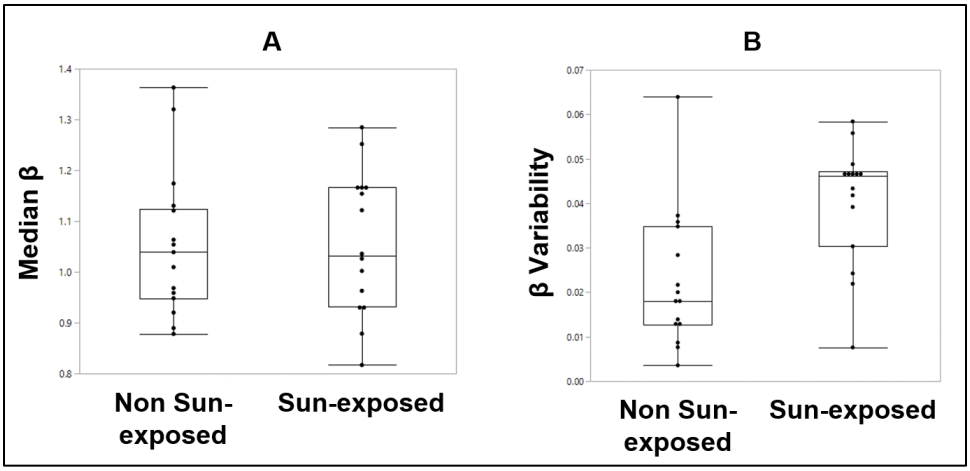

Figure 2.4. Mitochondrial clustering metrics based on MPM imaging are not significantly different in non sun-exposed compared to sun-exposed normal skin. (A) Distribution of the median β values; each value corresponds to a z-stack of images acquired in the non sun-exposed and sun-exposed measurement sites in all volunteers. (B) Distribution of the β variability values; each value corresponds to a z-stack of images acquired from the non sun-exposed and sun-exposed sites in all volunteers (t-test p-values >0.05).

These results confirm that the different trend of mitochondrial clustering in keratinocytes of vitiligo skin compared to normal skin is a result of changes to mitochondrial organization related to vitiligo, and was not affected by the differences in melanin content of the vitiligo and normal epidermis.

2.4.2 Pretreatment single cell RNA sequencing analysis

Mitochondrial clustering analysis on pretreatment MPM images demonstrated that keratinocytes in vitiligo lesions were metabolically altered, suggesting that keratinocyte cell states are different in vitiligo lesional skin compared to nonlesional skin. To examine the major alterations in keratinocyte cell states in vitiligo, we performed scRNA-seq on patient-matched lesional and nonlesional suction blisters from seven patients using the 10x Genomics Chromium platform (Figure 2.5, a). We obtained a total of 9,254 cells from vitiligo lesional skin and 7,928 cells from nonlesional skin for downstream analyses. We performed integration analysis of data

from all patients using a recently developed approach scMC, which has shown its superior capability in preserving biological signals while removing batch effects[83]. Unsupervised clustering analysis identified 14 cell clusters (Figure 2.5, b). Cell clusters were visualized using Uniform Manifold Approximation and Projection (UMAP) space, which estimates a topology of the high-dimensional data and uses this information to construct a low-dimensional representation that preserves relationships present in the data[84]. Specifically, we identified two keratinocyte states that upregulate expression of keratins that are not normally expressed in the mature interfollicular epidermis and are associated with insults like wounding and UV injury[85,86] (Figure 2.5, b, circles). Compared to nonlesional skin, vitiligo lesional skin showed an increased presence of these stressed keratinocytes (Figure 2.5, c). This finding of a stressed population of keratinocytes in vitiligo epidermis is consistent with our MPM imaging data, which revealed an altered cellular state of vitiligo keratinocytes.

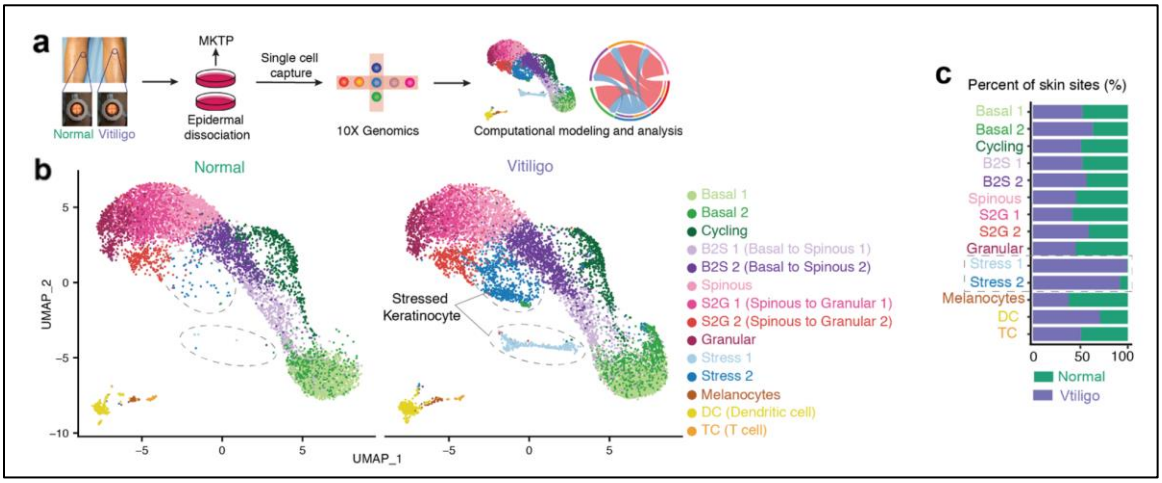

Figure 2.5. Vitiligo skin contains populations of stressed keratinocytes. (A) Workflow of patient sample processing for scRNA-seq. (B) UMAP plot of patient data showing unique clusters in lesional skin. (C) Percentage of different cell types from vitiligo and normal skin in each cluster from B.

2.4.3 Assessment of keratinocyte metabolism in vitiligo patients using a mitochondrial clustering approach post-treatment

Mitochondrial clustering analysis of the MPM images acquired after micrografting treatment from the vitiligo and nonlesional pigmented skin showed that keratinocytes in vitiligo lesions in patients that did experience clinical repigmentation due to treatment exhibited a return to normal depth-dependent mitochondrial clustering trends (Figure 2.6, a). In contrast, the kerationcytes in vitiligo lesions that did not experience clinical repigmentation due to treatment still demonstrated an altered trend of the depth-dependent mitochondrial clustering compared to the normal skin (Figure 2.6, d). Statistical analysis demonstrated the median β values and β variability values were not statistically significantly different when comparing vitiligo and normal skin in the patients that responded to treatment (Figure 2.6, b, c), while the values were statistically significantly different when comparing vitiligo and normal skin in the patients that were unresponsive to treatment (Figure 2.6, e, f).

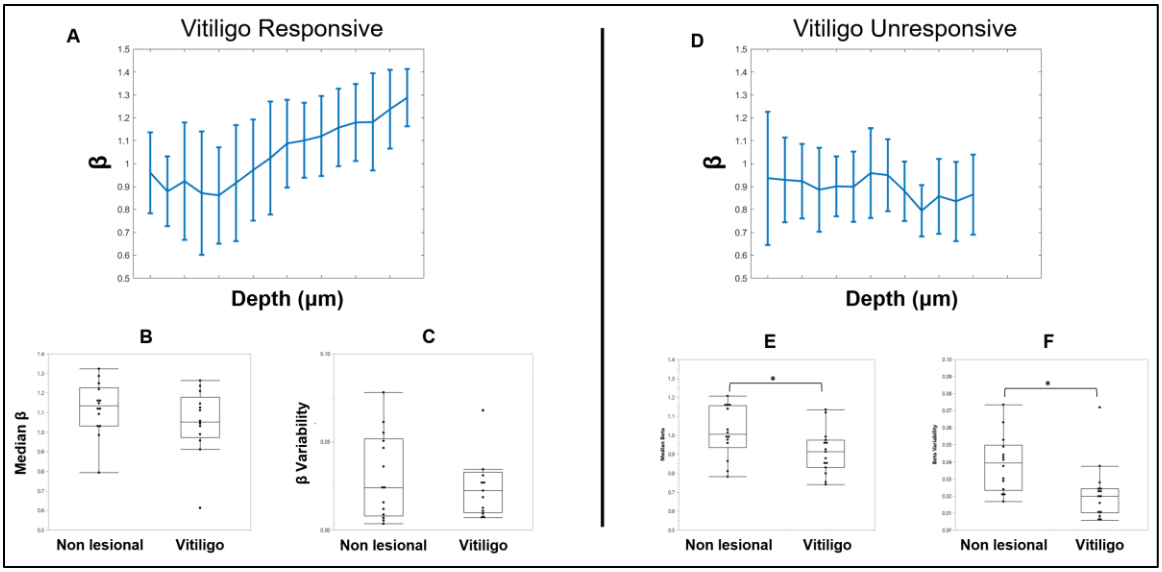

Figure 2.6. MPM mitochondrial clustering values in patients 10 weeks after vitiligo therapy initiation. Beta clustering values with depth in the epidermis for patients that responded to therapy (A) (clinical repigmentation and active migrating melanocytes observed with RCM), and for patients that did not respond to therapy (D) (no clinical repigmentation and no active migrating melanocytes observed with RCM). Bottom part of panels are a distribution of the median β values in the responsive patients (B) and unresponsive patients (E), and β variability values in the responsive patients (C) and unresponsive patients (F); each value corresponds to a z-stack of images acquired at each measurement site. T-test p-values >0.05 for responsive patients and <0.05 for unresponsive patients as denoted by *.

2.4.4 Assessment of the repigmentation process using RCM imaging of vitiligo patients post-treatment

Analysis of RCM images showed that the initiation of the repigmentation process after treatment can be visualized by the outward migration of active dendritic melanocytes from micrografts as clinical repigmentation was observed (Figure 2.7). Migrating melanocytes were visualized in five out of the eleven vitiligo lesions imaged (Figure 2.8), and the same five patients were the only lesions to see clinical repigmentation. Quantitative analysis showed that in the five vitiligo lesions that melanocytes were imaged, the distance from the skin graft of imaged

melanocytes increased over time post-micrografting treatment (Figure 2.8). In no patients where melanocytes were imaged did they subsequently disappear at a later time point.

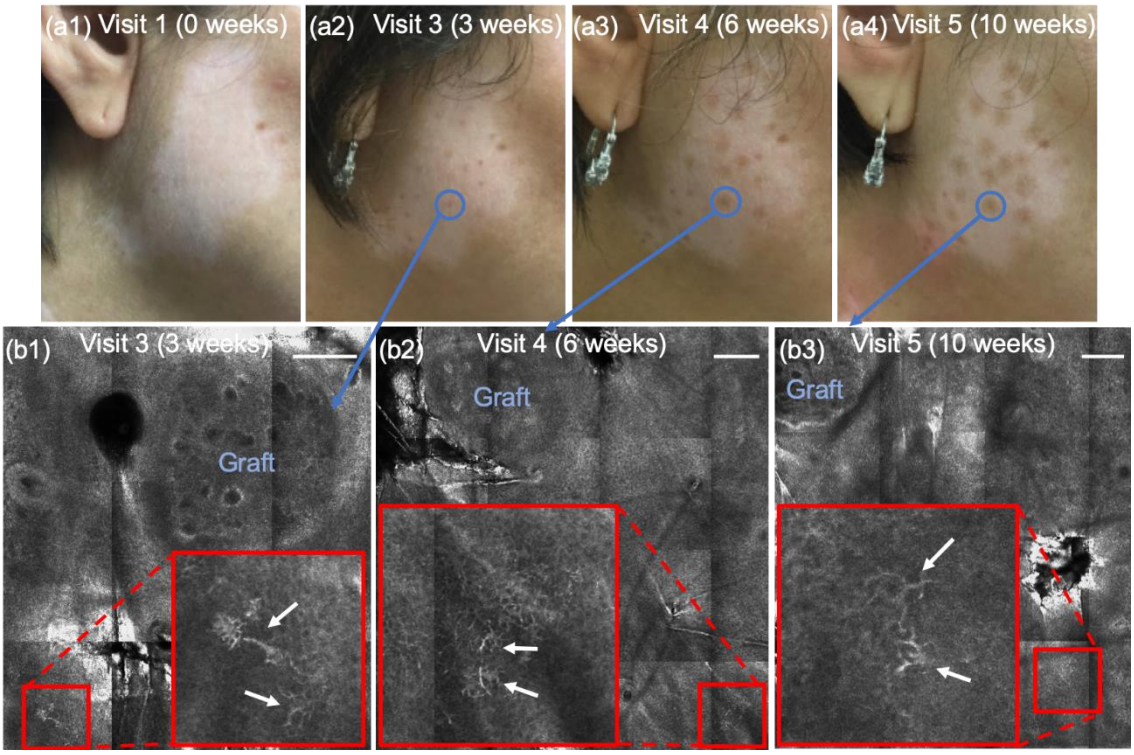

Figure 2.7. RCM images of dendritic melanocytes. Clinical images before treatment (a1), 3 weeks (a2), 6 weeks (a3), and 10 weeks (a4) post treatment initiation. Blue circles denote imaging location near graft. Dendritic melanocytes (insets, white arrows) were visualized 3 weeks (b1), 6 weeks (b2), and 10 weeks post treatment initiation (b3). Insets show enlarged view of the dendritic melanocytes. Scale bar is 200 μm for all large RCM images.

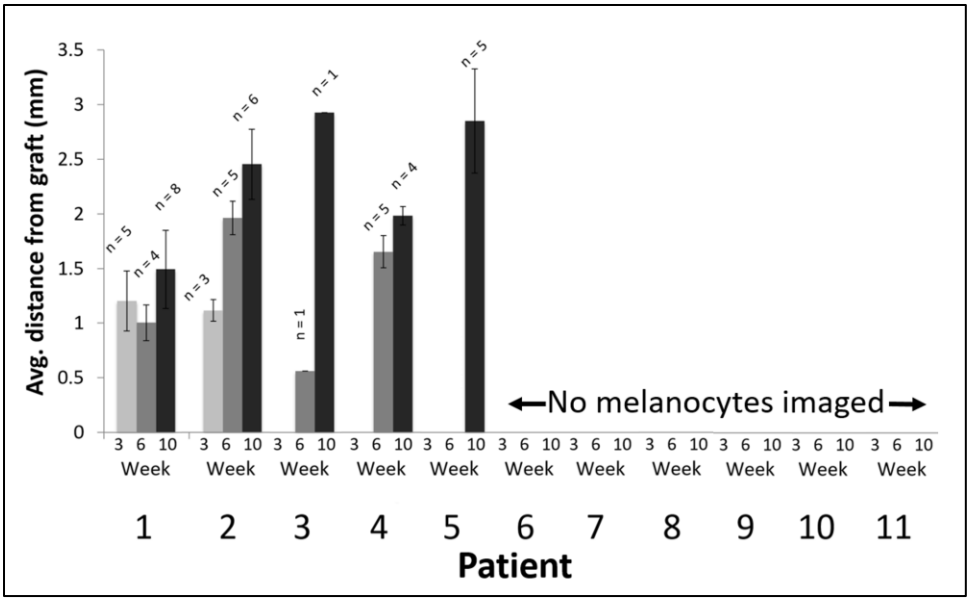

Figure 2.8. **Distance from micrograft of dendritic melanocytes after treatment initiation.** No dendritic melanocytes were seen in visits 1 or 2 for any patients. n = number of dendritic melanocytes seen in each case.

2.5. Discussion

To date, the study of keratinocytes in human vitiligo and their interactions with cells in the tissue microenvironment have largely been limited to traditional in vitro cultures and immunohistochemistry methods due to the lack of tools to assess cellular changes in situ. Here, we combine RCM and MPM *in vivo* imaging of stable vitiligo patients and scRNA-seq analysis to reveal a subpopulation of stressed keratinocytes in vitiligo lesional skin that is not present in nonlesional skin.

Mouse models and analyses of blister fluid from vitiligo patients have demonstrated the importance of the CXCL9/10 contribution in disease pathogenesis[69,73,87]. In humans, transcription of CXCL10 on whole skin increases in active lesions with prominent T cell infiltrates[88]. In stable depigmented whole skin, however, CXCL10 transcripts are not elevated[70]. CXCL9/10 were both expressed in vitiligo blister fluid but only CXCL9, not CXCL10, was a good predictor of vitiligo

disease activity[69]. While these methods have provided important insights into vitiligo pathogenesis, signals from small populations are lost from averaging of cell expression[89,90]. Our study using scRNA-seq demonstrates the existence of a small population of stressed keratinocytes in stable depigmented skin.

Evidence of a normalization in MPM mitochondrial clustering beta values after treatment initiation in patients that exhibited repigmentation supports the idea that if normal cell metabolism is restored via treatment, vitiligo skin is able to repigment. Absence of this metabolic restoration leads to vitiligo disease persistence, and should be a main target of study in the future.

Active dendritic melanocytes are visualized in vitiligo lesions that respond to treatment and can be monitored as they migrate farther from the micrografts. In no patients were melanocytes imaged by RCM at one time-point and then disappeared at a later time point. This finding supports the idea that the most likely reason for repigmentation failure after treatment is that the melanocytes are arrested from outward migration from the micrografts. Not that they migrate out and are destroyed by the immune system before they can repigment the vitiligo skin.

There are several limitations to this study. scRNA-seq analyses were performed on skin blisters which do not include fibroblasts and other dermal cell types and were only performed before treatment initiation. Blisters were collected as they represented a non-scarring method to collect vitiligo skin samples for analyses and had previously been shown to be sufficient to predict disease activity[69]. It is possible that intercellular communication networks between stress keratinocytes and fibroblasts affect vitiligo disease persistence, which is not addressed in this study. Also, the limited FOV of the MPM images means that a only small percentage of keratinocytes were assessed for mitochondrial clustering. Future studies with a larger imaging area

must be completed to more fully assess the extent of the metabolic alterations present in vitiligo skin.

Our data indicate that altered/stressed keratinocytes are present in the vitiligo skin microenvironment, and may be assessed using noninvasive *in vivo* MPM imaging and single cell RNA sequencing. In addition, active dendritic melanocytes can be monitored using noninvasive *in vivo* RCM imaging. These results are significant because they provide evidence for a potential link between stressed keratinocytes and vitiligo persistence and a rationale for targeting stressed keratinocytes as a treatment strategy in vitiligo. However, important questions remain. For example, when do stressed keratinocytes arise during vitiligo pathogenesis and how vitiligo treatment modalities affect stressed keratinocyte populations?

2.4.5 Main findings and significance

- Keratinocytes exhibit altered cellular metabolism in vitiligo skin compared to normal skin before treatment initiation according to mitochondrial clustering analysis performed on *in vivo* images.
- Keratinocytes displayed a return to normal cellular metabolism in vitiligo skin that repigmented after treatment, while kerationcytes in vitiligo skin that did not repigment showed a continuation of altered metabolism according to mitochondrial clustering analysis performed on *in vivo* images.
- Tracking of active dendritic melanocytes showed that when repigmentation doesn't occur after treatment, the reason is that the melanocytes do not migrate out and repigment the vitiligo skin.

- Single-cell RNA sequencing analysis revealed a sub-population of stressed keratinocytes in vitiligo skin not present in normal skin, a potential target for future vitiligo therapies.

3. Morphological features of common melanocytic nevi characterized by *in vivo* multiphoton microscopy

3.1 Background

Unrepaired defects in skin cell DNA can lead to the disruption of skin homeostasis, causing a variety of biological problems. For instance, common melanocytic nevi (also known as "moles"), involve BRAF V600E mutations that affect one of two alleles in every melanocyte of the nevus, indicating that a nevus is the result of a clonal outgrowth of a single melanocyte that acquired this mutation[91]. This type of nevi is a benign tumor of melanocytes, and is generally important only in relation to melanoma since it is the most important simulant both clinically and histologically[92]. Melanoma, a malignant tumor of melanocytes, is the deadliest form of skin cancer[93,94], and has been increasing in incidence rate since 1982 with no signs of decline[95]. Early stage melanoma can be difficult to distinguish from common melanocytic nevi, leading to large inter-observer variability[96-98], a persistent problem in melanoma diagnosis with a negative impact on patient care and management. Our group and others have demonstrated the potential of MPM for non-invasive imaging of pigmented lesions and detection of melanoma[24,99-101]. However, these studies include limited information about the MPM morphology and cytology of common nevi and no histology confirmation of the identified MPM features. Knowledge about the *in vivo* morphology of benign melanocytic nevi, which may differ significantly from the processed tissue morphology, is necessary for the differentiation of benign melanocytic nevi from early malignant melanomas.

In the work described in this chapter, we sought to explore the range of *in vivo* morphologies of different types of common melanocytic nevi in human skin in order to identify key MPM features of these skin lesions. Melanocytic nevi are composed of nevus cells, which differ from normal melanocytes as they are arranged in clusters, or "nests," and rarely if ever show dendritic processes[102]. Nevus cells lie in nests in the lower epidermis in junctional nevi and mainly in the dermis of intradermal nevi[102]. Compound nevi possess features of both junctional and intradermal nevi. Characterizing the *in vivo* morphology of these nevi is an important step in understanding more about nevi in evolution to melanoma.

3.2 Outstanding questions and aims

- What is the in vivo cellular morphology of benign pigmented lesions (nevi)?
- Are there optical biomarkers that distinguish benign senescent nevi from nevi in evolution to melanoma?
- What is the in vivo cellular morphology of the immune response in benign nevi?

Aims:

1) Identify histopathological features in the in vivo images of benign nevi.

2) Identify optical biomarkers to distinguish benign senescent nevi from nevi in evolution to melanoma.

3) Identify the immune response in the in vivo images of benign nevi.

3.3 Method of study

3.3.1 MPM imaging

We used the MPTflex MPM device for the *in vivo* imaging of the pigmented lesions in human skin (For details, see Chapter 2.3.1). The excitation wavelength used was 790 nm. We acquired the MPM data as z-stacks of en-face images from the stratum corneum to the superficial dermis. Typically, the FOV for each optical section was about 200×200 μm^2 and the step between the optical sections was 5 μm. Due to the limited FOV of each individual scan and in order to sample a larger area of the lesion, we acquired several stacks of images within each lesion. Thus, a total of 2,462 images were acquired for this study, corresponding to an average of 82 images for each nevus. Images were 512×512 pixels and were acquired at approximately 6 seconds per frame. For several lesions we acquired vertical cross-sectional, "histology-like" images from the stratum corneum to superficial dermis. These images were 1024×1024 pixels and were acquired at approximately 30 seconds per frame.

Thirty pigmented lesions in twenty-eight patients were imaged *in vivo* by MPM. In order to address inter-observer variability, all lesions that were not biopsied (19) were diagnosed as common nevi by three independent dermatologists. The pigmented lesions with a clinically suspicious appearance (11) were biopsied following MPM imaging. The histological diagnosis was performed by three independent dermatopathologists. The topographic location, pathologic characteristics along with MPM features corresponding to each case are summarized in Table 3.1.

Table 3.1. Patient age, location of the lesion, clinical diagnosis, MPM morphological features, and pathologic diagnosis of nevi.

Case no	Age (years)/ Gender	Location	Clinical diagnosis	MPM features			Pathology diagnosis
				Nests of nevus cells	Elongated rete ridges	Immune response	
1	57/M	back	JN	no	yes	no	x
2	34/F	leg	CN	yes	no	no	x
3	28/F	arm	JN	yes	no	no	x
4	22/F	arm	JN	yes	no	no	x
5	22/F	arm	JN	yes	no	yes	x
6	25/F	arm	JN	yes	yes	no	x
7	63/F	abdomen	JN	yes	no	no	x
8	24/M	arm	CN	yes	no	no	x
9	20/F	arm	CN	yes	no	no	x
10	23/F	arm	JN	no	yes	no	x
11	33/F	arm	CN	yes	no	no	x
12	57/F	leg	JN	no	yes	no	x
13	57/F	arm	JN	no	yes	no	x
14	55/M	chest	IDN	yes	no	no	x
15	23/M	arm	JN	yes	no	yes	x
16	57/F	back	IDN	yes	no	no	x
17	48/F	leg	CN	yes	no	no	x
18	89/M	leg	JN	no	yes	no	x
19	28/M	arm	IDN	yes	no	no	x
20	42/M	arm	AN	no	no	yes	IDN
21	47/F	arm	IN vs Melanoma	yes	no	no	IDN
22	67/F	abdomen	AN	yes	no	no	IDN
23	27/M	back	AN	no	no	yes	IDN
24	56/F	back	Nevus vs BCC	no	no	yes	IDN
25	23/F	abdomen	IDN	yes	no	yes	CN/IDN
26	46/F	back	AN	yes	no	yes	CN
27	27/F	arm	RN-CN	no	no	yes	RN-CN
28	89/M	arm	RN-IDN vs Melanoma	no	no	no	RN-IDN
29	52/F	back	AN vs melanoma	yes	yes	no	CN
30	46/M	abdomen	AN	no	yes	yes	CN

Abbreviations: JN-junctional nevus; CN-compound nevus; IDN-intra-dermal nevus; AN-atypical nevus; IN-irritated nevus; BCC-basal cell carcinoma; RN- recurrent nevus.

All *in vivo* measurements were conducted according to an approved institutional review board protocol of the University of California–Irvine (HS No. 2011-8494) with written informed consent obtained from all patients.

3.3.2 Image analysis

We used ImageJ[103] for both the qualitative and quantitative analysis. The qualitative analysis included: 1) basic processing tasks of the MPM images for enhancing contrast and highlighting features of interest; 2) comparison of the MPM and histologic images of biopsied nevi in order to identify and correlate their morphological features.

The quantitative analysis included measurements of:

1) Nevomelanocytes sizes. We calculated the average cell diameter using a semi-automatic segmentation method within ImageJ using the following procedure for nevomelanocyte segmentation: Gaussian blur (sigma: 2.0), manual outline selection of cell(s) to be measured, signal thresholding based on signal in outlined area, image binarization, erosion and/or dilation (if necessary to outline complete cell), watershed (if necessary to distinguish neighboring cells), Feret's diameter measurement for each segmented cell. We used a two-tailed t-test to determine whether the nevomelanocyte sizes in the junctional and compound nevi were significantly different from size of nevomelanocytes in the nests of intradermal nevi. We combined the results from junctional and compound nevi into one group since in compound nevi, MPM captured mostly the epidermal component of the nevus, namely the epidermal nests.

2) Nevomelanocyte nests sizes. We measured the major axis of each nest at its maximum imaged size as determined from the MPM cross-sectional en-face images. The average size of each nest was calculated based on two independent measurements. We used a two-tailed t-test to

determine whether the nevomelanocyte nest sizes were: i) significantly different in the two groups of junctional/compound and intradermal nevi; ii) significantly changed within the imaging depth.

3) Percentage of nevomelanocytes outside the nests. For each en-face image acquired within the stack, we measured the number of cells inside the nests through the ratio of the nest area to the average area of the melanocytes within the nest. We counted manually the sparse melanocytes outside nests and calculated their percentage by dividing their number by the total number of nevomelanocytes located within nests for each imaging volume.

3.4 Results

We analyzed both qualitatively and quantitatively the MPM images acquired *in vivo* in thirty common nevi in human skin (see Table 3.1 for a summary of the lesion location and diagnosis). Beside the enhanced pigmentation of keratinocytes, which may also be present and imaged in pigmented normal skin[24,62], the MPM features of nevi included: 1) nests of nevomelanocytes; 2) elongated rete ridges epidermal extensions into the underlying connective tissue) and 3) an immune response in the form of melanophages and inflammatory cells in the dermis. These features are discussed below. Details about the location, diagnosis, etc. for each lesion the images shown have been acquired from can be found in Table 3.1 based on the case number provided.

3.4.1 Qualitative assessment of nevomelanocyte nests

The presence or absence of nests was consistent in all the stacks acquired in 60% of the patients. In the rest of the patients, the nests of nevus cells were imaged on average in 49% of the total number of stacks acquired. The different cytological structures of the nevomelanocyte nests

can be visualized in the representative MPM images from a junctional nevus in Figure 3.1 and from two intradermal nevi in Figure 3.2. In Figure 3.1 (Case 6), the nest imaged in the junctional nevus is located at the dermo-epidermal junction, clearly attached to the epidermis based on its close proximity to the basal cells (pigmented cells visualized through bright fluorescence from melanin, Figure 3.1b).

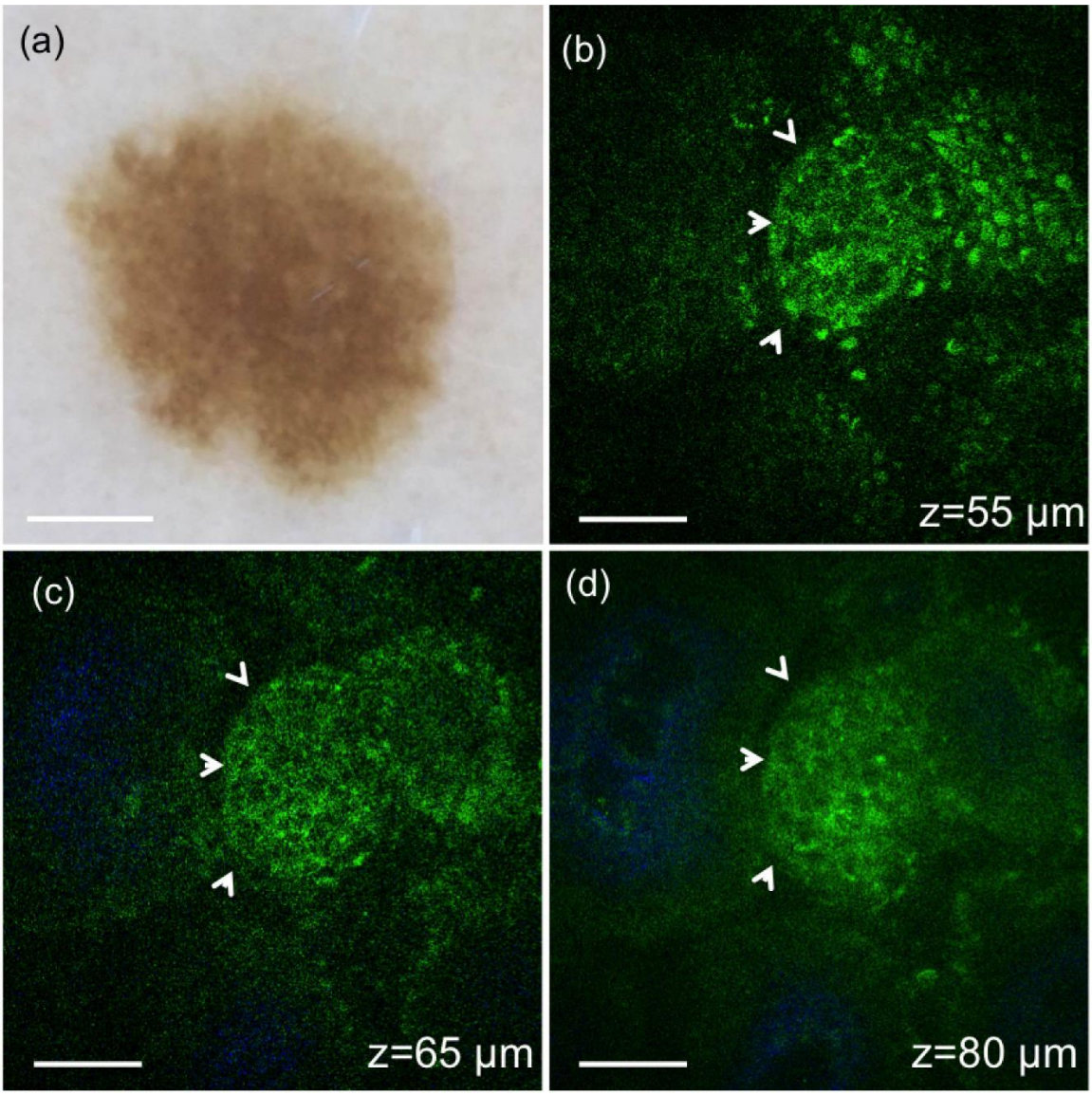

Figure 3.1. *In vivo* MPM of nevomelanocytes in a junctional nevus. (a) Clinical image (Dermlite FOTO, Dermlite, Inc), Case 6. Scale bar is 1 mm. (b-d) MPM images of the nevus in (a) showing a nest of nevomelanocytes (arrows) at different depths surrounded by pigmented keratinocytes (green, visualized through bright fluorescence from melanin) (b) and dermal papillae (blue) collagen (c-d). Scale bar is 40 μm.

Figure 3.2 (a1-a4) shows nevomelanocytes arranged in nests in the papillary dermis of an intradermal nevus imaged by MPM (Case 25 in Table 1). Figure 3.2 (b1-b4) includes a representative example of MPM images that show sparse nevomelanocytes located outside the nests of an intradermal nevus (Case 22). The cytological appearance of nevomelanocytes was consistent in all predominantly intradermal nevi and correlated well with histology. In an effort to provide a side-by-side correlation of the MPM and histology images of nevomelanocytes, we imaged *ex vivo* by MPM unstained tissue sections (obtained from the remaining paraffin blocks) of the biopsied lesions included in this study. We compared the MPM images with histologic (H&E stained) images of adjacent tissue sections. Figure 3.3 illustrates an example of such images acquired from the same nevus shown in Figure 3.2 (a1-a4, Case 25). Although the same clusters of nevomelanocytes can be visualized in both MPM and corresponding histologic images, the MPM images clearly show the difference between the nevomelanocytes appearance in the processed tissue (Figure 3.3) and their live morphology captured by MPM *in vivo* (Figure 3.2 a3).

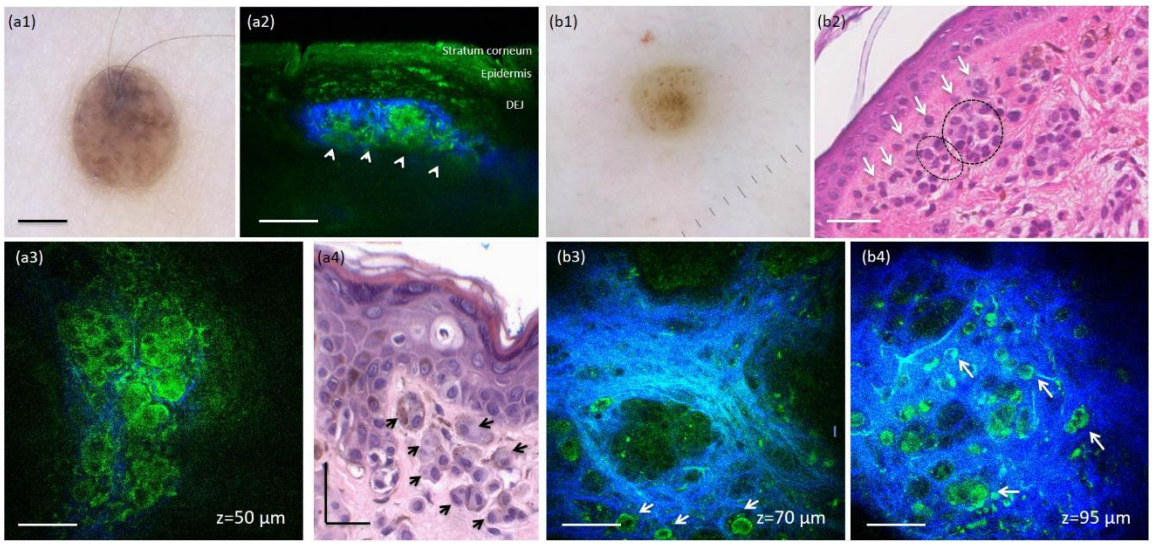

Figure 3.2. ***In vivo*** **MPM of nevomelanocytes in intradermal nevi.** (a1) Clinical image (Dermlite FOTO, Dermlite, Inc), Case 25. Scale bar is 2 mm. (a2, a3) Vertical cross-section (a2) and en-face (a3) MPM images of the nevus in (a1) showing a nest (arrows) of epithelioid nevomelanocytes displaying rounded large nuclei and surrounded by collagen (blue) in the papillary dermis. (a4) Hematoxylin and eosin (H&E) histological section of the lesion in (a1) showing nests of epithelioid nevomelanocytes in the papillary dermis; (b1) Clinical image (Dermlite FOTO, Dermlite, Inc), Case 22. (b2) H&E histological section of the lesion in (b1) showing sparse melanocytes (arrows) around a nest of nevomelanocytes in the papillary dermis (circle); Scale bar is 40 µm. (b3, b4) En-face MPM images of the nevus in (b1) showing sparse nevomelanocytes (arrows) around nests of nevomelanocytes surrounded by collagen (blue) in the papillary dermis at depths of 70 µm (b3) and 95 µm (b4). Scale bar is 40 µm in all MPM images.

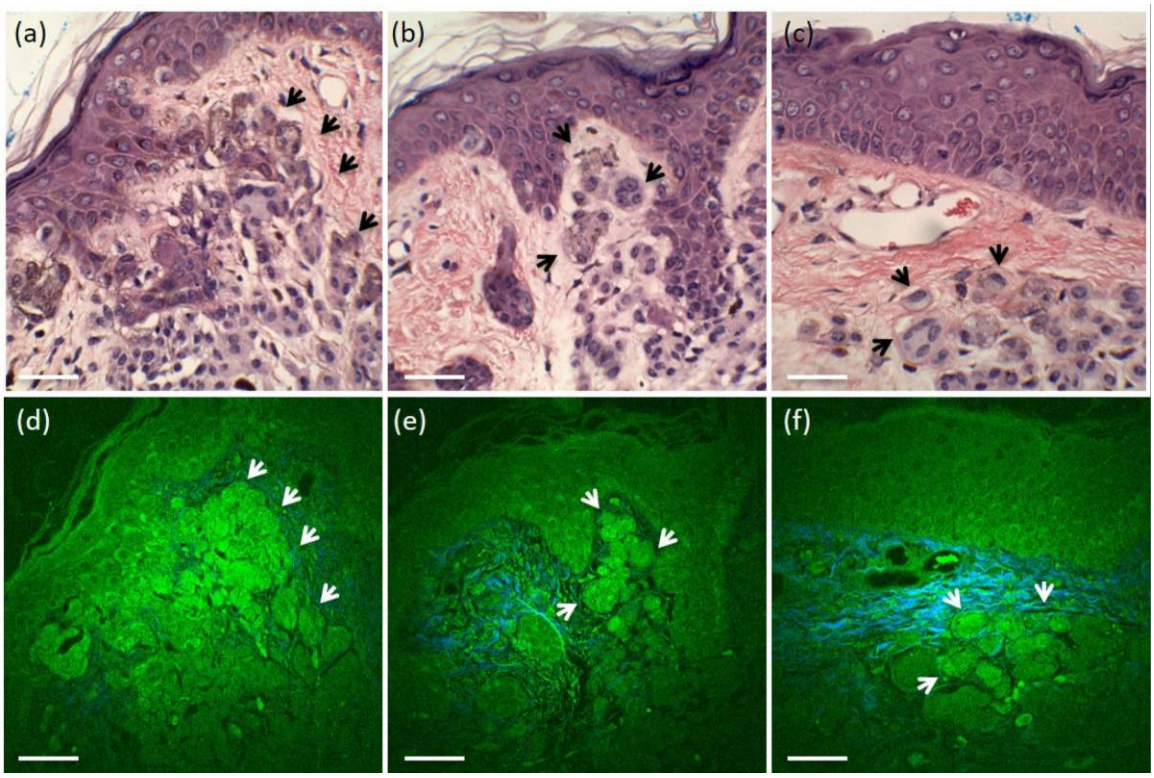

Figure 3.3. H&E and MPM images of adjacent tissue sections from an intradermal nevus. (a-c) H&E histological sections of the lesion shown in Fig. 3.2 (Case 25) showing nests of nevomelanocytes in the papillary dermis (arrows); (d-f) MPM images of the adjacent tissue sections in (a-c) showing the same nevomelanocytes (arrows) in the papillary dermis. Scale bar is 40 μm.

3.4.2 Size of the nevomelanocyte nests

There was no significant difference between the size of nevomelanocyte nests in the two groups of junctional/compound and intradermal nevi. In all nevi, the size of the vast majority of the nests (~90%) was between 20 to 80 μm and did not significantly change with the imaging depth. Nine of the thirteen largest nests were located in intradermal nevi and had sizes within the range of 85-170 μm. This analysis included 78 nests visualized in 13 junctional/compound nevi and 62 nests in 6 dermal nevi. Figure 3.4 shows the distribution of the nevomelanocyte nest diameters measured in the two groups of nevi (junctional/compound vs dermal) for different patients.

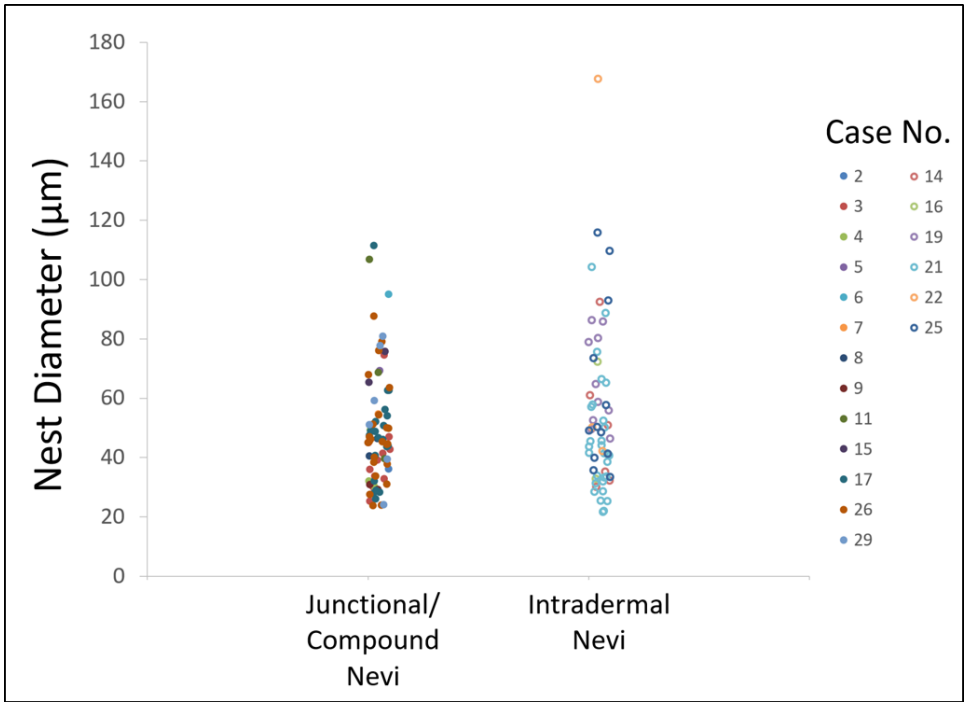

Figure 3.4. Distribution of nevomelanocyte nest diameters in junctional/compound and intradermal nevi. Data represent individual nest diameter measurements for each lesion. Case numbers correspond to those listed in Table 3.1.

3.4.3 Size of nevomelanocytes.

The nevomelanocytes were significantly smaller (p=0.0001) in junctional and compound nevi (8.94 ±2.9 µm) compared to the nevomelanocytes in the intradermal nevi (14.08±3.3 µm). Figure 3.5 shows the distribution of the nevomelanocyte diameters for the two groups of nevi for different patients.

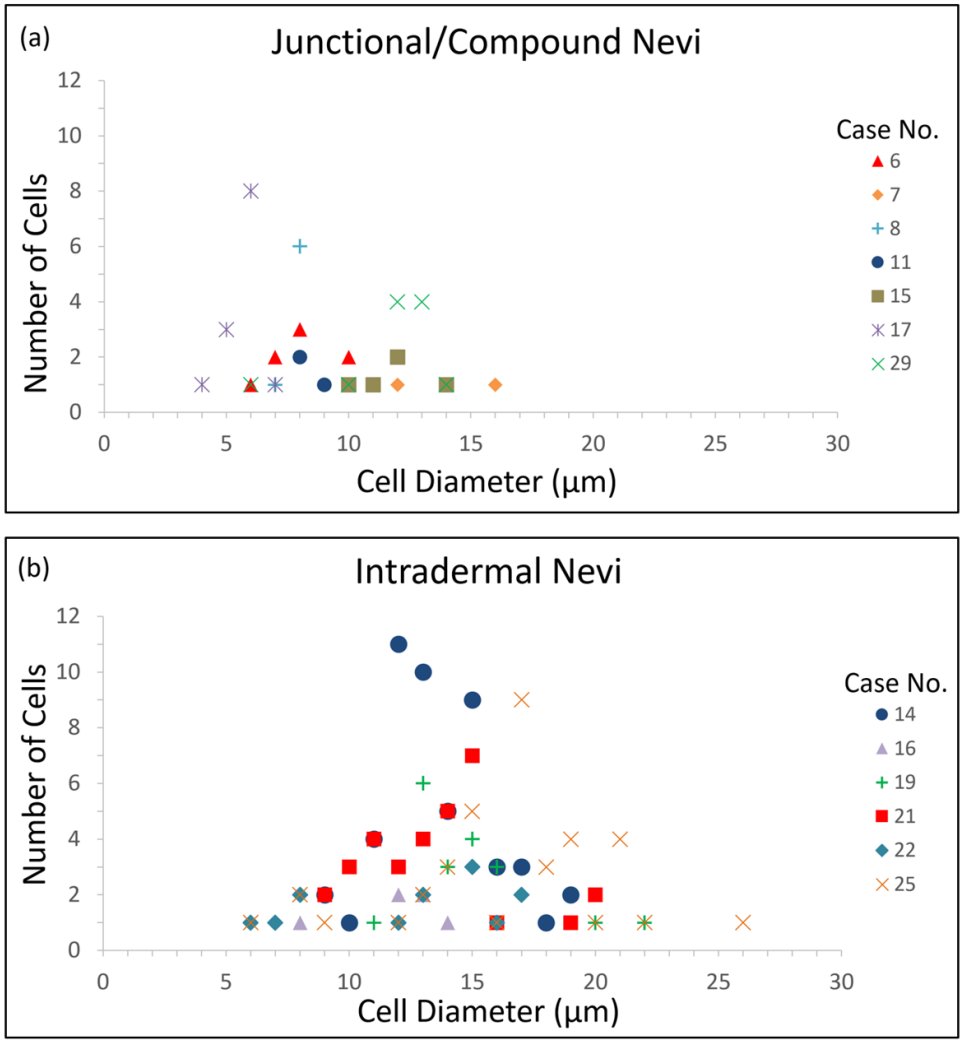

Figure 3.5. Distribution of nevomelanocyte cell diameters in junctional/compound and dermal nevi. Data represent number of cells with different cell diameters measured in junctional/compound nevi (a) and intradermal nevi (b) for each lesion. Case numbers correspond to those listed in Table 3.1.

3.4.4 Percentage of nevomelanocytes outside the nests.

Most of the nests (76%) were rather small including less than 45 nevomelanocytes. The nests with the largest number of nevomelanocytes (100-125) were located in intradermal nevi. In most nevi (72%), the nevomelanocytes were located exclusively inside the nests. The rest of nevi

showed nevomelanocytes located both within and outside nests. The number of sparse melanocytes outside nests represented less than 5% of those located within the nests.

3.4.5 Elongated rete ridges

Another specific feature we imaged in nevi was elongated rete ridges. We identified this feature exclusively in junctional nevi. We compared the elongation of the rete ridges based on their morphology in the en-face images. At the dermo-epidermal junction, the en-face MPM images show a horizontal sectional view of the rete ridges. In this view, the rete ridges appear as ring-like structures of basal keratinocytes surrounding the dermal papilla. In the nevi with long rete ridges, this morphology was visualized as deep as ~150 μm, the common depth limit for MPM imaging of nevi. For the nevi with shorter rete ridges, the en-face images captured at ~150 μm depth showed presence of collagen and elastin fibers, i.e. the morphology characteristic to the skin dermis. Representative images that illustrate the assessment of rete ridges are included in Figure 3.6. We identified elongated rete ridges in 6 out of 11 junctional nevi. Nests of nevomelanocytes were not visualized in 5 of these nevi, likely due to their deeper location at the tips of the rete ridges.

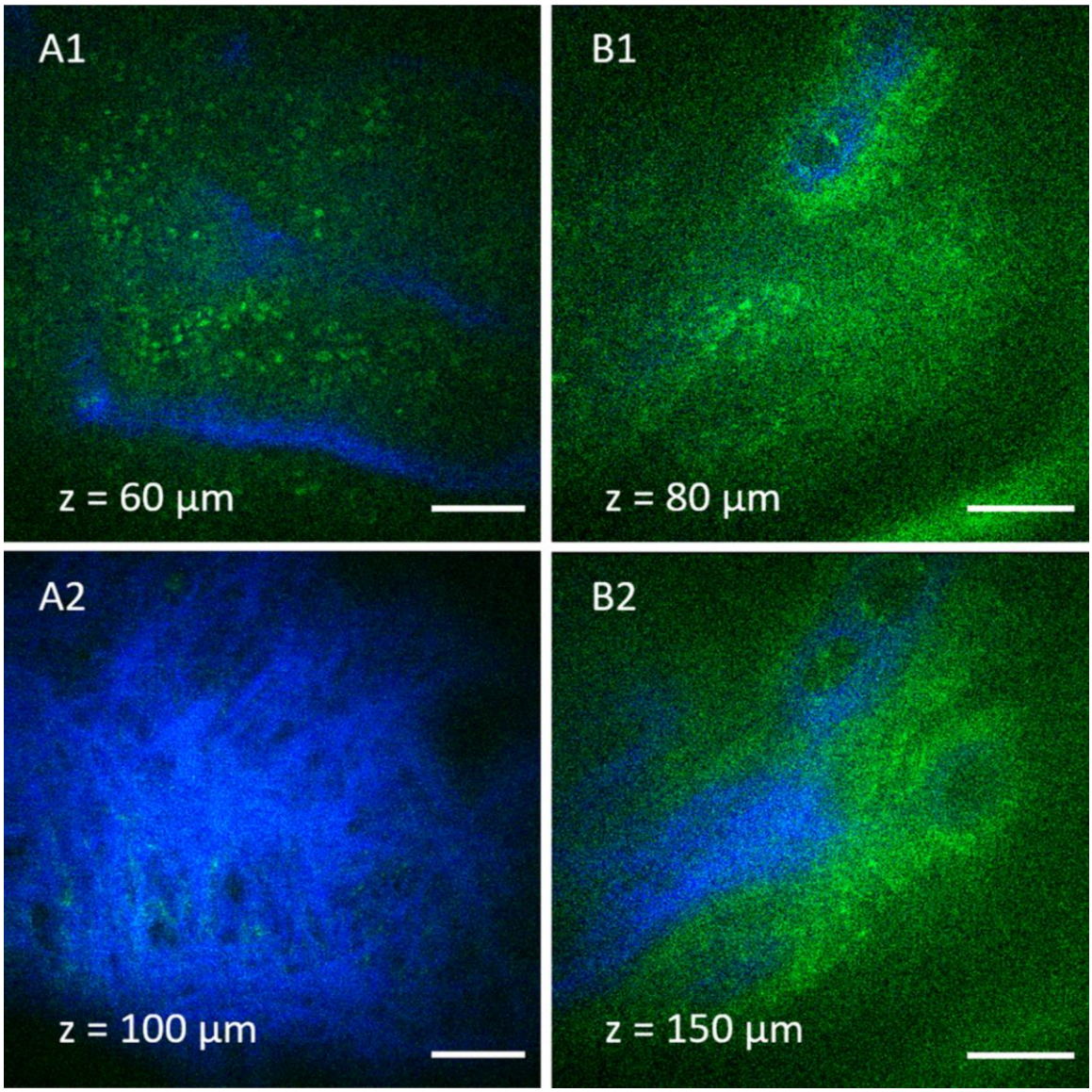

Figure 3.6. Assessment of rete ridges in nevi based on en-face *in vivo* MPM images. (A) MPM images of a nevus (Case 17) at a depth of 60 µm below the skin surface showing basal keratinocytes (green) surrounding dermal papilla (blue) (A1) and at 100 µm depth in the superficial dermis showing collagen (blue) and elastin (green) fibers (A2). (B) MPM images of a nevus (Case 13) at a depth of 80 µm below the skin surface showing basal keratinocytes surrounding dermal papilla (blue) (B1) and at 150 µm depth still showing the morphology of the rete ridges in the en-face view (basal keratinocytes surrounding dermal papilla), a sign of elongated dermo-epidermal junction and thus, of the rete ridges (B2). Scale bar is 40 µm.

3.4.6 Immune response

We captured the immune response in the form of dermal infiltration of inflammatory cells and melanophages. The presence or absence of the immune response was consistent in all the stacks acquired in 80% of the patients. In the rest of the patients, the inflammation was captured on average in 53% of the total number of stacks acquired.

MPM imaging revealed presence of inflammatory cells in two of the nevi imaged *in vivo* by MPM. These nevi were histologically diagnosed, one as residual dermal melanocytic nevus (Case 20), the other one as recurrent compound melanocytic nevus (Case 27). Figure 3.7 (b-e) shows dermal cells visualized by MPM *in vivo* in the recurrent compound melanocytic nevus (Case 27), along with a nest of nevomelanocytes at the dermo-epidermal junction. The appearance of dermal cells is different from the nevomelanocytes imaged in this lesion or in others (Figure 3.1, 3.2, 3.3) and based on correlation with immunohistochemistry (Figure 3.7), they are most likely CD3 T-cells. In the MPM images, these cells were approximately round in shape, were about 10-12 μm in size and arranged in clusters. Unlike nevomelanocytes, they appear dispersed rather than closely packed and their nuclei are not well resolved.

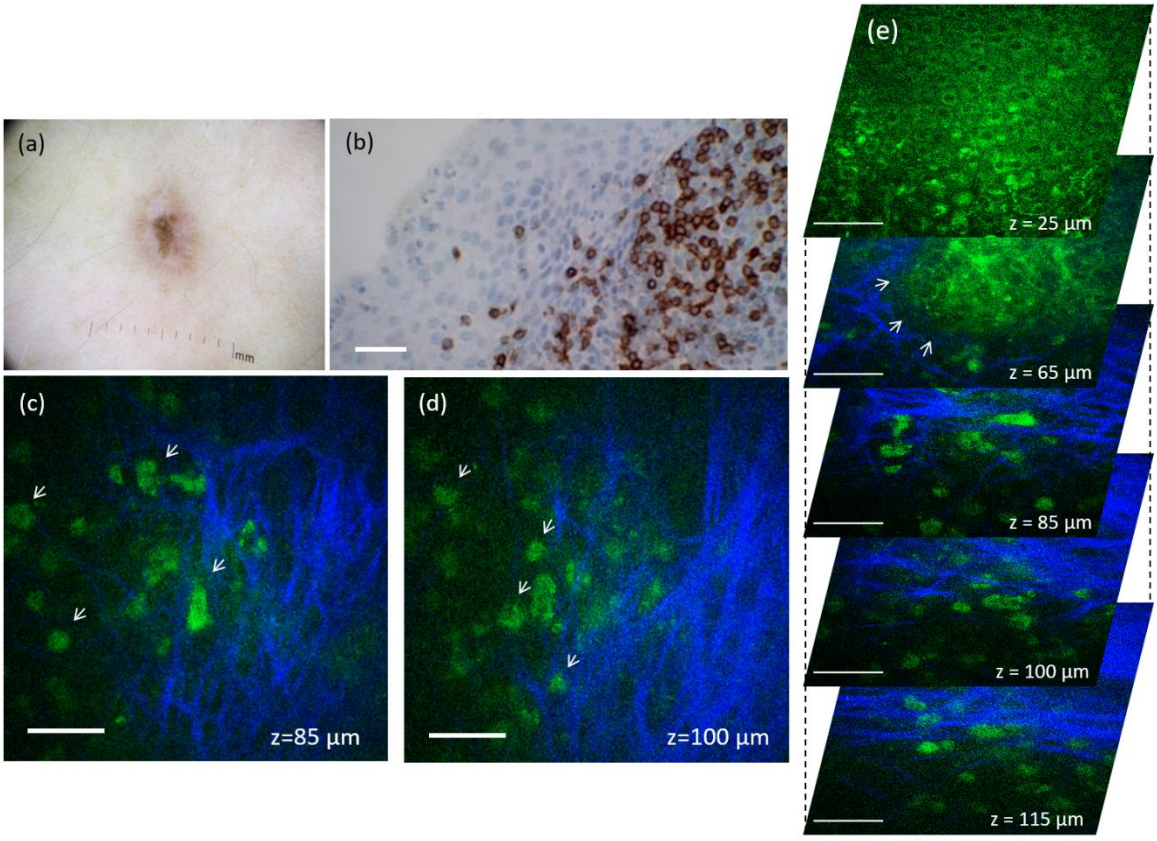

Figure 3.7. ***In vivo*** **MPM of lymphocytes in a recurrent compound nevus.** (a) Clinical image (Dermlite FOTO, Dermlite, Inc), Case 27. (b) Immunohistochemistry image showing CD3-positive T-cell lymphocytes in the superficial dermis; (c, d) En-face MPM images of the nevus in (b) showing inflammatory cells (arrows) in the superficial dermis at a depth of 85 (c) and 100 µm (d). (e) A stack of en-face MPM images acquired at different depths from the nevus in (b) showing a nest of nevomelanocytes at the dermo-epidermal junction (arrows) and inflammatory cells in the superficial dermis. Scale bar for in all images is 40 µm.

MPM imaging also revealed the presence of melanophages in the dermis of eight nevi. Six of these nevi were biopsied and histologically diagnosed as compound (2) and intradermal (4) nevi. In the MPM images, melanophages had an irregular shape, were about 18-20 µm in size and were generally bright due to fluorescence from their abundant melanin content. They were arranged in clusters and some of them appeared dendritic. Their appearance correlated well with the melanophages identified in the histological images. Representative example of MPM images

showing melanophages imaged in an intradermal nevus is shown in Figure 3.8 (c-d, Case 23). Presence of melanophages in this lesion was confirmed by histology (Figure 3.8 b).

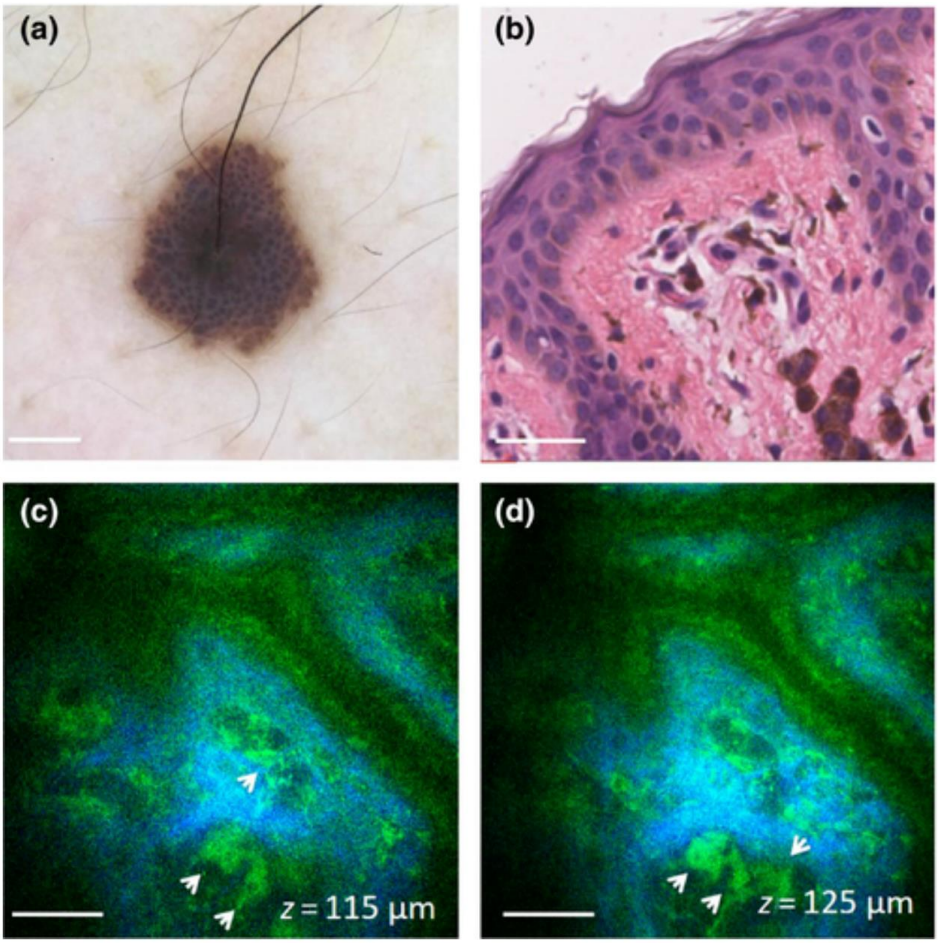

Figure 3.8. *In vivo* MPM of melanophages in an intradermal nevus. (a) Clinical image (Dermlite FOTO, Dermlite, Inc), Case 23. (b) H&E histological section of the lesion in (a) showing nests of melanophages in the papillary dermis; Scale bar is 40 µm. (c,d) En-face MPM images of the nevus in (a) showing melanophages (arrows) in the papillary dermis at a depth of 115 µm (c) and 125 µm (d). Scale bar is 40 µm.

Establishing the cytological morphology of nevomelanocytes and immune response by comparison with histopathology allowed us to accurately identify these cells in nevi that were not

biopsied. Representative MPM images of nevomelanocytes and melanophages imaged in such nevi are shown in Figure 3.9 and 3.10, respectively.

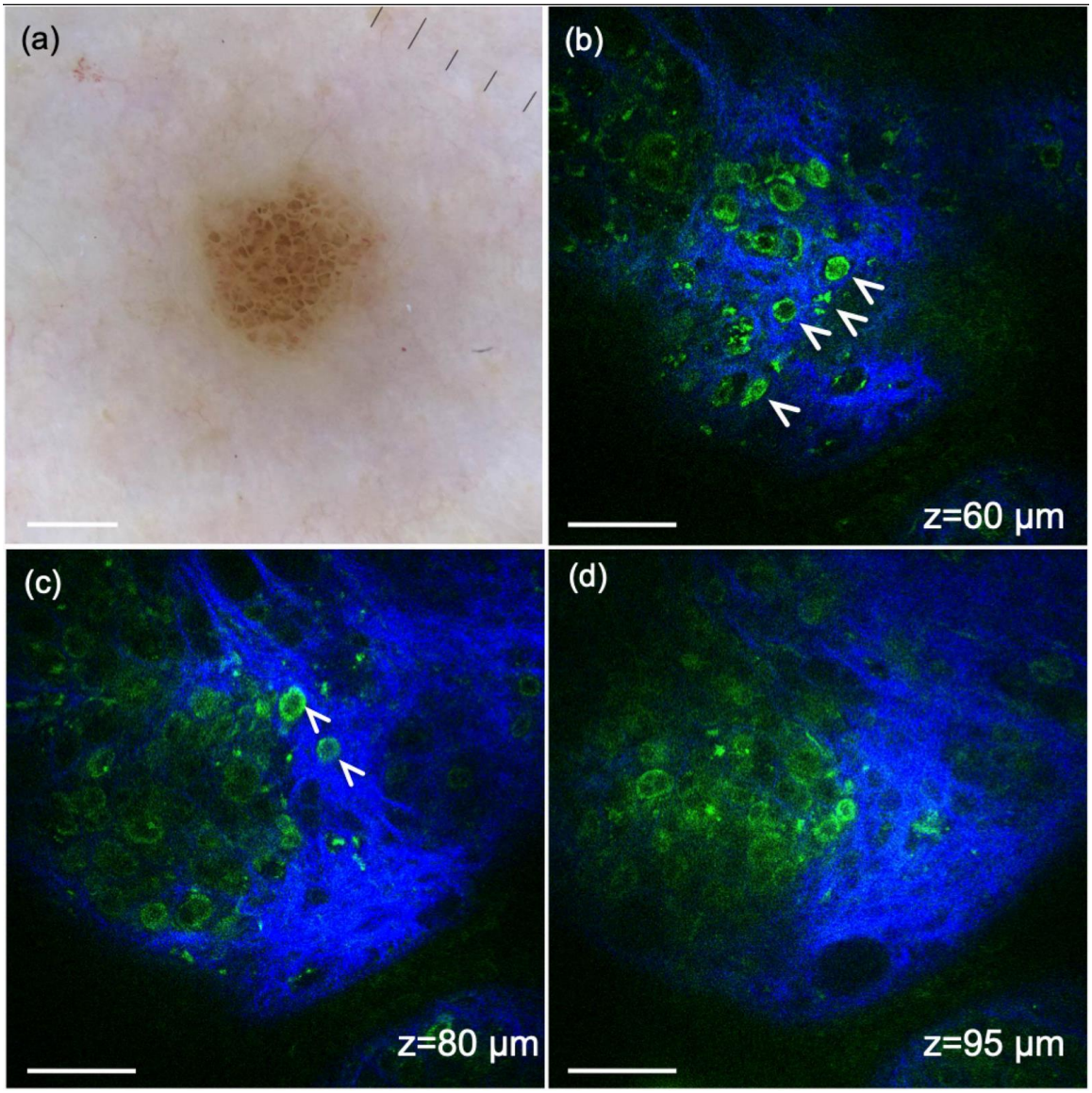

Figure 3.9. *In vivo* MPM of nevomelanocytes in an intradermal nevus. (a) Clinical image (Dermlite FOTO, Dermlite, Inc), Case 14 (b-d) En-face MPM images of the nevus in (a) showing nests of epithelioid nevomelanocytes (green) displaying rounded large nuclei and surrounded by collagen (blue) in the papillary and superficial dermis at depths of 60 µm (b), 80 µm (c) and 95 µm (d). Arrows indicate sparse nevomelanocytes located outside the nest. Scale bar is 40 µm.

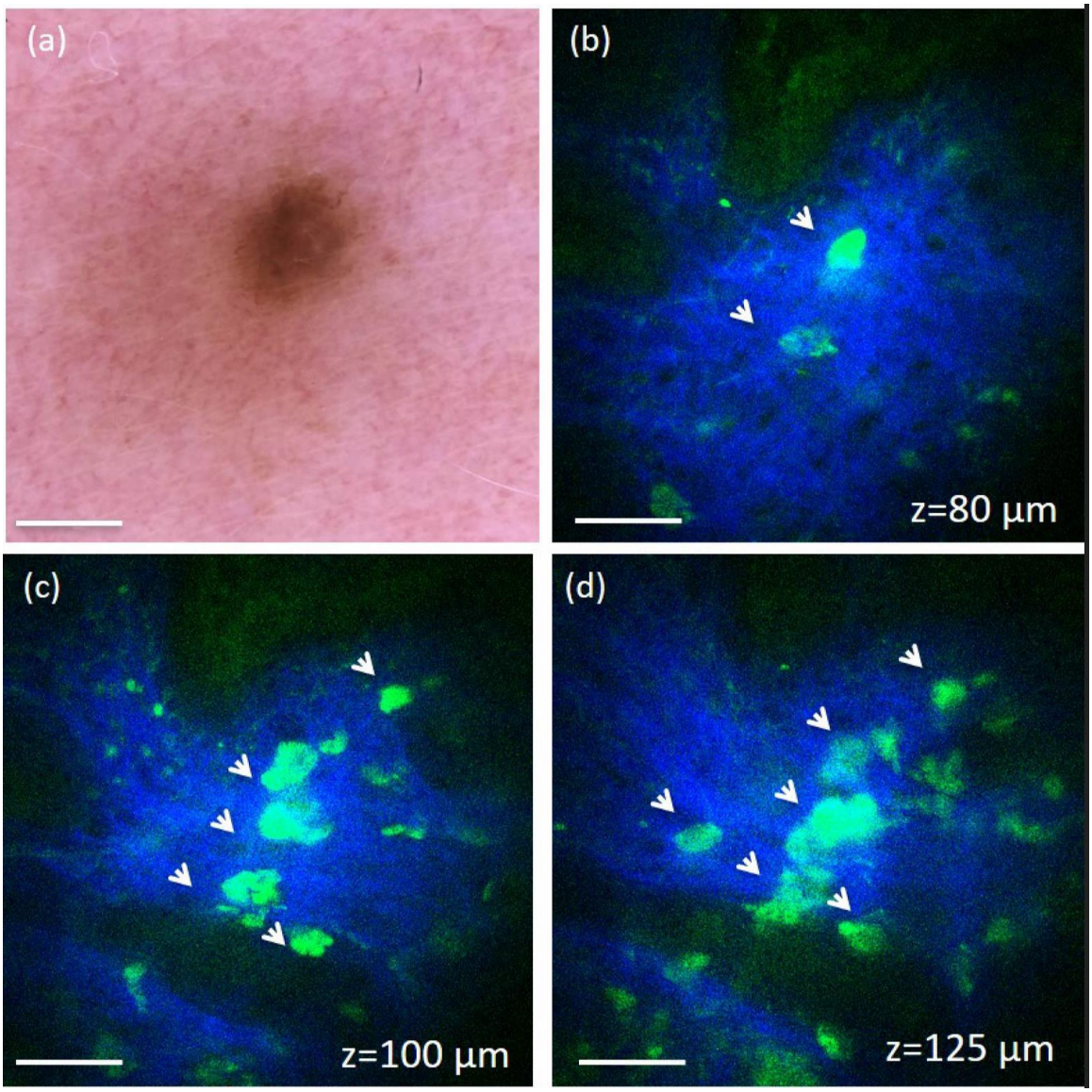

Figure 3.10. ***In vivo*** **MPM of melanophages in a junctional nevus.** (a) Clinical image (Dermlite FOTO, Dermlite, Inc), Case 5. Scale bar is 2 mm; (b-d) En-face MPM images of the nevus in (a) showing melanophages (arrows) in the papillary and superficial dermis at a depth of 80 µm (b), 100 µm (c) and 125 µm (d). Scale bar is 40 µm.

3.5 Discussion

In this study, we assessed both qualitatively and quantitatively the cytological and morphological features of common nevi in human skin as visualized by *in vivo* MPM.

Nests of nevomelanocytes represented the most predominant feature captured by MPM in most nevi. We assessed several quantitative parameters related to the size of nevomelanocytes, the size of the nests and the percentage of nevomelanocytes located outside the nests. The nevomelanocytes of intradermal nevi were significantly larger and presented larger nuclei than the nevus cells in junctional and compound nevi. Their appearance correlated well with the corresponding histological images and, based on their large size and epithelioid shape, seemed to represent the superficial component (type A melanocytes) of so-called "maturation"[104]. This term is commonly used in histology to indicate the progression of nevomelanocytes from large epithelioid cells in the papillary dermis to smaller, lymphocytes-like cells in the superficial dermis and spindle Schwann like-cells deeper in the dermis. In all nevi, the size of the vast majority of the nests (~90%) was in the range of 20-80 μm and did not significantly change with the imaging depth. The nevomelanocytes nest size can be a potential relevant metric in differential diagnosis of benign and malignant melanocytic nevi[105]. The limited imaging depth of MPM in skin (~200 μm) did not allow us to measure a potential change in size of the nevomelanocyte nests with depth, but we were able to show that the majority of melanocytes were located within the nests. Published studies have suggested that melanocytes within nests express the senescence marker p16[106]. This observation indicates that the metric related to percentage of nevomelanocytes outside the nests may be used to assess the nevi in evolution. Metrics based on size of nests and/or the percentage of cells located outside nests may also be used as criteria to distinguish nevi from melanoma. This

hypothesis is based on observations from histology[107] and from our previously published work on MPM imaging of nevi and melanoma[24], but it needs to be tested in further studies.

Elongated rete ridges, a known histological feature of junctional nevi[104], were imaged by MPM in about half of these types of nevi. They generally hindered the imaging of nevomelanocytes nests. Thus, while nests of nevomelanocytes were imaged in most of the nevi, they were not captured in most nevi that showed elongated rete ridges. This was likely due to the location of the nevomelanocytes at the tips of the rete ridges[104] that were too deep to access by MPM. Limited penetration depth of MPM was also likely the reason we did not capture the nevomelanocytes in three out of eight nevi diagnosed as predominantly intradermal.

Inflammatory infiltrates may develop in some types of melanocytic lesions such as recurrent and residual melanocytic nevi that involve regression[108]. MPM was able to capture dermal cells with a distinct morphology in a regressing nevus in approximately the same location where infiltrating CD3+ cells were observed on histology. T cell infiltration in nevi is often a sign of regression or of an anti-melanocyte immune response, and can be indicative of a good response to immunotherapy[109]. Although these observations suggest that MPM can definitively identify T cells surrounding nevi based on their distinct morphology, more extensive imaging of skin lesions with characteristic T cell infiltrates such as cutaneous T cell lymphoma (CTCL) is required to validate this imaging signature. Melanophages, commonly visualized histologically in common nevi[104], were imaged by MPM in the papillary and superficial dermis of two junctional, one compound and four intradermal nevi. We distinguished the melanophages in the MPM images of the intradermal nevi by comparing their cellular morphology with the melanophages identified in the histological images. Identification of melanophages through comparison of the MPM and histological images allowed us to accurately identify these cells in the junctional nevi that were

not biopsied. Similarly, establishing the cytological morphology of nevomelanocytes by comparison with histopathology was valuable in accurately identifying these cells in nevi that were not biopsied. Unlike the nests of nevomelanocytes, dermal melanophages do not represent a specific morphological feature of common nevi. However, they commonly can be indicative of prior inflammatory response in common nevi or regression of melanocytes.

The qualitative and quantitative parameters proposed in this study are instrumental in a future study on an expanded number of lesions in order to evaluate the potential of MPM as a non-invasive, label-free imaging tool for diagnosis of pigmented lesions. Such a study would also need to address current technical limitations of the MPM clinical imaging, particularly the reduced scanning area and penetration depth. Improved penetration depth would allow visualization of nevomelanocytes at the tips of elongated rete ridges, immune response of deeper dermis and the evaluation of maturation within deeper nest. Dispersion compensation to decrease the laser pulse duration[110,111] and adaptive optics[112] are among approaches that have been reported recently for enhancing penetration depth in thick, scattering tissue. Sampling large areas of the lesions is critical to avoid false-negative diagnoses, as pigmented lesions are often non-uniform. We have recently proposed an approach for addressing this limitation by designing and developing an MPM imaging prototype device that provides rapid scanning of large skin tissue areas, while maintaining submicron resolution[65].

In conclusion, this study illustrates and discusses qualitative and quantitative cytologic and morphologic metrics in common nevi as visualized by MPM. The qualitative descriptors complement the MPM features previously described in melanoma. A large database of MPM descriptors to characterize a broad range of pigmented lesions is critical in the process of discriminating melanoma from look-alike lesions by *in vivo* MPM imaging. The quantitative

parameters proposed in this study to characterize nevi imaged *in vivo* by MPM may be extremely relevant in future studies for assessing nevi in evolution or for distinguishing benign nevi from early stage melanoma.

3.6 Main findings and significance

- MPM morphological features of nevi identified in the *in vivo* images include: larger nevomelanocytes and nevomelanocyte nuclei in intradermal nevi compared to junctional and compound nevi, similar nevomelanocyte nest sizes (20-80 μm) in all three types of nevi, and elongated rete ridges. These features are a compliment to the features previously described in melanoma and can be used in the process of discriminating melanoma from simulants by *in vivo* imaging.
- The percentage of nevomelanocytes located within nests for each lesion is a metric that may distinguish benign senescent nevi from nevi in evolution to melanoma. Quantitative changes in this feature may be helpful in future studies assessing nevi in evolution to become melanoma.
- An immune response in the *in vivo* images was visualized in two forms: (1) irregularly shaped cells, 18-20 μm in size, exhibiting bright fluorescence, most likely melanophages, and (2) cells with a round in shape, 10-12 μm in size, and arranged in clusters, most likely T cells. Cellular morphology correlated with histopathology and immunohistochemistry. Visualization of immune *response in vivo* in nevi could be used in future studies as a biomarker related to response to immunotherapies.

4. Characterization of melasma by *in vivo* multiphoton microscopy

4.1 Background

Another skin condition related to alterations in normal pigment biology in human skin is melasma. This condition is most prevalent in women with a familial predisposition who live in climates that receive abundant sun exposure[113,114], pointing to the influence hormonal activity[115,116], genetics[115,117], and UV light exposure[118,119] have on occurrence. Visually, melasma is seen as irregular light to dark brown patches frequently found on the sun-exposed areas of the face[10]. The patches are the result of hyper-functional melanocytes that produce and deposit excessive amounts of melanin in the epidermis and/or dermis.[19] The presence of these hyper-functioning melanocytes has been shown to be due to a disruption in the normal Wnt signaling pathway, a key regulator of melanin production[120]. In short, a downregulation in the expression of the Wnt signaling antagonist "Wnt inhibitory factor-1" (WIF-1) gene, which is only expressed in human keratinocytes and dermal fibroblasts, leads to enhanced melanin production and deposition in melasma[121,122].

To date, there is no reliable method to determine the depth of the excess melanin within the skin (epidermal and/or dermal), a key factor among others that make the treatment of melasma a difficult challenge. Biopsy is commonly not an option due to cosmetic reasons, and a heterogeneous melanin distribution is often present, which would require multiple sampling sites. Both a dermatoscope, and a Wood's lamp are commonly used by dermatologists for melasma diagnosis as non-invasive alternatives to biopsy[18,123]. However, dermatoscopic inspection is

limited to the surface of the skin, and several studies have shown that Wood's lamp examination is not accurate in determining the depth of melanin pigment[19] and cannot predict treatment response[20].

Because of these limitations, optical imaging technologies such as MPM and RCM hold the potential to improve the accuracy of melasma diagnosis and impact its treatment. RCM images are sufficient for the overall assessment of tissue structure and the technology has been employed in several studies for imaging melasma[124]. Findings included increased pigmentation of the epidermis in melasma lesions compared to adjacent normal skin, as well as presence of melanophages in lesions diagnosed by histopathology as dermal/mixed melasma[125,126]. RCM was also evaluated as a potential imaging tool for monitoring treatment efficacy of melasma[127-129].

Compared to RCM, the TPEF and SHG signals used in MPM provide enhanced contrast, facilitate image interpretation, and allow evaluation of elastosis and development of quantitative analysis strategies based on MPM molecular contrast as recently shown by our group and others[24,62,130]. Yet research on melasma using MPM is rare due to its almost nonexistent presence in dermatology clinics. The goal of this chapter is to demonstrate MPM's ability to characterize melasma skin in its native environment to learn more about the basic biology of the disease.

4.2 Outstanding questions and aims

- What is the relationship between cellular melanin distribution and extracellular matrix changes in melasma?
- Can the presence of melanophages be identified *in vivo* in melasma lesions?

- Can melasma sub-types be distinguished noninvasively with high accuracy to inform treatment?

Aims:

1) Evaluate the relationship between epidermal melanin distribution and dermal photodamage (elastosis) in melasma.

2) Identify signs of prior inflammation by evaluating the presence of melanophages in the *in vivo* images of melasma.

3) Identify and characterize the location of excess pigment (epidermal and/or dermal) in melasma lesions in order to classify the different types of melasma to guide treatment.

4.3 Method of study

4.3.1 Patients and imaging

The experiments were conducted with the full consent of each subject using a protocol approved by the Internal Review Board for clinical research in human subjects at UC Irvine. Twelve female subjects age 29-58 and Fitzpatrick skin type II-IV with facial melasma lesions were enrolled in this pilot study. Board certified dermatologists Anand K. Ganesan and Sanghoon Lee used a Woods lamp to determine melasma diagnosis. Seven subjects were diagnosed with primarily epidermal melasma and five were diagnosed with primarily dermal or mixed. Four subjects had a history of treatment for their melasma within the past year (Table 4.1).

Table 4.1. Summary of location imaged and previous treatment for each subject.

Subject	Diagnosis	Location Imaged	Previous Treatment*
1	Epidermal	Forehead	Tretinoin 0.05%, Hydroquinone 4%, Fluocinoide 0.05%
2	Epidermal	Cheek	Clobetasol 0.05%
3	Dermal/Mixed	Cheek	none
4	Epidermal	Forehead	Retin-A 0.05%, Hydroquinone 4%
5	Dermal/Mixed	Cheek	Tazorac 0.05%, Desonide 0.05%
6	Epidermal	Cheek	none
7	Dermal/Mixed	Cheek	none
8	Epidermal	Cheek	none
9	Dermal/Mixed	Cheek	Protopic 0.1%, Elidel 1%
10	Epidermal	Forehead	IPL, Tretinoin
11	Dermal/Mixed	Cheek	none
12	Epidermal	Cheek	none

*No treatment administered for at least two months prior to MPM imaging.

All melasma lesions were located on the face, mainly on cheek and forehead. Imaging sites included melasma and perilesional areas (Table 4.1). Perilesional areas were located within a few centimeters from the lesion. Multiple locations at each site were imaged *in vivo* using MPM.

Imaging of melasma patients was completed with the MPTflex MPM device, described in detail in Chapter 2.3.1. We acquired data using two excitation wavelengths, 790 nm and 880 nm. The 790 nm shows the overall morphology through emission signals from all fluorophores (NADH/FAD, keratin, melanin, elastin fibers) and collagen fibers in skin (Figure 4.1, a). The 880 nm was used in order to maximize the melanin contrast against TPEF signals from other components of the epidermis (keratin, NADH/FAD), which facilitates quantification of melanin in the epidermis (Figure 4.1,b).

We acquired optical sections of $200 \times 200\ \mu m^2$ at different depths ranging from 0 to about 150 μm (5 μm steps). Since each optical section is limited to a small scan field, to improve the overall characterization of the examined skin we acquired three stacks of images for each of the

lesional and perilesional areas and for each excitation wavelength, 790 nm and 880 nm; thus a total of twelve stacks for each subject.

4.3.2 Assessment of melanophages

The presence/absence of dermal melanophages in MPM images was determined by board-certified dermatopathologist Ronald M. Harris based on visual assessment. Dr. Harris has extensive expertise with MPM image interpretation from his involvement in previous studies on MPM clinical skin imaging[24,57,110]. Criteria for identification of melanophages included large size (>12 μm diameter)[131,132], increased fluorescence brightness compared to fluorescence from surrounding elastin fibers[133], presence of a nucleus, shape, ill-defined cytoplasmic borders, and clustering distribution within the dermis[134].

4.3.3 Assessment of epidermal melanin content

For measuring the melanin volume fraction (MVF), we used the TPEF images acquired in the lesional and perilesional epidermal areas (880 nm excitation wavelength). The MVF corresponding to each acquired stack was calculated following image processing based on an algorithm described in a previous study[62] . In short, each TPEF image was converted into a binary image using the same threshold for all images. The pixels of value "1" represented the melanin contribution and were used to calculate the area occupied by melanin in each image and subsequently, the volume occupied by melanin in each acquired stack (Figure 4.1, c). The MVF was defined as the ratio between the melanin volume and the imaged volume.

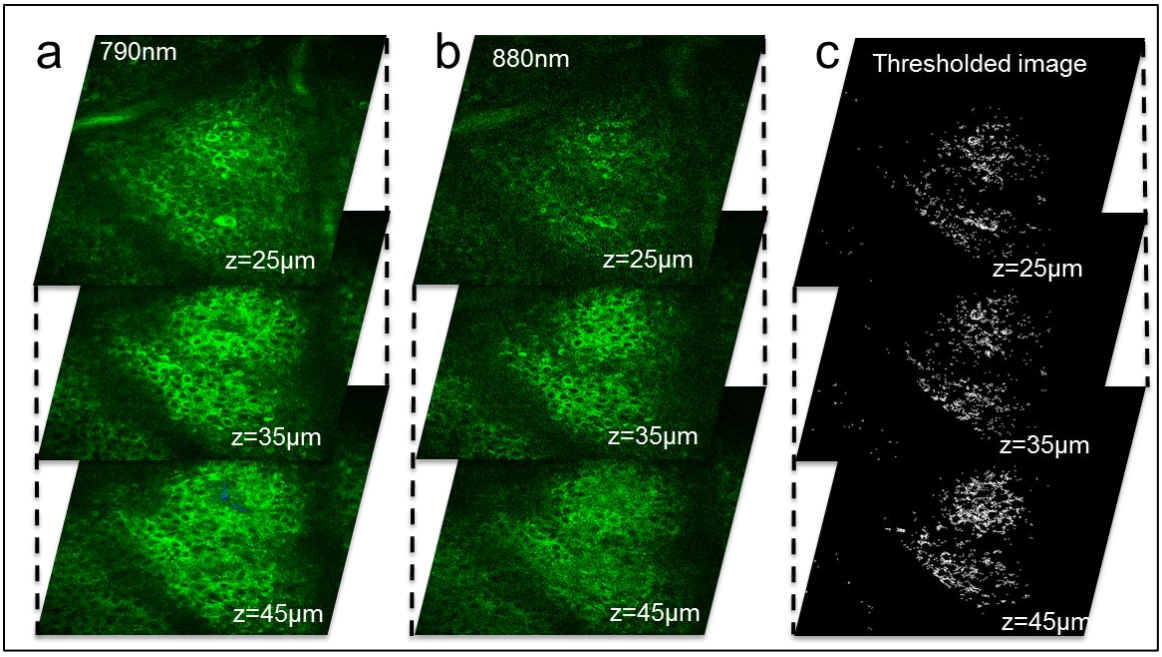

Figure 4.1. MPM image processing for estimating the melanin content. Stacks of TPEF images acquired at different depths at (a) 790 nm and (b) 880 nm. (c) thresholded images corresponding to the stack of TPEF images shown in (b).

4.3.4 Assessment of elastosis

The severity of solar elastosis (overproduction or clumping of elastin in the dermis)[135] in the lesional and perilesional areas was evaluated semi-quantitatively as "mild", "moderate" and "severe", based on visual assessment by Ronald M. Harris. We correlated this evaluation with a more rigorous quantitative assessment based on the TPEF and SHG signals from elastin and collagen fibers, respectively. For each patient, we selected about 5 frames corresponding to superficial dermis in each stack. We measured the mean intensity of the TPEF signal from elastin fibers and of the SHG signal from collagen fibers in each frame. We determined the elastosis severity in the superficial dermis by defining a metric as a/(a+b), where a and b represented the mean intensity of the TPEF and SHG signals, respectively. Based on its definition, this metric

increased with the increase of elastosis. We used a paired t-test to determine whether the metric values were significantly different in the lesion compared to the perilesion of each patient.

4.4 Results

We analyzed the MPM images acquired *in vivo* from melasma lesional and perilesional skin in 12 subjects. There were three parameters of interest in the evaluation of melasma: the presence of dermal melanophages, epidermal melanin content and distribution, and elastosis severity. We assessed these parameters in both melasma (lesion) and adjacent normal skin (perilesion) for comparison purposes. We compared the quantitative parameters measured in two groups: epidermal and dermal/mixed melasma as diagnosed by the board certified dermatologists Anand K. Ganesan and Sanghoon Lee based on Wood's lamp. The following sections expand on the findings related to measured parameters.

4.4.1 Assessment of melanophages

The dermal melanophages we imaged could be classified in 4 groups: (1) clusters of small melanophages (10-15 μm) (Figure 4.2, a), (2) clusters of large melanophages (15-20 μm) (Figure 4.2, b), (3) dendritic melanophages (Figure 4.2, c), and (4) individual (scattered) melanophages (Figure 4.2, d). Table 4.2 includes the number of melanophages identified in the volume measured for each subject.

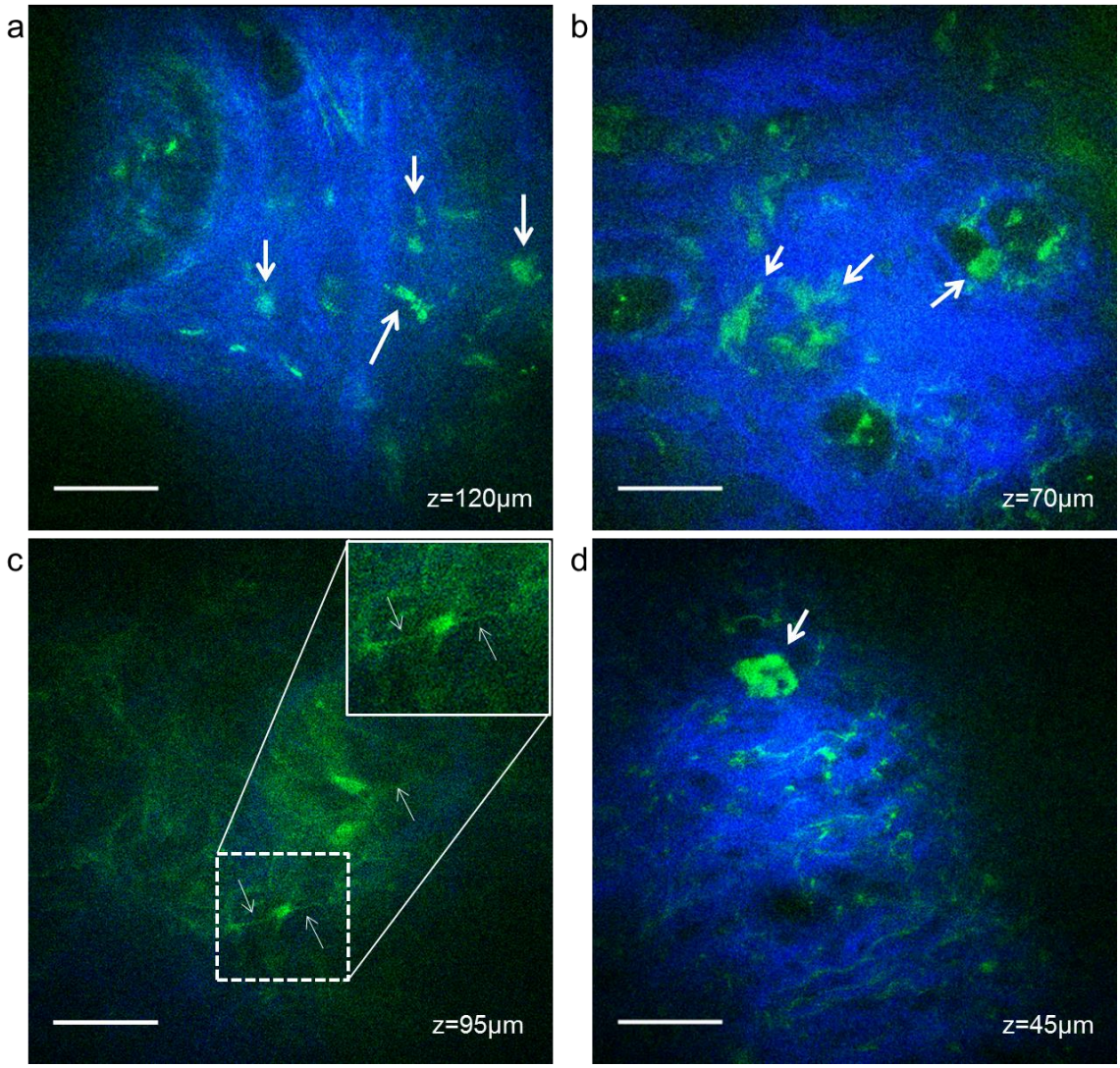

Figure 4.2. MPM imaging of dermal melanophages in melasma lesions. MPM images showing: (A) clusters of small dermal melanophages (arrows), (B) clusters of large dermal melanophages (arrows), (C) dendritic melanophages (arrows), and (D) individual/scattered dermal melanophages (arrow). Images in A, B, C are from subjects with dermal/mixed melasma. Image D corresponds to epidermal melasma. Collagen and elastin fibers are visualized in dermis by their SHG (blue) and TPEF (green) signals, respectively. 'z' represents depth in all MPM images. Scale bar is 40 µm.

Table 4.2. Number of melanophages identified in the imaged volume for each subject.

Subject	Diagnosis	Number of Melanophages in Measured Volume*		Depth of Pigment** (μm)	
		Lesion	Perilesion	Lesion	Perilesion
1	Epidermal	0	0	-	-
2	Epidermal	0	0	-	-
3	Dermal/Mixed	11	0	150	-
4	Epidermal	0	0	-	-
5	Dermal/Mixed	0	12	-	140
6	Epidermal	0	0	-	-
7	Dermal/Mixed	7	0	110	-
8	Epidermal	2	0	80	-
9	Dermal/Mixed	8	4	150	140
10	Epidermal	0	0	-	-
11	Dermal/Mixed	20	0	135	-
12	Epidermal	0	0	-	-

* Imaged volume was up to 0.6 x 0.6 x 0.15 mm^3 for all sites.

** Depth of pigment represents the deepest location melanophages were identified in the imaged volume.

We imaged occasional dermal melanophages in one of the seven subjects diagnosed with epidermal melasma and larger number of melanophages (7-20) in four of the five subjects diagnosed with dermal/mixed melasma. In two of the subjects diagnosed with dermal melasma a small number of melanophages (4-12) were identified in the perilesion.

4.4.2 Assessment of epidermal melanin content and distribution

The melanin appears in the MPM images as bright fluorescence spots in the cellular cytoplasm, representing aggregates of melanosomes. The MPM images provided information about the melanin content and distribution in melasma compared to adjacent normal skin

Subjects in the epidermal melasma diagnosis group generally showed significantly ($p=0.03$) higher pigment amount in lesional skin (14±4%) compared to perilesional skin (11±3%) in the epidermis, while subjects diagnosed with dermal/mixed melasma presented similar pigment

amount (p=0.32) in lesional skin (11±5%) compared to perilesional skin (13±6%) in the epidermis (Figure 4.3).

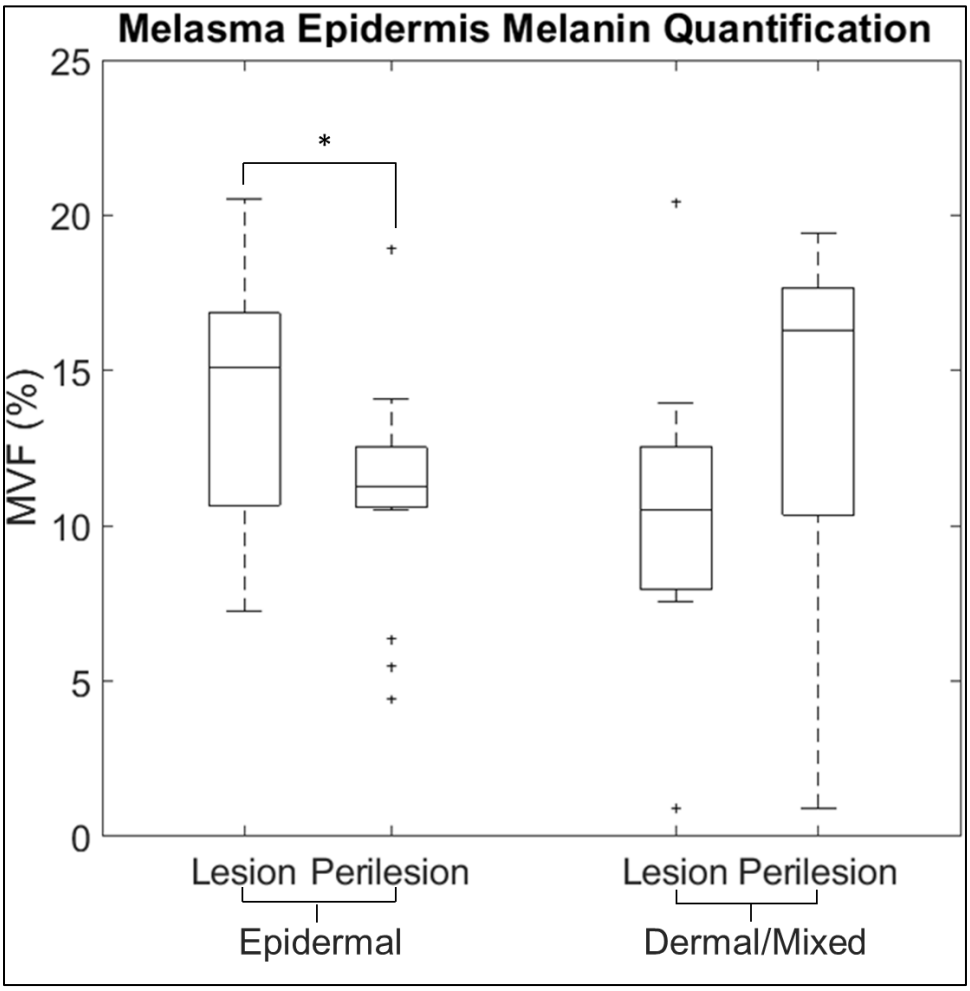

Figure 4.3. Distribution of the mean MVF values. The distribution of the mean MVF values measured in all lesions diagnosed as epidermal melasma (*p=0.03) and dermal/mixed melasma (p=0.32) and in corresponding perilesional skin.

Besides the difference in melanin amount, the lesions and perilesions also showed difference in melanin distribution. Pigment within the basal cells was distributed either towards

the cellular membrane, away from the nucleus (Figure 4.4, a) or towards the nuclear membrane as melanin caps (Figure 4.4, b). Melasma was more often characterized by the melanin distribution towards the cellular membrane compared to adjacent normal skin. In melasma lesions, melanin caps were either absent or very few compared to adjacent normal skin. The MPM images shown in Figure 4.4 a, b, and their corresponding stacks shown in Figure 4.4 c, d, correspond to the 790 nm excitation. Melanin is visualized as bright fluorescence signal at this excitation wavelength. While images acquired at 880 nm excitation wavelength were used for estimating the melanin content (see example shown in Figure 4.1), the images acquired at 790 nm allow visualization of the dermal-epidermal junction and accurate identification of the basal layer through the SHG signal from the tops of the dermal papillae (Figure 4.4 c, d). Conversely, the fixed settings for the emission filters do not allow the separation of the TPEF and SHG signals for the 880 nm excitation.

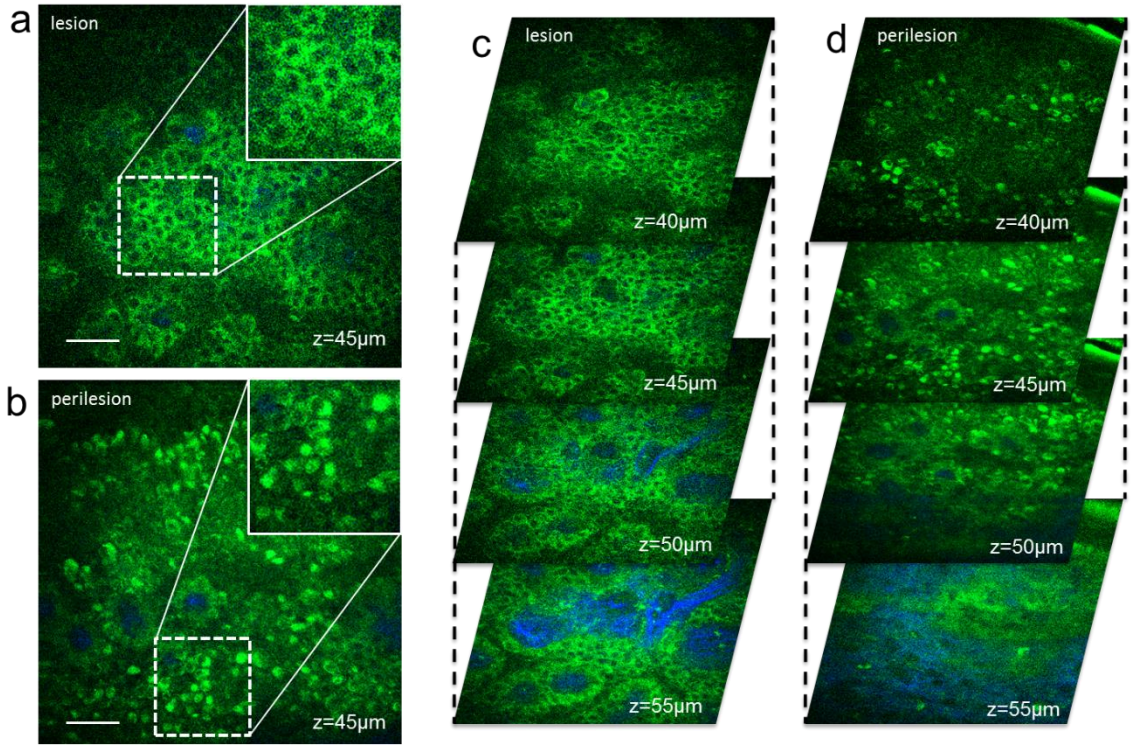

Figure 4.4. MPM imaging of epidermal melanin distribution in melasma lesion and perilesion. MPM images showing: (a) melasma lesional skin, with pigment distribution localized mainly towards the cellular membrane, and (b) perilesional skin, with pigment distribution localized mainly towards the nuclear membrane (melanin caps). The insets in (a) and (b) show a close-up of the melanin distribution in the lesion and perilesion keratinocytes. These images were selected from the corresponding stacks acquired at different depths as shown in (c) and (d). MPM images are from a subject with dermal/mixed melasma. 'z' represents depth in all MPM images. Scale bar is 40 μm.

4.4.3 Assessment of elastosis

Elastosis was visualized by MPM as an over-production of normal elastin fibers (Figure 4.5, a1, c1) or thickened, clumped elastin fibers (Figure 4.5, b1, b2). The severity of elastosis in the lesional and perilesional areas was categorized semi-quantitatively as "mild," "moderate," or "severe" by the board-certified dermatopathologist Ronald M. Harris. Generally, MPM images of lesional skin showed an increase in elastosis severity compared to perilesional skin. Occasionally, perilesional normal skin showed increased elastosis compared to the adjacent melasma lesion as

illustrated in Figure 4.5 c1-c2. The dermatopathologist evaluation of elastosis was validated by employing a quantitative analysis based on the TPEF and SHG signals from elastin and collagen fibers, respectively. The parameter we used to determine the elastosis severity in the superficial dermis was defined as a/(a+b), where a and b represented the mean intensities of the TPEF and SHG signals, respectively (see Methods). The value of this parameter ranged between 0.2 and 0.7 for both lesion and perilesion. Based on its definition, the parameter increased with the severity of elastosis. Thus, eight out of twelve subjects showed a significant increase in elastosis severity in their melasma area compared to perilesional skin ($p<0.05$), three subjects showed a significant increase in elastosis severity in their perilesional normal skin compared to melasma ($p<0.05$), while one other subject showed a similar degree of elastosis severity in both lesion and perilesion (Figure 4.6).

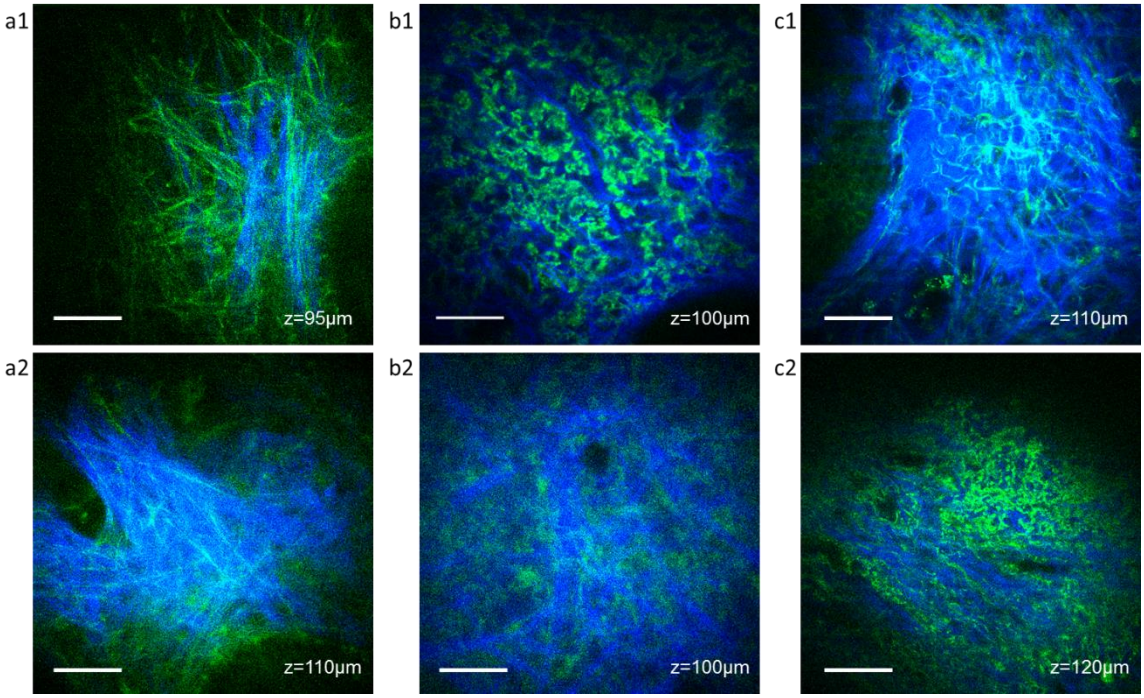

Figure 4.5. MPM imaging of elastosis in melasma lesion and perilesional skin. MPM images of the dermis in the lesion (A1, B1, C1) showing severe elastosis with overproduction of normal elastin fibers (A1, C1), and abnormal elastin fibers (B1); MPM images of the dermis in the corresponding perilesion (A2, B2, C2) showing: moderate elastosis (A2), mild elastosis (B2), and moderate elastosis with overproduction of abnormal elastosis fibers (C2). Collagen and elastin fibers are visualized in dermis by their SHG (blue) and TPEF (green) signals, respectively. 'z' represents depth in all MPM images. Scale bar is 40 μm.

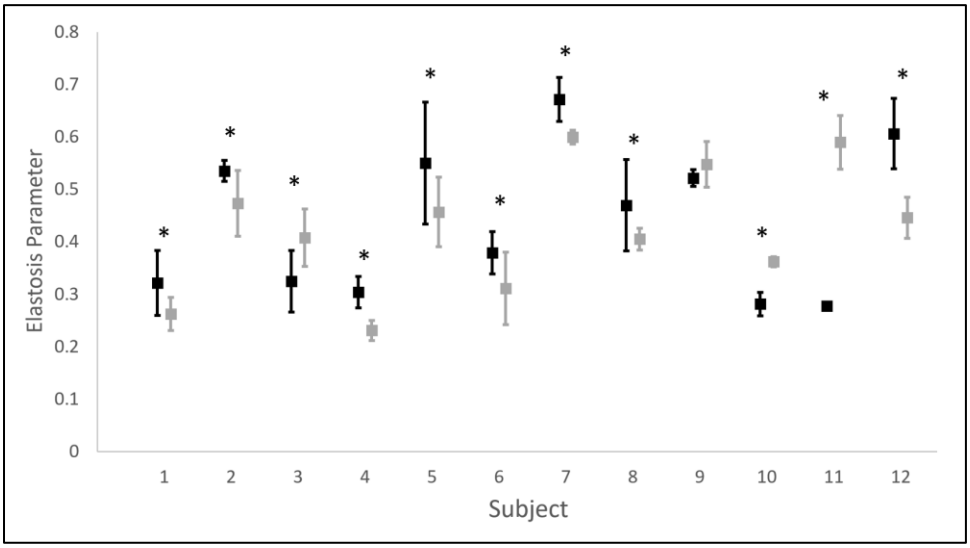

Figure 4.6. Plot of the mean elastosis parameter values. The mean of the elastosis parameter for each subject measured in lesional (black) and corresponding perilesional (gray) skin. Error bars represent the standard deviation over all images at each site for each subject (*$p<0.05$).

Analysis of the lesional and perilesional dermal appearance and the corresponding epidermal melanin distribution revealed an interesting observation: 70% of lesions and perilesions showed increased elastosis and presence of melanophages associated with lack of melanin caps in the basal layer of the epidermis. This observation is illustrated by representative images in Figures 4.7 and 4.8 and Table 4.3.

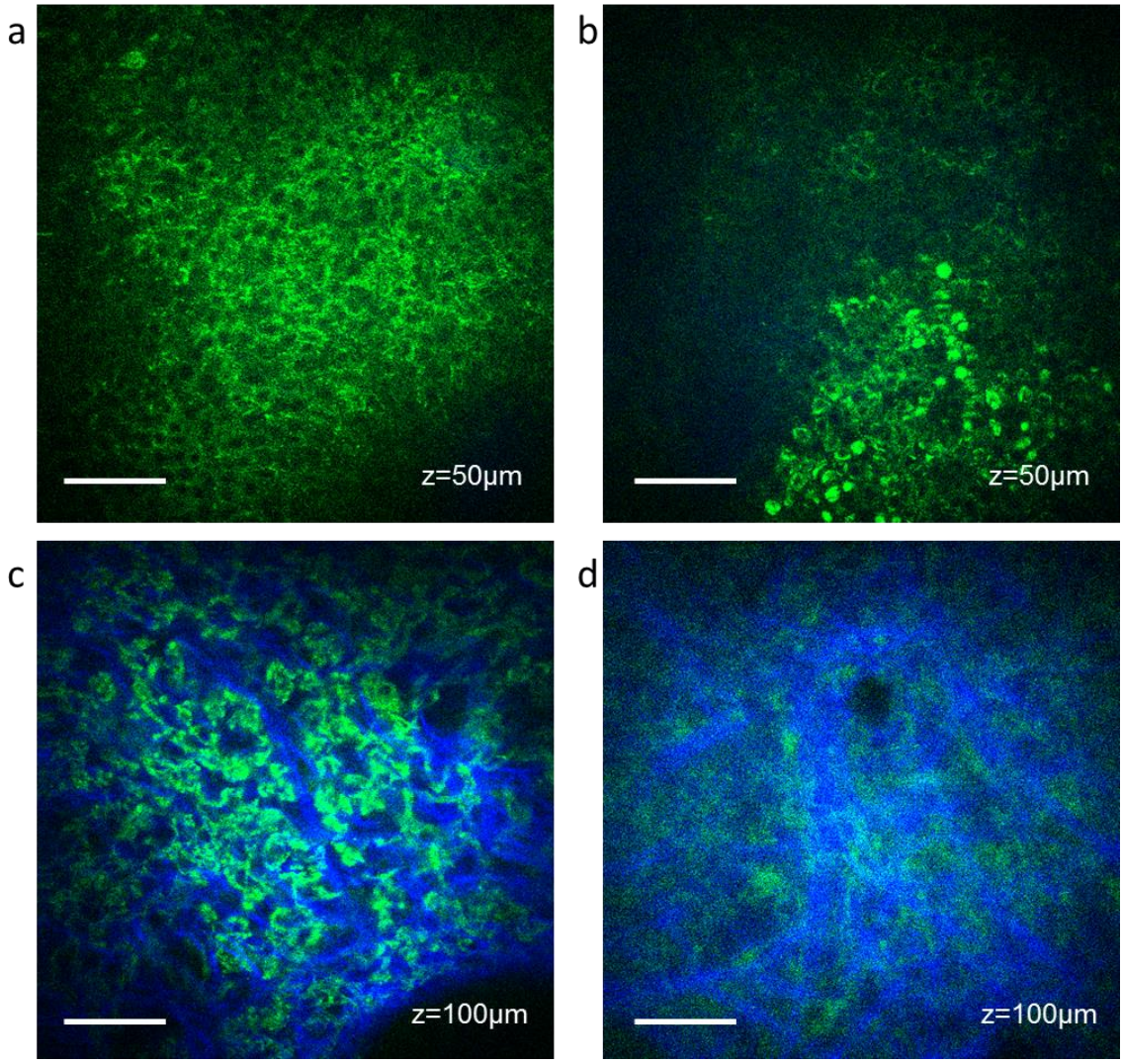

Figure 4.7. Representative MPM images of epidermal pigment distribution in the basal layer vs. elastosis severity in melasma lesion and perilesional skin. MPM image of the epidermis in the lesion (A) showing an epidermal pigment distribution localized towards the cellular membrane, and perilesion (B) showing an epidermal pigment distribution localized towards the nuclear membrane (melanin caps); MPM images of the dermis in the lesion (C) showing severe elastosis with overproduction of abnormal elastosis fibers, and perilesion (D) showing mild elastosis. Collagen and elastin fibers are visualized in dermis by their SHG (blue) and TPEF (green) signals, respectively. 'z' represents depth in all MPM images. Scale bar is 40 μm.

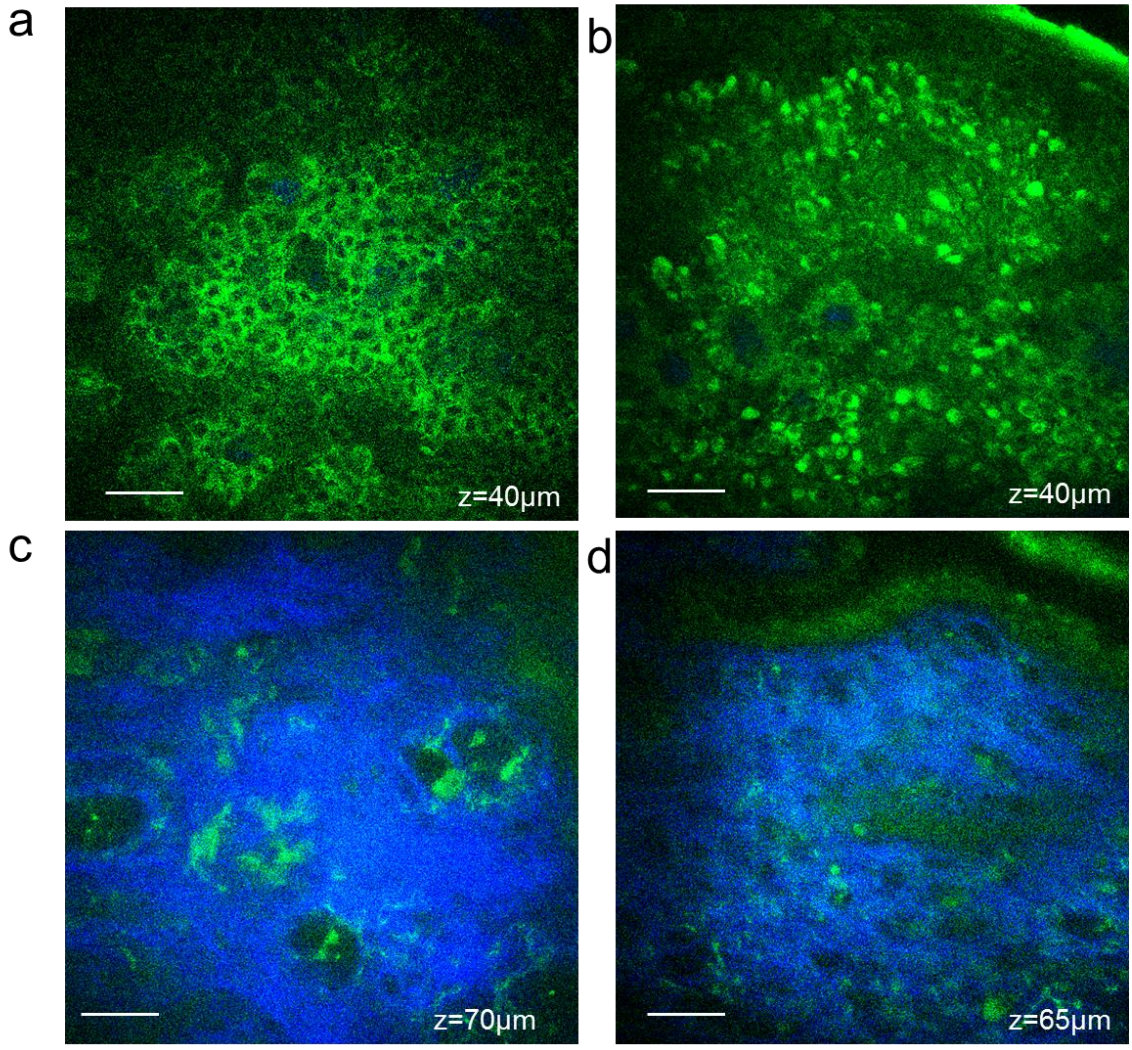

Figure 4.8. Representative MPM images of epidermal pigment distribution in the basal layer vs. presence of dermal melanophages in melasma lesion and perilesional skin. MPM image of the epidermis in the lesion (A), showing an epidermal pigment distribution localized towards the cellular membrane, and perilesion (B), showing an epidermal pigment distribution localized towards the nuclear membrane (melanin caps); MPM images of the dermis in the lesion (C), showing clusters of dermal melanophages, and perilesion (D), showing no dermal melanophages. Collagen and elastin fibers are visualized in dermis by their SHG (blue) and TPEF (green) signals, respectively. 'z' represents depth in all MPM images. Scale bar is 40 µm.

Table 4.3. Summary of melanin caps presence in basal cells and elastosis severity as evaluated by Dr. Ronald M. Harris for each subject.

		Presence of Melanin Caps		Elastosis Severity	
Subject	**Diagnosis**	**Lesion**	**Perilesion**	**Lesion**	**Perilesion**
1	Epidermal	no caps	✔✔	✔✔✔	✔
2	Epidermal	✔	-	✔✔✔	✔
3	Dermal/Mixed	no caps	✔	✔✔✔	✔✔
4	Epidermal	✔	✔✔	✔	✔✔
5	Dermal/Mixed	no caps	✔	✔✔✔	✔✔
6	Epidermal	✔	✔	✔✔✔	✔
7	Dermal/Mixed	no caps	-	✔✔	✔
8*	Epidermal	✔	✔	✔✔	✔✔
9	Dermal/Mixed	no caps	no caps	✔✔	✔
10*	Epidermal	✔	✔	✔	✔
11	Dermal/Mixed	no caps	✔✔	✔✔	✔
12	Epidermal	no caps	✔	✔✔✔	✔✔

*Not included in total number since elastosis severity was similar in lesion and perilesion.
Check marks represent level of elastosis severity or density of melanin caps (✔ - lowest, ✔✔✔ highest). The highlighted data emphasize lesions that showed increased elastosis associated with lack of melanin caps in the basal layer of the epidermis.

4.5 Discussion

This study evaluated the potential of MPM to be used as a non-invasive imaging tool for visualizing melasma features, particularly melanophages, as a sign of prior inflammation, and for advancing our understanding of morphological changes related to this skin condition.

The most relevant feature we sought to capture by MPM imaging was the sign of a prior inflammatory response in the form of melanophages. Identification of melanophages in the dermis represents an indication of dermal pigment presence, a key element for differential diagnosis of melasma and successful treatment. MPM identified presence of melanophages in four out of five dermal/mixed melasma lesions and in one out of seven epidermal melasma lesions. Melanophages were also visualized in normal perilesional area of one patient diagnosed with dermal/mixed melasma. Presence of dermal melanophages in the epidermal melasma lesion indicates a potential

erroneous clinical diagnosis of the lesion. The absence of melanophages in one dermal/mixed melasma is related to either an erroneous diagnosis of the lesion or very likely to the sampling limitation of MPM. Melanophages in dermal/mixed melasma lesions have been previously identified non-invasively by RCM imaging and confirmed by histopathology[125]. Presence of melanophages in perilesional skin of melasma has been reported in studies based on histopathology results[19,136].

Enhanced melanin content of the epidermis was another MPM key feature of melasma. We defined a melanin volume fraction (MVF) index corresponding to the imaged volume in each patient. We found that only epidermal melasma lesions were characterized by significantly higher MVF values compared to normal skin, while in dermal/mixed melasma patients these values were rather comparable for lesion and perilesion. We believe this might be the result of melanin migration across the basal layer into the dermis as suggested in a previous study[137], which leads to presence of dermal melanophages in these lesions. Studies have commonly found enhanced melanin content in melasma lesions compared to perilesional normal skin[125,136]. However, the results were based on visual assessment and did not include a separate analysis of melanin content in epidermal and dermal/mixed melasma groups. An additional observation was related to the melanin distribution pattern within keratinocytes in melasma skin as compared to normal skin. In the basal layer of normal skin, melanocytes transfer melanosomes to keratinocytes, which then align these melanosomes to form caps above their nuclei, protecting them from UV induced DNA damage. In melasma lesions, however, melanosomes in the basal cells were more often not distributed above the nuclei but appeared to be more randomly dispersed throughout the keratinocyte. These findings are consistent with the results of a previous study based on biopsy and H&E staining showing that basal keratinocytes display

changes in nuclei sizes and chromatin texture in melasma lesions compared to perilesional skin[138].

We have also investigated the change in fibrillar structure in melasma lesions compared to adjacent normal skin. Both melasma lesions and perilesions were generally affected by elastosis, in agreement with previous reports[139,140]. Elastosis was evaluated by a dermatopathologist through visual assessment and was well correlated with a quantitative index we defined as a metric for elastosis. This metric showed an enhanced amount of elastosis in melasma compared to perilesion for most patients, regardless of the type of melasma, in accordance with previous studies based on histopathology[139,140]. While both melasma and elastosis are dependent upon UV exposure, it is unclear whether elastosis is caused by melasma (i.e. the increase in pigment content and its distribution favor the appearance of elastosis) or whether melasma and solar elastosis are independent of each other.

The changes observed in the melanin distribution of basal keratinocytes and absence of melanin caps in the basal layer of the epidermis likely provide reduced photoprotection as they seemed to be associated with more pronounced dermal photodamage. Thus, 70% of lesions and perilesions showed increased elastosis associated with lack of melanin caps in the basal layer of the epidermis. Further studies are needed in order to determine whether altered distribution of melanosomes plays a role in the pathogenesis of melasma.

Although these results are limited by a modest sample size, they demonstrate the potential of MPM to characterize melasma. Most notably, MPM demonstrated the ability to visualize non-invasively the signs of a prior inflammatory response, a key element in the differential diagnosis of melasma. Additionally, the technique was able to quantify the melanin amount and its distribution in the epidermal basal layer as well as dermal elastosis in melasma. The results suggest

potential correlations among the melanin amount and distribution in the basal keratinocytes, dermal inflammation and photodamage. A more comprehensive study of a larger number of subjects is necessary to evaluate the ability of MPM to improve the differential diagnosis of melasma and to advance the understanding of this skin condition.

An expanded study would need to address current technical limitations related to MPM imaging, particularly the reduced FOV and penetration depth. High penetration depth allows for a better evaluation of the melanophage population in the dermis. Penetration depth can be optimized by implementing dispersion compensation to decrease the laser pulse duration[110,111]. Although the benefit would still be limited, the ability of MPM to visualize melanophages in melasma lesions as described in this study holds great promise. Sampling a large FOV is key for accurate diagnosis of melasma type since lesions are often non-uniform with certain features focally localized. This limitation has been recently addressed by our group and is discussed in more detail in Chapter 5. These results show that MPM can be valuable in learning more about melasma biology, and confirming a melasma clinical diagnosis or providing a more accurate picture of where the pigment is actually located so the correct method of treatment can be used.

4.6 Main findings and significance

- Basal keratinocytes in melasma have a pigment distribution localized towards the cellular membrane and generally lack the melanin caps providing reduced photoprotection as they appear to be associated with more pronounced dermal photodamage (elastosis) compared to perilesional skin. This finding motivates future studies to determine whether altered distribution of melanin plays a role in the pathogenesis of melasma.

- Signs of prior inflammatory response in melasma in the form of melanophages in the dermis can be captured by *in vivo* MPM, an uncertainty before the study due to the MPM limited penetration depth.
- Epidermal melasma is characterized by significantly higher amounts of epidermal melanin compared to perilesional skin, while dermal/mixed melasma presents a similar pigment amount in both melasma and perilesional skin, a result that has been speculated about based on visual assessment.

5. Multiphoton microscopy instrument development for enhanced skin characterization

5.1 Background

As demonstrated in the studies described in the previous chapters, multiphoton microscopy technology represents a valuable imaging tool for non-invasive clinical skin imaging to advance the understanding of skin biology and skin disease. Compared to existing clinical skin imaging approaches, MPM imaging provides label-free molecular contrast and sub-micron spatial resolution. However, based on the performed clinical studies, some of them described in this dissertation, we have identified several technological barriers that limit the applicability of MPM for human skin characterization. These technical challenges are related to limited scanning area, slow frame rate, high cost, and complexity. In order to address these technical limitations, our group has recently developed a fast large area multiphoton exoscope (FLAME)[141], a compact, portable device based on an earlier design of a laboratory benchtop prototype[65]. FLAME includes a fast resonant scanner, customized relay and beam expander optical systems, and a high NA, low magnification objective lens. This prototype maximizes the field-of-view (FOV) to nearly 1 mm^2 and reduces the imaging time per unit area to 2 sec/mm^2 while maintaining sub-micron resolution, resulting in over an order of magnitude improvement in FOV and imaging speed compared to the MPTflex. FLAME also features time-resolved detection to allow detection of fluorescence photons based on their arrival time. There are several outstanding questions related to the development of this imaging platform as summarized below.

5.2 Outstanding questions and aims

- Can the molecular contrast of MPM be further improved to enhance label-free specificity?
- Does macroscopic imaging improve the accuracy of an epidermal melanin assessment?
- Can macroscopic images of skin be acquired *in vivo* with microscopic resolution and high stability?

Aims:

1) Assess the ability of the FLAME imaging platform to selectively detect melanin in human skin.

2) Evaluate the impact of macroscopic imaging on a melanin assessment by measuring the melanin volume fraction in different skin types *in vivo* and compare to the skin color as characterized by a colorimeter.

3) Engineer a stable patient interface for reliable *in vivo* imaging and test its performance.

5.3 Method of study

An overview of the FLAME system is presented in Figure 5.1 and is further described in Fast et al.[141]

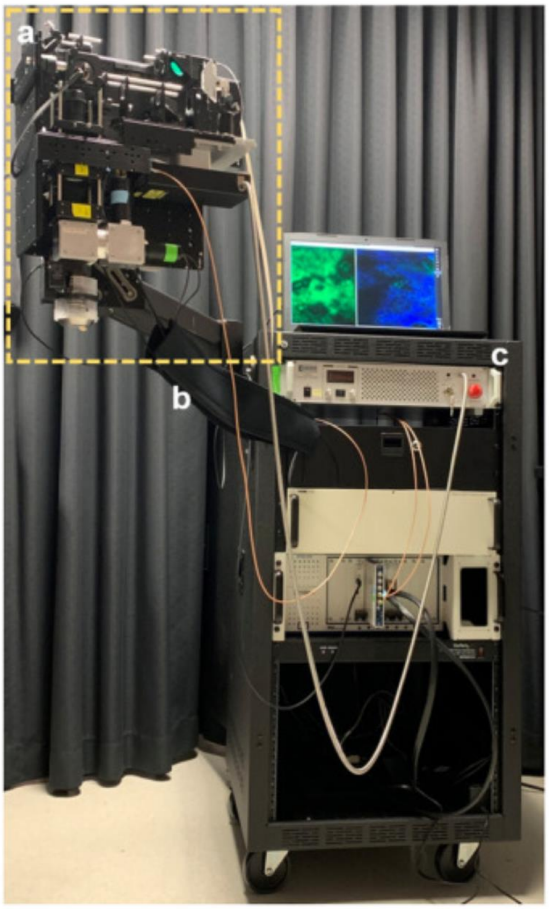

Figure 5.1. FLAME imaging platform. The scan head (a) is supported by an articulated mechanical arm (b) attached to the cart (c) that houses the electronic controllers and holds the computer.

5.3.1 Excised tissue collection and in vivo imaging

Skin specimens for *ex vivo* melanin staining were obtained from surgeries in the UCI Dermatology Clinic and consisted of remaining tissue from wound closure procedures ("dog ears"). The tissue collection procedure was exempt from the Institutional Review Board (IRB) approval since the specimens were de-identified, but they were handled based on an Institutional Biosafety Committee (IBC) approved protocol. The specimens were imaged fresh, immediately

upon collection and then subjected to Fontanna-Masson staining to compare the FLAME images to the gold standard melanin stain.

The *in vivo* imaging was conducted according to an approved IRB protocol of the University of California – Irvine with written informed consent obtained from six volunteers with Fitzpatrick skin types II-V. The two imaging sites included a non-sun exposed area (volar forearm), and sun exposed area (dorsal forearm) on each volunteer. To obtain a representative view of the skin at each site, 2-4 stacks of $943 \times 943 \times 150$ μm^3 (1024×1024 pixels) were taken using a 5 μm step size at slightly different locations within each site.

5.3.2 Enhancing the molecular contrast for selective melanin detection

Conventional fluorescence lifetime imaging microscopy (FLIM) is performed by time-correlated single photon counting (TCSPC) detection that enables acquisition of fluorescence lifetime decays with high temporal resolution but requires long integration times. To decrease imaging times, a critical factor in adoption of the technology, we use a different approach, where the analog output of the PMT is digitized at a fast rate. Specialized software (ScanImage, Vidrio Technologies) and hardware (National Instruments fast digitizer 5771) enables time-resolved single photon counting (SPC) detection with a ~390 ps (32 bins) temporal resolution. The time resolution is relatively coarse as it depends on the PMT rise time and the digitization rate, but since it is not limited by the dead time associated with photon counting, this is a fast method to rapidly separate some fluorophores based on their short and long fluorescence lifetime. The fluorescence of melanin is characterized by short lifetime with respect to most other endogenous fluorophores in skin[101,142,143]. To separate melanin from the other fluorophores, the signal is detected based on

the fluorescence photons arrival time relative to the excitation photons, in time bins of width: -0.4 – 0.77 ns (red channel) and 0.77 – 12 ns (green channel).

For image analysis, we subtract the photon counts representing the long lifetime fluorescence signal (green channel image) from the short lifetime fluorescence signal (red channel image). The subtraction process yields both positive and negative values. The negative values are due to larger contribution to signal from photons with long fluorescence lifetime. These values are set to zero in the final image resulted from subtraction. The positive photon count values resulted from subtraction are due to larger contribution to signal from photons with short fluorescence lifetime. These values represent mainly the melanin fluorescence signal contribution and the remaining signal in the final image (corrected-red channel) resulted from subtraction. We perform the time-resolved SPC volumetric imaging using three channels for simultaneous detection of the SHG signal and of the short and long lifetime TPEF signals described above.

To calculate a melanin volume fraction (MVF) for each imaged volume within the epidermis, all pixels in the volume with a positive value in the corrected-red channel were set to 1 and then summed and divided by the total number of pixels in the volume. A colorimeter was used to provide a more quantitative measurement of skin lightness compared to the class-based Fitzpatrick scale. The colorimeter value used in this study was the L* value obtained in CIE L*a*b* color space from the Chroma Meter CR-400 (Konica Minolta Sensing, Inc., Tokyo, Japan). The L* parameter is used to represent skin “lightness” on a 0-100 scale (0=darkest, 100=lightest)[144,145]. Colorimeter measurements were taken from within the same few cm as the MPM images and were then correlated with the MVF values to assess the sensitivity of the selective melanin detection.

5.3.3 In vivo multi-scale, high resolution imaging

We perform imaging on a millimeter scale by employing the following two scanning mechanisms for stitching adjacent fields of views and for acquiring volumetric images: (1) The tile mosaic scheme employs the galvo-resonant mirrors to scan each frame ('tile') and then linear stages to translate the sample in the x and y directions in order to scan adjacent tiles. Reliable *in vivo* tile mosaic scanning requires an interface that connects the stages in the device to the skin in a stable manner. (2) The volumetric imaging involves acquiring z-stacks of en face images by moving the objective in the z direction, thus scanning at different depths in the skin.

The scanning for each tile is performed in two different ways. In iteration one, miniature linear x-y stages (Q522.130, Physik Instrumente, GmbH) controlled by a customized data acquisition software (Vidrio Technologies), facilitate automatic and rapid stitching of adjacent scanned areas. We selected this stage based on its performance and reduced size ($3 \times 2.1 \times 1$ cm^3), the latter being an essential requirement for its eventual integration into the compact scanning head. This stage can be used as the mechanical scanner component while imaging either *ex vivo* or *in vivo* by taking advantage of the skin elasticity. In the second iteration of the tile scanning process, the x-y scanning is performed by a cage-mounted manual linear translator (CXY Translation Mount, ThorLabs, New Jersey, USA).

5.4 Results

Key advances of the FLAME imaging platform with respect to the bench-top prototype previously reported by our group[65] include an enhancement of the molecular contrast through

specific detection of melanin, and an increase in the scanning speed over millimeter-scale tissue areas both *in vivo* and *ex vivo*,.

5.4.1 Enhancing molecular image contrast by time-resolved single photon counting (SPC)

Based on the assignment of the time bin integration in the fluorescence detection channel in our exoscope, as described in section 5.3.2, melanin is predominantly detected in the corrected red channel, while fluorescence signals from other fluorophores such as keratin, NAD(P)H/FAD and elastin, are mainly detected in the green channel. Figure 5.2 presents a side-by-side comparison between MPM and histology images of human skin that demonstrate the co-localization of the fluorescence signal in the corrected red channel and the melanin specific stain (Fontana-Masson).

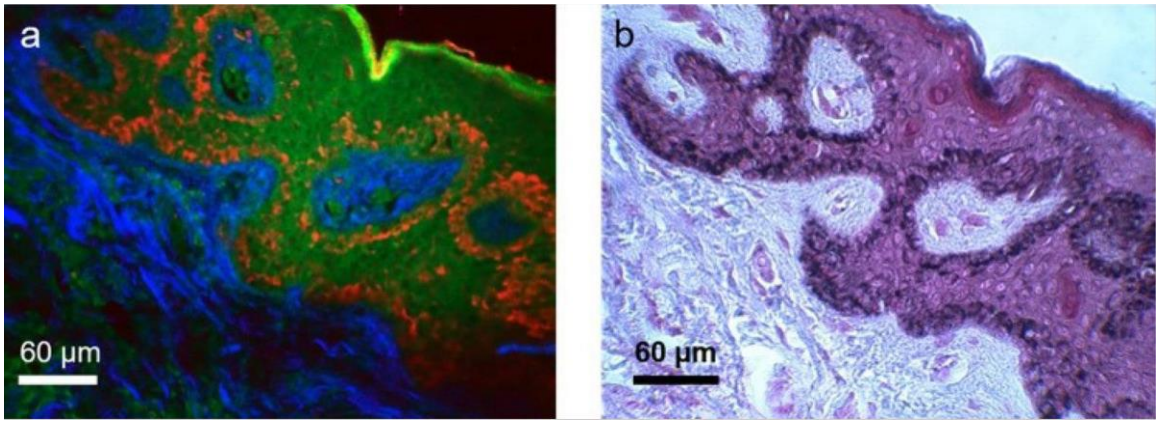

Figure 5.2. Side-by-side comparison of MPM and histological images. (a) time-resolved SPC MPM image of an unstained thin section of formalin-fixed normal human skin acquired with the FLAME system; (b) Histological image obtained by Fontana-Masson staining of a human skin section from the same sample and adjacent to the one shown in (a). The images show that the fluorescence signal in the corrected-red channel of the MPM image (a) is co-localized with the Fontana-Masson melanin-specific stain (black) in the histological image (b).

5.4.2 In vivo melanin quantification in different skin types with different assessment volumes

In order to test the ability of FLAME to quantify skin color based on melanin content in the epidermis of human skin *in vivo*, we compared the calculated melanin volume fraction with a colorimeter reading from each site in the six volunteers. In Figure 5.3, MVF values at each site are plotted against the results from colorimeter measurements (L*) at the same location as FLAME imaging.

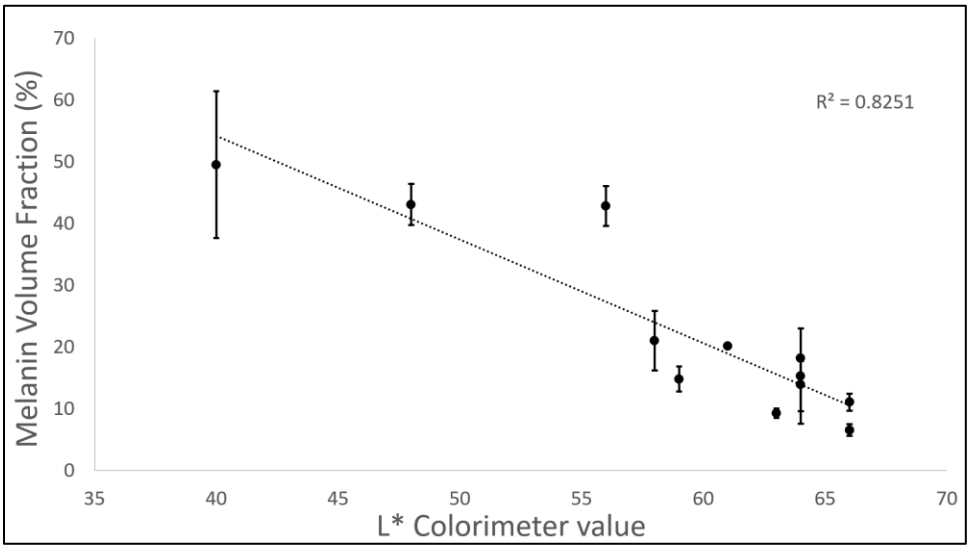

Figure 5.3. Correlation of MPM based MVF values and colorimeter measurements. MPM images and colorimeter measurements taken within 5 cm of each other for each volunteer (n=6) at both sites. Error bars are the standard deviations calculated across the 2-4 image volumes at each site for each volunteer. R^2 value is based on a linear regression of the values.

5.4.3 Rapid millimeter-scale in vivo MPM imaging of human skin at sub-micron resolution

The ultimate goal in our effort to develop the FLAME imaging platform is to utilize it as an effective imaging tool for *in vivo* skin imaging in research and clinical applications that require

high spatial resolution and molecular contrast. To this end, representative MPM images with time-resolved SPC contrast acquired *in vivo* at different depths in a volunteer's forearm are presented in Figure 5.4. The time required for acquiring 30 1 MPx frames within the z-stack was 80 s.

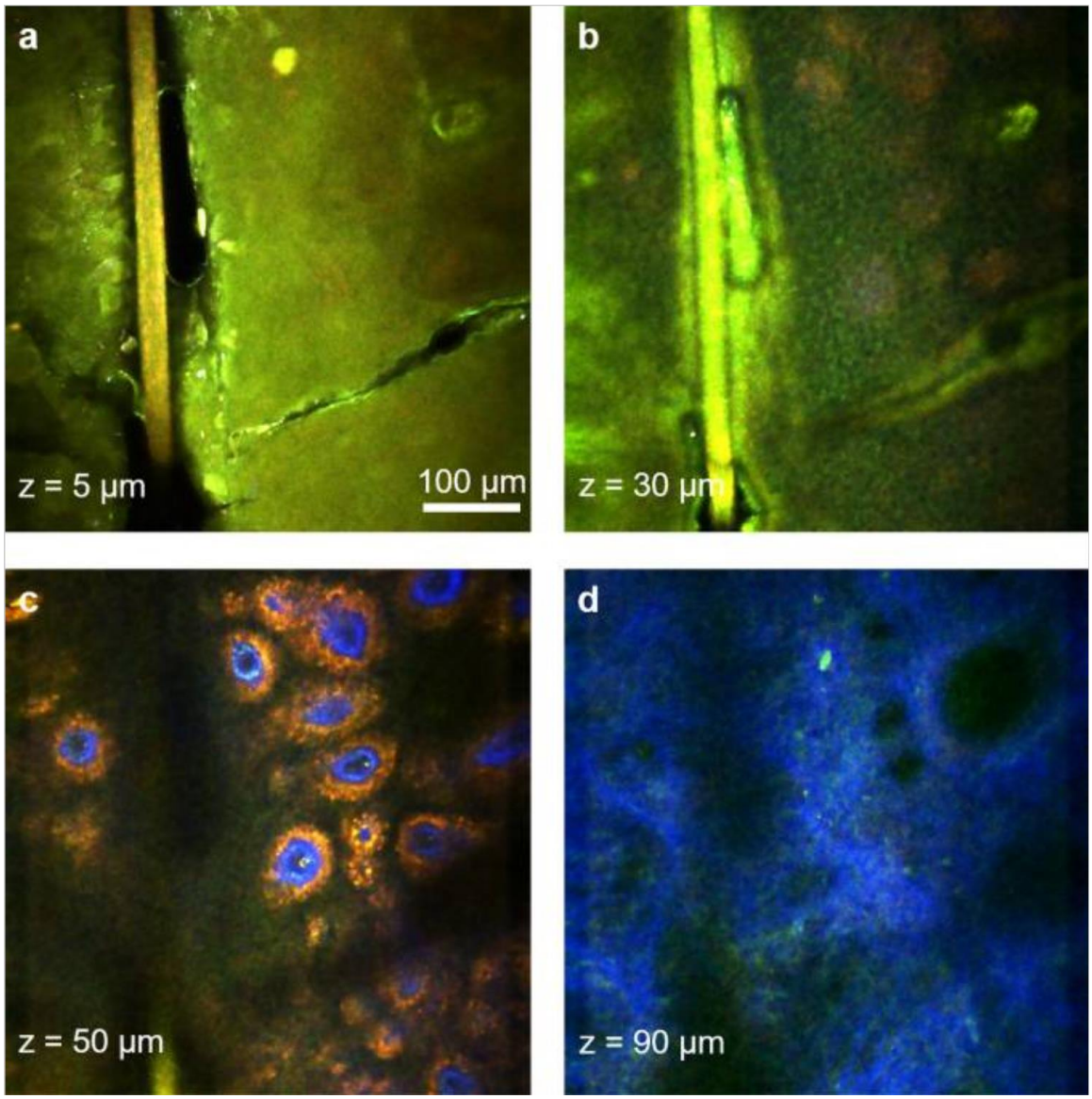

Figure 5.4. Rapid, sub-micron resolution, time-resolved SPC *in vivo* MPM imaging of human skin forearm. MPM images acquired at different depths in human skin showing the keratinized stratum corneum (a), epidermal keratinocytes (b), pigmented cells surrounding dermal papilla (red) (c) as well as collagen (blue) and elastin fibers (green) in (d).

Reliable *in vivo* tile mosaics require an interface that connects the x-y scanning stages to the skin in a stable manner. The connection must be solid as to prevent motion artifacts during imaging, but readily detachable once imaging is complete. Requirements for the connection include the design of an adapter that will connect a glass imaging window that is taped to the patient's skin to x-y scanning stages. Because the glass window is fixed to the skin with a light adhesive and the skin is highly elastic, movement of the window by the stages will result in a lateral displacement of the superficial tissue layers. This constitutes a safe and simple way for lateral scanning without physically displacing the imaging head itself.

In the first iteration of this connection, a SolidWorks designed and 3-D printed patient interface is connected to a servo-controlled miniature translation stage (Figure 5.5). In this iteration, the servo-controlled stage is attached to the benchtop and has an extendable range of 13 mm along both lateral coordinates. Using this first iteration, Figure 5.6 presents a representative millimeter-scale tile-mosaic image (2.7×2.7 mm^2) acquired *in vivo* from a volunteer's forearm in 45 s, using time-resolved SPC detection. Reliable *in vivo* images using this patient-interface required the volunteer's arm to be rested on the benchtop near the stationary benchtop-mounted x-y scanning stages, limiting the use of this iteration for bedside imaging.

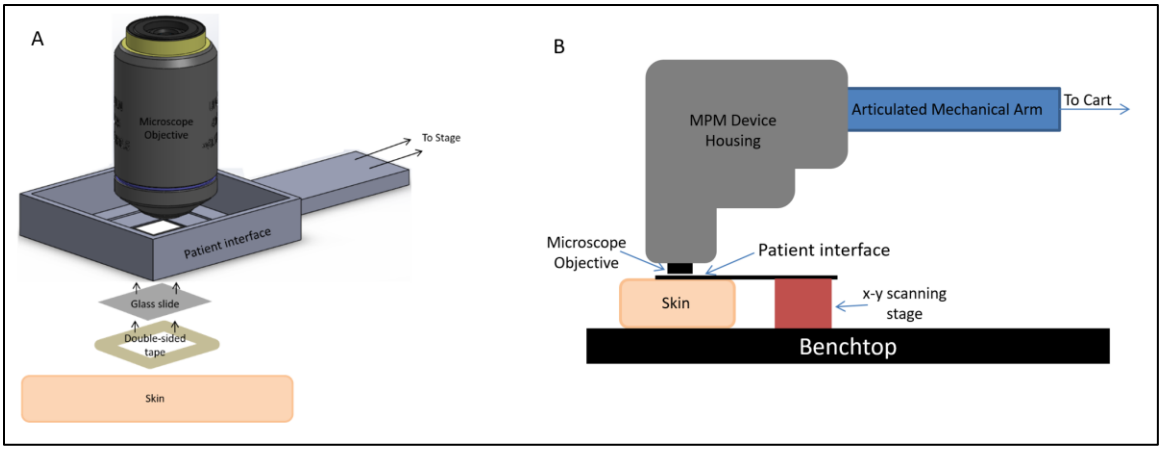

Figure 5.5. First iteration prototype patient-interface. (a) Solid Works drawing of the interface and schematic showing the attachment to the skin with double-sided tape and glass slide. (b) Schematic showing how the first iteration interface is used with the microscope.

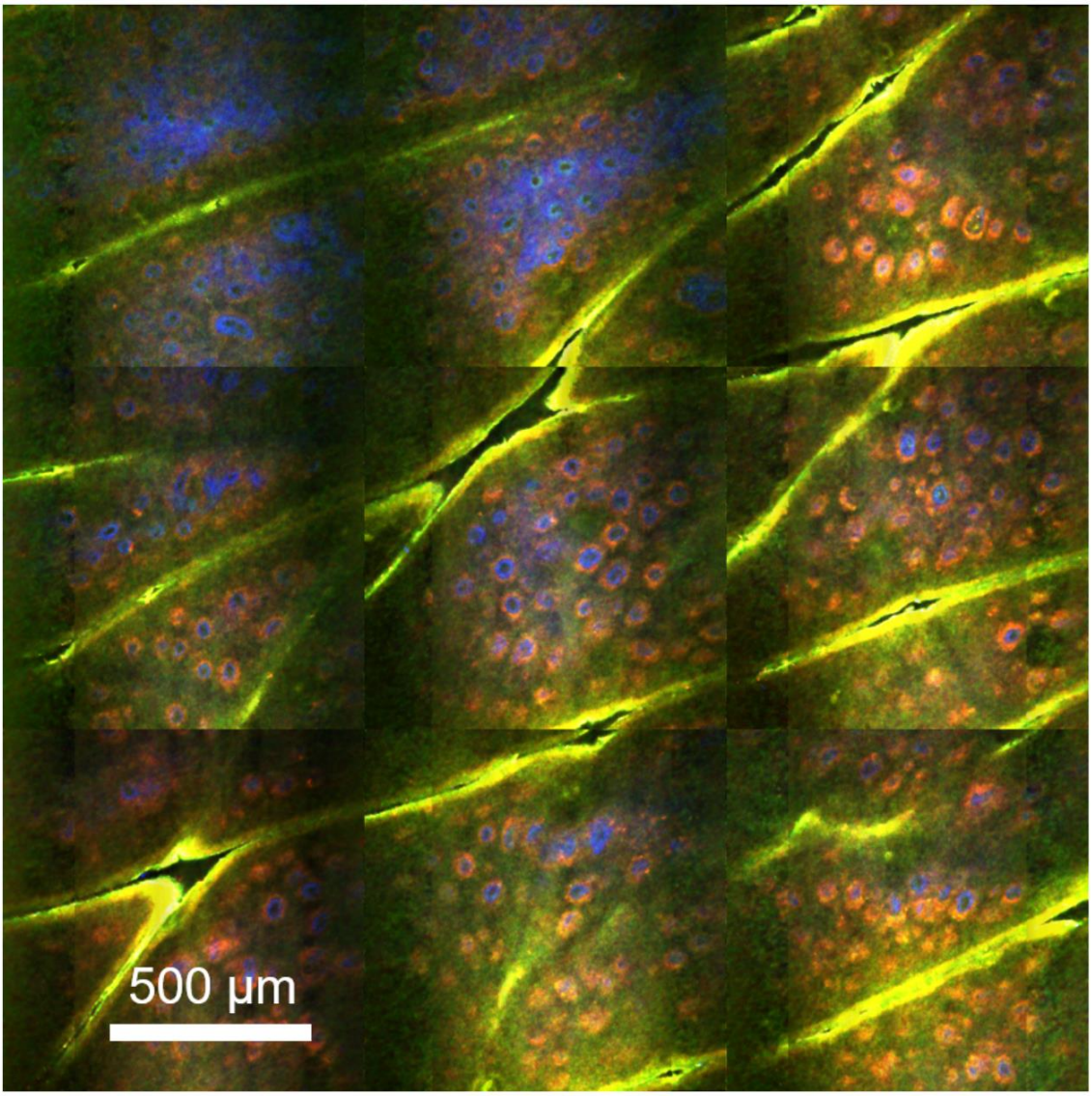

Figure 5.6. Rapid, millimeter scale, sub-micron resolution, time-resolved SPC *in vivo* MPM imaging of human skin forearm. Tile mosaic image (2.7 x 2.7 mm^2, 9 MPx) acquired in 45 seconds, at 45 µm below the surface at the DEJ. The image shows an overview of normal skin morphology at this depth mainly consisting of pigmented keratinocytes (red) surrounding dermal papilla (blue).

In the second iteration of the patient-interface, a manual x-y translation stage mount is attached to a cage mount within the imaging head and has an extendable range of 4 mm along both lateral coordinates (Figure 5.7). This iteration included the SolidWorks design of an objective enclosure for enhanced stability, and the connection of this enclosure to the manual-controlled stage scanning mechanism. Successful design and implementation allowed for reliable *in vivo* images to be acquired after bringing the MPM device to the volunteer laying on a gurney or sitting in a chair, rather than bringing the volunteer to the benchtop, as in iteration one. This makes a wider variety of imaging positions and locations possible. The interface has the ability to capture millimeter-scale MPM images *in vivo* and representative images acquired from a volunteer's forearm and face are presented in Figure 5.8 and Figure 5.9, respectively.

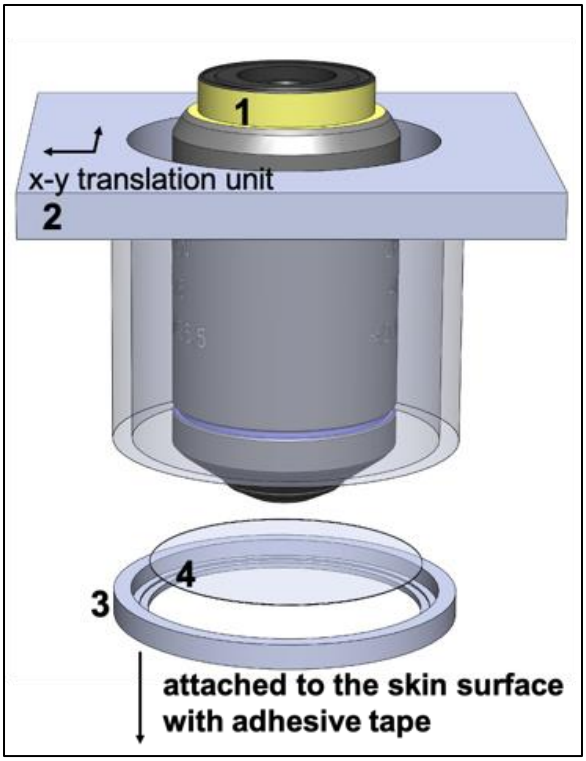

Figure 5.7. Second iteration patient-interface schematic. Solid Works schematic of the objective (1) within the manual x-y translation unit (2) that is mounted to a cage system around the objective. The attachment to the skin with double-sided tape and glass slide is indicated by 3 and 4.

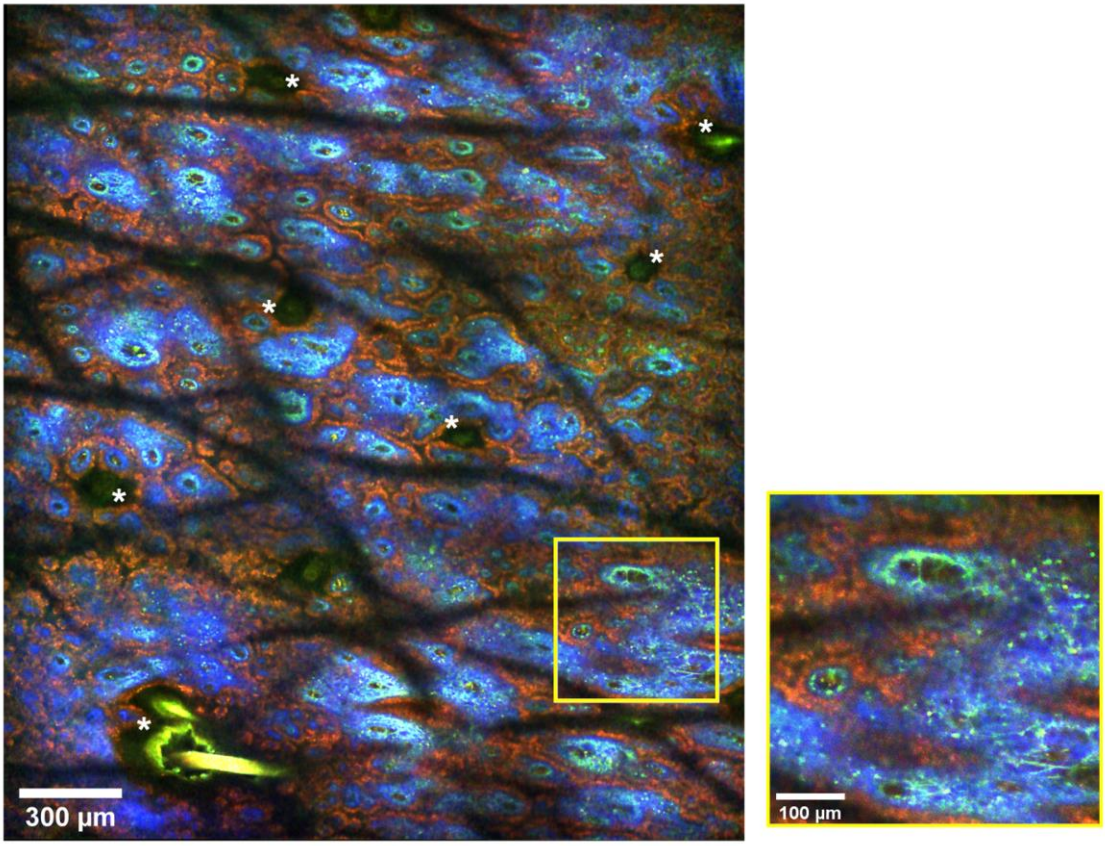

Figure 5.8. Millimeter scale, sub-micron resolution, time-resolved SPC *in vivo* MPM imaging of human forearm skin. MPM image acquired at the dermo-epidermal junction (60 µm depth) in the forearm of a volunteer. The macroscopic (left) and the close-up (right) images show collagen (SHG, blue) and elastin (TPEF, green) fibers, pigmented keratinocytes (TPEF, red) and hairs (TPEF,*). The 10 Mpx macroscopic image (2.5 x 3 mm^2) was acquired in ~30s.

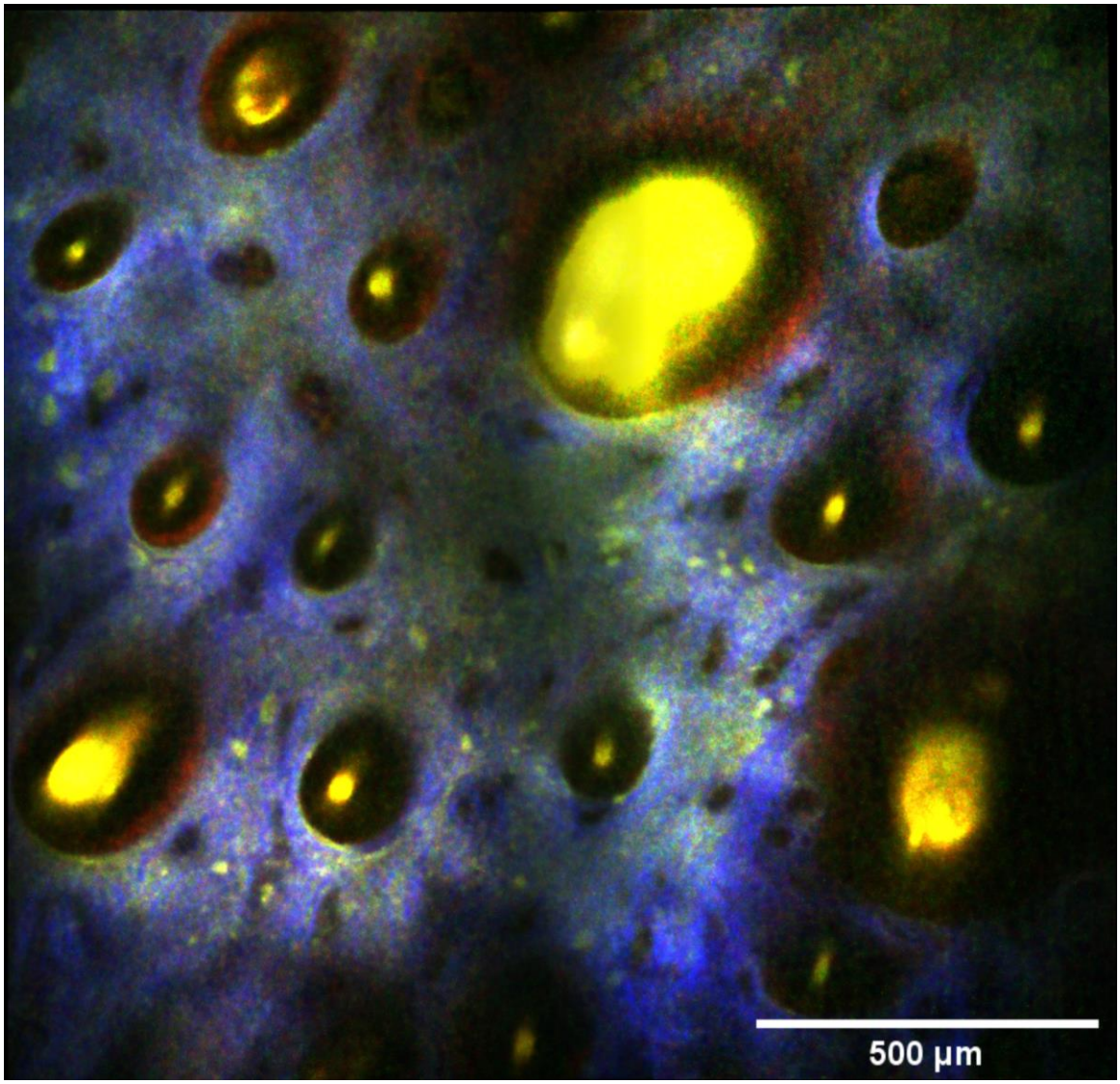

Figure 5.9. Millimeter scale, sub-micron resolution, time-resolved SPC *in vivo* MPM imaging of human facial skin. Tile mosaic image (1.5 x 1.5 mm^2) acquired 100 µm below the skin surface in the dermis. The image shows normal skin morphology at this depth mainly consisting of collagen fibers (blue), elastin fibers (green), and hair shafts (yellow).

6.5 Discussion

In this chapter, we demonstrate a compact imaging platform based on label-free multiphoton microscopy optimized for rapid multi-scale imaging of skin tissue, providing sub-micron resolution high contrast images.

One main challenge to overcome in multiphoton microscopy is maintaining high spatial resolution while optimizing scanning area and speed. The high numerical aperture objective and the custom optical design of our imaging platform provide millimeter-scale images at sub-micron resolution[65]. The millimeter-scale areas are scanned rapidly at micron resolution, sufficiently high to allow visualization of the cellular and fibrillar structures. This performance element is critical in the ability of the exoscope to emulate the current histological examination method, where the pathologist examines the entire tissue at low magnification and then zooms in for careful investigation of selected regions of interest.

Molecular contrast is the key benefit of MPM when compared to other high-resolution imaging techniques currently utilized for clinical skin imaging such as reflectance confocal microscopy. The molecular contrast, commonly provided in MPM skin imaging by the intensity of the endogenous fluorescence signals, can be significantly enhanced through approaches such as fluorescence lifetime imaging (FLIM). FLIM has been demonstrated to be valuable for many applications related to label-free skin imaging in humans[101] and animal models[146]. Although the conventional approach, TCSPC, enables acquisition of fluorescence lifetime decays with high temporal resolution, hundreds of photons per pixel[146] are required for accurate lifetime decay curve representations of fluorophores in the skin, which leads to long integration times. TCSPC imaging of skin in humans and animal models has been commonly performed at 250 ps temporal resolution

and 25 s [101] to 60 s [146] integration time per 256 × 256 pixel frame. These values would translate into hundreds of minutes of acquisition time for megapixel size images as required for imaging millimeter skin tissue areas. One solution we found for enhancing the intensity-based molecular contrast of the FLAME imaging platform without compromising speed, was to integrate time resolved SPC detection with reduced temporal resolution (390 ps) and time bins selected and grouped in such a way to allow selective discrimination of just one key endogenous fluorophore in skin, melanin. This approach is facilitated by the characteristically short fluorescence lifetime of a melanin component[101,142,143] probably eumelanin[61], with respect to the other endogenous fluorophores in skin. Selective detection of melanin is essential in distinguishing dermal melanocytes and melanophages from other cellular components and in applications such as pigmented lesions diagnosis and therapy assessment of pigmentary skin disorders requiring quantitative assessment of melanin. A benefit of using FLAME as an imaging tool as an aid in melanoma diagnosis and for therapy guiding of pigmentary skin disorders is related to its unique ability to provide in real-time, a volumetric mapping of melanin as demonstrated by the images we acquired *ex vivo* and *in vivo* in human skin. Rapid access to a volumetric assessment of melanin distribution in skin is expected to expedite and enhance the accuracy of its quantitative assessment, a particularly important tool for diagnosis and therapy guiding of pigmentary skin disorders[147] and for characterizing and understanding of pigment biology[62]. In addition to this, millimeter sized FOV's allow for more accurate quantification of epidermal melanin content which could be used in further studies to follow the skins response to UV exposure and evaluate UV therapy response.

Of note, literature values of epidermal melanin content are generally lower than the 6-50% reported in this work. For example, Saager et al. found that for all skin types, melanin volume fractions in the forearm and upper arm ranged from 5-20% using MPM and spatial frequency

domain spectroscopy[62]. Verdel et al. used an inverse model based on pulsed photothermal radiometry and diffuse reflectance spectroscopy measurements to calculate the melanin content in the epidermis of Fitzpatrick type II skin and found values in the 1.3-1.9% range[148]. Discrepancies between FLAME melanin volume fractions and other methods may be due to the way the calculation is carried out: the FLAME allows for selective melanin detection and larger field-of-views than commercial MPM systems. For example, melanin volume fractions calculated based on images acquired with the MPTflex does not separate out melanin from other skin fluorophores and relies on image thresholding to separate out the melanin signal using pixel intensities. With FLAME, no thresholding is necessary; all the pixels that contain more signal contributions from melanin than other fluorophores are all counted equally in the calculation. This thresholding could lead to variable melanin volume fractions since the detected signal intensity depends on many variables including laser power used, and scattering in the skin. In addition, based on the images presented in the literature acquired with the small field of view (i.e. $200 \times 200\ \mu m^2$) MPM device for the purpose of melanin content assessment, they are always acquired from areas located between skin folds and hair follicles to facilitate a more straightforward analysis. Through this approach only the cellular features of the epidermis are sampled, which may lead to another source of variation in the reported melanin volume fractions, as all of the non-melanin components in skin folds are not taken into account. Future research must be completed to better understand the effects of larger field-of-views and selective melanin imaging on MPM-based melanin content calculations.

We also demonstrated the design and implementation of two reliable *in vivo* patient-interfaces that allow for stable MPM imaging over millimeter-scales. All connections from the FLAME device housing to the glass window fixed on the skin to be imaged must be sturdy and

secure to prevent motion artifacts during imaging, but readily detachable once imaging is complete. In our design, a glass window is fixed to the skin with a light adhesive, and since the skin is highly elastic and the glass window is connected to the stages in the device housing in a robust manner, movement of the window by the stages results in a lateral displacement of the superficial tissue layers. This constitutes a safe and simple way for lateral scanning without physically displacing the imaging head itself. Future research will be necessary to characterize the precise motion artifacts introduced by the connection of the device to the skin in difficult imaging locations, such as the face or back.

In conclusion, we test the capability of a compact, multiphoton microscopy-based imaging platform, FLAME, highly optimized for rapid, label-free macroscopic imaging of skin with microscopic resolution and high contrast. It has the ability to provide 3D images encompassing sub-millimeter to millimeter scale areas of skin tissue within minutes and allows fast discrimination and 3D virtual staining of melanin. This unique combination of features provides the FLAME imaging platform with highly optimized functionality and facilitates a seamless conversion to a portable device for rapid, multi-scale skin characterization with high resolution to learn more about skin biology and disease.

5.6 Main findings and significance

- Using time-binning of detected photons, the FLAME imaging platform accurately and selectively detects melanin in human skin. This is important for the characterization and understanding of pigment biology, and may be used as a tool for diagnosis and therapy guiding of pigmentary skin disorders.

- Human skin exhibits heterogeneous melanin content that is accurately characterized using larger than millimeter sized assessment volumes. Rapid, accurate melanin quantification can be used to assess the skin's response to UV light or to evaluate therapy response.
- Reliable *in vivo* imaging with FLAME over millimeter-sized areas can be accomplished and requires a stable patient interface. This is important for further adoption of this technology as a practical device for studying skin biology and disease.

6. Conclusions and future directions

Human skin is a highly complex and dynamic biological material vital for the preservation of homeostasis. Thus, a multi-scale analysis with subcellular resolution performed without harming the skin is necessary to obtain a robust characterization of the structure and function involved in this homeostasis. Recent advances in optical imaging technologies, specifically in multiphoton microscopy, have made this type of study feasible. In this dissertation, three applications of *in vivo* noninvasive characterization of skin are described and contrasted with conventional methods. In addition, further advancements to the technology are demonstrated with the goal of motivating more widespread adoption for use in the study of skin biology, skin disease, and skin treatment effects monitoring.

The main application described was the characterization of skin cellular structure and function in vitiligo. Using MPM, we found altered cellular metabolism in vitiligo compared to normal skin before treatment initiation according to mitochondrial clustering analysis performed on *in vivo* images, and: (1) a return to normal cellular metabolism in vitiligo skin that exhibited repigmentation after treatment, (2) a continuation of altered metabolism in vitiligo patients that did not exhibit repigmentation. Single-cell RNA sequencing analysis revealed a sub-population of stressed keratinocytes in vitiligo skin not present in normal skin, in agreement with the MPM findings. We were also able to track active dendritic melanocytes after vitiligo treatment, the results of which showed that when repigmentation does not occur after treatment, the reason is that the melanocytes do not migrate out and repigment the vitiligo skin. These results provide evidence for a potential link between stressed keratinocytes and vitiligo persistence and a rationale for

targeting stressed keratinocytes as a treatment strategy in vitiligo. Important questions remain, such as when the stressed keratinocytes arise during the depigmentation process in vitiligo and how different treatment modalities affect the stressed keratinocyte populations. Future studies on the immune response after treatment may help elucidate the reason behind vitiligo treatment failure in some patients.

The second application was the characterization of the cytological and morphological features in benign nevi visualized by *in vivo* MPM. The main features described in the benign nevi were: larger nevomelanocytes and nevomelanocyte nuclei in intradermal nevi compared to junctional and compound nevi, similar nevomelanocyte nest sizes (20-80 μm) in all three types of nevi, and elongated rete ridges. These features are a compliment to the features previously described in melanoma and can be used in the process of discriminating melanoma from simulants by *in vivo* imaging. We also found the percentage of nevomelanocytes located outside nests was quite small in the studied nevi. An increase in the percentage of nevomelanocytes outside nests may be a helpful metric in future studies assessing nevi in evolution to become melanoma. In addition to this, an immune response in the *in vivo* images was visualized in two forms: (1) irregularly shaped cells, 18-20 μm in size, exhibiting bright fluorescence, most likely melanophages, and (2) cells with a round in shape, 10-12 μm in size, and arranged in clusters, most likely T cells. Cellular morphology of these cells correlated with histopathology and immunohistochemistry. Visualization of an immune response *in vivo* in nevi could be used in future studies as a biomarker related to response to immunotherapies. These results illustrate and discuss qualitative and quantitative metrics in benign nevi that complement those previously described in melanoma and may be relevant in future studies for assessing nevi in evolution to become melanoma or in distinguishing benign nevi from early stage melanoma. Future studies

following nevi over a period of a few years to more fully understand the nevi that evolve to melanoma are a necessary step in the more widespread use of this technology for melanoma detection.

The third application was an evaluation of the skin condition melasma to more accurately differentiate between melasma sub-types *in vivo* noninvasively. We found that basal keratinocytes in melasma have a pigment distribution localized towards the cellular membrane and generally lack the melanin caps that provide photoprotection in normal skin. This reduced photoprotection appears to be associated with more pronounced dermal photodamage (elastosis) compared to skin with perilesional skin with melanin caps. This finding motivates future studies to determine whether an altered distribution of melanin plays a role in the pathogenesis of melasma. Another finding was the sign of a prior inflammatory response in melasma captured by MPM, in the form of melanophages in the dermis. This was an uncertainty before the study due to the limited penetration depth of MPM. Lastly, we found that epidermal melasma is characterized by significantly higher amounts of epidermal melanin compared to perilesional skin, while dermal/mixed melasma presents a similar pigment amount in both melasma and perilesional skin, a result that has been speculated about based on visual assessment. These results demonstrate the ability of MPM to characterize melasma and potentially differentiate between the sub-types, although an expanded study is necessary to fully test this hypothesis and advance the understanding of the condition.

The final chapter of the dissertation was dedicated to the description of two main components of the enhanced MPM imaging platform recently developed in our lab. The first component was an improvement in signal detection sensitivity resulting in the separation of melanin from the other skin fluorophores based on its short fluorescence lifetime. This separation

lead to enhanced accuracy and sensitivity of the melanin content measurement in volunteers with different skin types. The second component was the engineering of a reliable patient-interface connecting the FLAME imaging head to the skin to be imaged. Two iterations were described that allowed for *in vivo* mosaic imaging to obtain a 3×3 mm^2 field-of-view with minimal motion artifacts. In conclusion, these advances support the highly optimized functionality of the FLAME imaging platform and facilitate a seamless conversion to a portable device for rapid, multi-scale skin characterization with high resolution to learn more about skin biology and disease.

References

1. Titford, M. A Short History of Histopathology Technique. *Journal of Histotechnology* **29**, 99-110 (2006).
2. Mukhopadhyay, A.K. On the History of Classification in Dermatology. *Indian J Dermatol* **61**, 588-592 (2016).
3. Malissen, B., Tamoutounour, S. & Henri, S. The origins and functions of dendritic cells and macrophages in the skin. *Nat Rev Immunol* **14**, 417-428 (2014).
4. Ariotti, S., *et al.* T cell memory. Skin-resident memory $CD8^+$ T cells trigger a state of tissue-wide pathogen alert. *Science* **346**, 101-105 (2014).
5. Hoath, S.B. & Leahy, D.G. The organization of human epidermis: functional epidermal units and phi proportionality. *J Invest Dermatol* **121**, 1440-1446 (2003).
6. Abdel-Malek, Z., *et al.* Analysis of the UV-Induced Melanogenesis and Growth Arrest of Human Melanocytes. *Pigment Cell Research* **7**, 326-332 (1994).
7. Hirobe, T. Keratinocytes regulate the function of melanocytes. *Special Issue: Pigmentary Disorders-Bringing Colors to Our Specialty* **32**, 200-204 (2014).
8. Lo Cicero, A., *et al.* Exosomes released by keratinocytes modulate melanocyte pigmentation. *Nat Commun* **6**, 7506 (2015).
9. Su, Q. & Igyártó, B.Z. Keratinocytes Share Gene Expression Fingerprint with Epidermal Langerhans Cells via mRNA Transfer. *J Invest Dermatol* **139**, 2313-2323.e2318 (2019).
10. James, W.D., Berger, T.G., Elston, D.M. & Neuhaus, I.M. *Andrews' Diseases of the Skin: Clinical Dermatology*, (Elsevier, 2016).
11. Monnier, V.M., *et al.* Relation between complications of type I diabetes mellitus and collagen-linked fluorescence. *N Engl J Med* **314**, 403-408 (1986).
12. Lyons, T.J., Bailie, K.E., Dyer, D.G., Dunn, J.A. & Baynes, J.W. Decrease in skin collagen glycation with improved glycemic control in patients with insulin-dependent diabetes mellitus. *J Clin Invest* **87**, 1910-1915 (1991).
13. Tong, P.L., *et al.* A quantitative approach to histopathological dissection of elastin-related disorders using multiphoton microscopy. *Br J Dermatol* **169**, 869-879 (2013).
14. Mehrabi, J.N., Doong, J., Lentsch, G. & Mesinkovska, N. Imaging of in vivo pseudoxanthoma elasticum via multiphoton microscopy and optical coherence tomography. *JAAD Case Rep* **6**, 702-704 (2020).
15. Goldman, L. Some investigative studies of pigmented nevi with cutaneous microscopy. *J Invest Dermatol* **16**, 407-427 (1951).
16. Vestergaard, M.E., Macaskill, P., Holt, P.E. & Menzies, S.W. Dermoscopy compared with naked eye examination for the diagnosis of primary melanoma: a meta-analysis of studies performed in a clinical setting. *British Journal of Dermatology* **159**, 669-676 (2008).
17. Antonio, J.R., *et al.* Correlation between dermoscopic and histopathological diagnoses of atypical nevi in a dermatology outpatient clinic of the Medical School of São José do Rio Preto, SP, Brazil. *An Bras Dermatol* **88**, 199-203 (2013).
18. Gilchrest, B.A., Fitzpatrick, T.B., Anderson, R.R. & Parrish, J.A. Localization of malanin pigmentation in the skin with Wood's lamp. *Br J Dermatol* **96**, 245-248 (1977).
19. Grimes, P.E., Yamada, N. & Bhawan, J. Light Microscopic, Immunohistochemical, and Ultrastructural Alterations in Patients with Melasma. *American Journal of Dermatopathology* **27**, 96-101 (2005).

20. Lawrence, N., Cox, S.E. & Brody, H.J. Treatment of melasma with Jessner's solution versus glycolic acid: A comparison of clinical efficacy and evaluation of the predictive ability of Wood's light examination. **36**, 589-593 (1997).
21. Bancroft, J.D. & Gamble, M. *Theory and practice of histological techniques*, (Elsevier health sciences, 2008).
22. Bos, J.D., *et al.* The skin immune system (SIS): distribution and immunophenotype of lymphocyte subpopulations in normal human skin. *J Invest Dermatol* **88**, 569-573 (1987).
23. Bos, J.D., *et al.* T-Cell Receptor γδ Bearing Cells in Normal Human Skin. **94**, 37-42 (1990).
24. Balu, M., *et al.* Distinguishing between benign and malignant melanocytic nevi by in vivo multiphoton microscopy. *Cancer Res* **74**, 2688-2697 (2014).
25. Kubanov, A., Proshutinskaia, D., Volnukhin, V., Katunina, O. & Abramova, T. Immunohistochemical analysis of melanocyte content in different zones of vitiligo lesions using the Melan-A marker. *Acta Dermatovenerol Alp Pannonica Adriat* **25**, 5-9 (2016).
26. Kelemen, K., White, C.R., Gatter, K., Braziel, R.M. & Fan, G. Immunophenotypic correlation between skin biopsy and peripheral blood findings in mycosis fungoides. *Am J Clin Pathol* **134**, 739-748 (2010).
27. Haymaker, C., *et al.* The Role of the Immune System and Immunoregulatory Mechanisms Relevant to Melanoma. in *Genetics of Melanoma* (eds. Torres-Cabala, C.A. & Curry, J.L.) 31-65 (Springer New York, New York, NY, 2016).
28. Richmond, J.M., Frisoli, M.L. & Harris, J.E. Innate immune mechanisms in vitiligo: danger from within. *Curr Opin Immunol* **25**, 676-682 (2013).
29. Balch, C.M., *et al.* Final version of 2009 AJCC melanoma staging and classification. *J Clin Oncol* **27**, 6199-6206 (2009).
30. Bağcı, I.S., *et al.* Effects of Short-Term Moisturizer Application in Different Ethnic Skin Types: Noninvasive Assessment with Optical Coherence Tomography and Reflectance Confocal Microscopy. *Skin Pharmacol Physiol* **31**, 125-133 (2018).
31. Minsky, M. Memoir on inventing the confocal scanning microscope. *Scanning* **10**, 128-138 (1988).
32. Rajadhyaksha, M., Grossman, M., Esterowitz, D., Webb, R.H. & Anderson, R.R. In vivo confocal scanning laser microscopy of human skin: melanin provides strong contrast. *J Invest Dermatol* **104**, 946-952 (1995).
33. Busam, K.J., Charles, C., Lee, G. & Halpern, A.C. Morphologic Features of Melanocytes, Pigmented Keratinocytes, and Melanophages by In Vivo Confocal Scanning Laser Microscopy. *Mod Pathol* **14**, 862-868 (2001).
34. Xiong, Y.D., *et al.* A meta-analysis of reflectance confocal microscopy for the diagnosis of malignant skin tumours. *J Eur Acad Dermatol Venereol* **30**, 1295-1302 (2016).
35. Xiong, Y.Q., *et al.* Comparison of dermoscopy and reflectance confocal microscopy for the diagnosis of malignant skin tumours: a meta-analysis. *J Cancer Res Clin Oncol* **143**, 1627-1635 (2017).
36. Borsari, S., *et al.* Clinical Indications for Use of Reflectance Confocal Microscopy for Skin Cancer Diagnosis. *JAMA Dermatol* **152**, 1093-1098 (2016).
37. Stevenson, A.D., Mickan, S., Mallett, S. & Ayya, M. Systematic review of diagnostic accuracy of reflectance confocal microscopy for melanoma diagnosis in patients with clinically equivocal skin lesions. *Dermatology practical & conceptual* **3**, 19-27 (2013).

38. Hashemi, P., *et al.* Langerhans cells and melanocytes share similar morphologic features under in vivo reflectance confocal microscopy: a challenge for melanoma diagnosis. *J Am Acad Dermatol* **66**, 452-462 (2012).
39. Nehal, K.S., Gareau, D. & Rajadhyaksha, M. Skin imaging with reflectance confocal microscopy. *Semin Cutan Med Surg* **27**, 37-43 (2008).
40. Raphael, A.P. & Prow, T.W. Clinical Cutaneous Drug Delivery Assessment Using Single and Multiphoton Microscopy. in *Percutaneous Penetration Enhancers Drug Penetration Into/Through the Skin: Methodology and General Considerations* (eds. Dragicevic, N. & I. Maibach, H.) 283-302 (Springer Berlin Heidelberg, Berlin, Heidelberg, 2017).
41. Hales, J.M. Chemical structure-nonlinear optical property relationships for a series of two-photon absorbing fluorene molecules. (2004).
42. Birge, R.R. & Pierce, B.M. Semiclassical time-dependent theory of two-photon spectroscopy. The effect of dephasing in the virtual level on the two-photon excitation spectrum of isotachysterol. *International Journal of Quantum Chemistry* **29**, 639-656 (1986).
43. Freund I Fau - Deutsch, M. & Deutsch, M. Second-harmonic microscopy of biological tissue.
44. Williams, R.M., Zipfel Wr Fau - Webb, W.W. & Webb, W.W. Multiphoton microscopy in biological research. (2001).
45. Campagnola, P.J., *et al.* Three-dimensional high-resolution second-harmonic generation imaging of endogenous structural proteins in biological tissues.
46. Dombeck, D.A., *et al.* Uniform polarity microtubule assemblies imaged in native brain tissue by second-harmonic generation microscopy.
47. Zipfel, W.R., *et al.* Live tissue intrinsic emission microscopy using multiphoton-excited native fluorescence and second harmonic generation. *Proc Natl Acad Sci U S A* **100**, 7075-7080 (2003).
48. Diaspro, A., Chirico, G. & Collini, M. Two-photon fluorescence excitation and related techniques in biological microscopy. *Q Rev Biophys* **38**, 97-166 (2005).
49. Piston, D.W., Masters, B.R. & Webb, W.W. Three-dimensionally resolved NAD(P)H cellular metabolic redox imaging of the in situ cornea with two-photon excitation laser scanning microscopy. *J Microsc* **178**, 20-27 (1995).
50. Xu, C., Williams, R.M., Zipfel, W. & Webb, W.W. Multiphoton excitation cross-sections of molecular fluorophores. *Bioimaging* **4**, 198-207 (1996).
51. Teuchner, K., *et al.* Femtosecond two-photon excited fluorescence of melanin. *Photochem Photobiol* **70**, 146-151 (1999).
52. Pena, A., Strupler, M., Boulesteix, T. & Schanne-Klein, M. Spectroscopic analysis of keratin endogenous signal for skin multiphoton microscopy. *Opt Express* **13**, 6268-6274 (2005).
53. Zoumi, A., Yeh, A. & Tromberg, B.J. Imaging cells and extracellular matrix in vivo by using second-harmonic generation and two-photon excited fluorescence. *Proc Natl Acad Sci U S A* **99**, 11014-11019 (2002).
54. Li, C., *et al.* Imaging leukocyte trafficking in vivo with two-photon-excited endogenous tryptophan fluorescence. *Opt Express* **18**, 988-999 (2010).
55. Koenig, K., *et al. Optical tomography of human skin with subcellular spatial and picosecond time resolution using intense near infrared femtosecond laser pulses*, (SPIE, 2002).

56. Balu, M., *et al.* In Vivo Multiphoton Microscopy of Basal Cell Carcinoma. *JAMA Dermatol* **151**, 1068-1074 (2015).
57. Pouli, D., *et al.* Imaging mitochondrial dynamics in human skin reveals depth-dependent hypoxia and malignant potential for diagnosis. *Sci Transl Med* **8**, 367ra169 (2016).
58. Lentsch, G., *et al.* Non-invasive optical biopsy by multiphoton microscopy identifies the live morphology of common melanocytic nevi. *Pigment Cell Melanoma Res* **33**, 869-877 (2020).
59. Balu, M., *et al.* In vivo multiphoton NADH fluorescence reveals depth-dependent keratinocyte metabolism in human skin. *Biophys J* **104**, 258-267 (2013).
60. Koehler, M.J., König, K., Elsner, P., Bückle, R. & Kaatz, M. In vivo assessment of human skin aging by multiphoton laser scanning tomography. *Opt Lett* **31**, 2879-2881 (2006).
61. Krasieva, T.B., *et al.* Two-photon excited fluorescence lifetime imaging and spectroscopy of melanins in vitro and in vivo. *J Biomed Opt* **18**, 31107 (2013).
62. Saager, R.B., *et al.* In vivo measurements of cutaneous melanin across spatial scales: using multiphoton microscopy and spatial frequency domain spectroscopy. *J Biomed Opt* **20**, 066005 (2015).
63. Bazin, R., *et al.* Clinical study on the effects of a cosmetic product on dermal extracellular matrix components using a high-resolution multiphoton tomograph. *Skin Res Technol* **16**, 305-310 (2010).
64. Lademann, J., *et al.* In vivo methods for the analysis of the penetration of topically applied substances in and through the skin barrier. *Int J Cosmet Sci* **34**, 551-559 (2012).
65. Balu, M., Mikami, H., Hou, J., Potma, E.O. & Tromberg, B.J. Rapid mesoscale multiphoton microscopy of human skin. *Biomed Opt Express* **7**, 4375-4387 (2016).
66. Rodrigues, M., *et al.* New discoveries in the pathogenesis and classification of vitiligo. *J Am Acad Dermatol* **77**, 1-13 (2017).
67. van den Boorn, J.G., *et al.* Autoimmune destruction of skin melanocytes by perilesional T cells from vitiligo patients. *J Invest Dermatol* **129**, 2220-2232 (2009).
68. Frisoli, M.L., Essien, K. & Harris, J.E. Vitiligo: Mechanisms of Pathogenesis and Treatment. *Annu Rev Immunol* **38**, 621-648 (2020).
69. Strassner, J.P., Rashighi, M., Ahmed Refat, M., Richmond, J.M. & Harris, J.E. Suction blistering the lesional skin of vitiligo patients reveals useful biomarkers of disease activity. *J Am Acad Dermatol* **76**, 847-855.e845 (2017).
70. Regazzetti, C., *et al.* Transcriptional Analysis of Vitiligo Skin Reveals the Alteration of WNT Pathway: A Promising Target for Repigmenting Vitiligo Patients. *J Invest Dermatol* **135**, 3105-3114 (2015).
71. Harris, J.E., *et al.* A mouse model of vitiligo with focused epidermal depigmentation requires IFN-γ for autoreactive $CD8^+$ T-cell accumulation in the skin. *J Invest Dermatol* **132**, 1869-1876 (2012).
72. Riding, R.L., Richmond, J.M. & Harris, J.E. Mouse Model for Human Vitiligo. *Curr Protoc Immunol* **124**, e63 (2019).
73. Richmond, J.M., *et al.* Keratinocyte-Derived Chemokines Orchestrate T-Cell Positioning in the Epidermis during Vitiligo and May Serve as Biomarkers of Disease. *J Invest Dermatol* **137**, 350-358 (2017).
74. Pérez-Guijarro, E., Day, C.P., Merlino, G. & Zaidi, M.R. Genetically engineered mouse models of melanoma. *Cancer* **123**, 2089-2103 (2017).

75. Whitton, M.E., *et al.* Interventions for vitiligo. *Cochrane Database Syst Rev*, CD003263 (2015).
76. Kishan Kumar, Y.H., Rao, G.R., Gopal, K.V., Shanti, G. & Rao, K.V. Evaluation of narrow-band UVB phototherapy in 150 patients with vitiligo. *Indian J Dermatol Venereol Leprol* **75**, 162-166 (2009).
77. Nishimura, E.K., *et al.* Dominant role of the niche in melanocyte stem-cell fate determination. *Nature* **416**, 854 (2002).
78. Chou, W.C., *et al.* Direct migration of follicular melanocyte stem cells to the epidermis after wounding or UVB irradiation is dependent on Mc1r signaling. *Nature Medicine* **19**, 924 (2013).
79. Goldstein, N.B., *et al.* Narrow Band Ultraviolet B Treatment for Human Vitiligo Is Associated with Proliferation, Migration, and Differentiation of Melanocyte Precursors. *J Invest Dermatol* **135**, 2068-2076 (2015).
80. Matin, R. Vitiligo in adults and children: surgical interventions. *BMJ Clinical Evidence* **2015**, 1717 (2015).
81. Xylas, J., *et al.* Noninvasive assessment of mitochondrial organization in three-dimensional tissues reveals changes associated with cancer development. *Int J Cancer* **136**, 322-332 (2015).
82. Xylas, J., Quinn, K.P., Hunter, M. & Georgakoudi, I. Improved Fourier-based characterization of intracellular fractal features. *Opt Express* **20**, 23442-23455 (2012).
83. Zhang, L. & Nie, Q. scMC learns biological variation through the alignment of multiple single-cell genomics datasets. *Genome Biol* **22**, 10 (2021).
84. Dorrity, M.W., Saunders, L.M., Queitsch, C., Fields, S. & Trapnell, C. Dimensionality reduction by UMAP to visualize physical and genetic interactions. *Nat Commun* **11**, 1537 (2020).
85. Lessard, J.C., *et al.* Keratin 16 regulates innate immunity in response to epidermal barrier breach. *Proc Natl Acad Sci U S A* **110**, 19537-19542 (2013).
86. Rotty, J.D. & Coulombe, P.A. A wound-induced keratin inhibits Src activity during keratinocyte migration and tissue repair. *J Cell Biol* **197**, 381-389 (2012).
87. Boniface, K., *et al.* Vitiligo Skin Is Imprinted with Resident Memory CD8 T Cells Expressing CXCR3. *J Invest Dermatol* **138**, 355-364 (2018).
88. Rashighi, M., *et al.* CXCL10 is critical for the progression and maintenance of depigmentation in a mouse model of vitiligo. *Sci Transl Med* **6**, 223ra223 (2014).
89. Dubois, A., Gopee, N., Olabi, B. & Haniffa, M. Defining the Skin Cellular Community Using Single-Cell Genomics to Advance Precision Medicine. *J Invest Dermatol* **141**, 255-264 (2021).
90. Suvà, M.L. & Tirosh, I. Single-Cell RNA Sequencing in Cancer: Lessons Learned and Emerging Challenges. *Mol Cell* **75**, 7-12 (2019).
91. Yeh, I. New and evolving concepts of melanocytic nevi and melanocytomas. *Mod Pathol* **33**, 1-14 (2020).
92. Elder, D.E. Precursors to melanoma and their mimics: nevi of special sites. *Mod Pathol* **19 Suppl 2**, S4-20 (2006).
93. Erdei, E. & Torres, S.M. A new understanding in the epidemiology of melanoma. *Expert Rev Anticancer Ther* **10**, 1811-1823 (2010).
94. Henley, S.J., *et al.* Annual report to the nation on the status of cancer, part I: National cancer statistics. *Cancer* **126**, 2225-2249 (2020).

95. Dimitriou, F., *et al.* The World of Melanoma: Epidemiologic, Genetic, and Anatomic Differences of Melanoma Across the Globe. *Curr Oncol Rep* **20**, 87 (2018).
96. Farmer, E.R., Gonin, R. & Hanna, M.P. Discordance in the histopathologic diagnosis of melanoma and melanocytic nevi between expert pathologists. *Hum Pathol* **27**, 528-531 (1996).
97. Lodha, S., Saggar, S., Celebi, J.T. & Silvers, D.N. Discordance in the histopathologic diagnosis of difficult melanocytic neoplasms in the clinical setting. *J Cutan Pathol* **35**, 349-352 (2008).
98. Shoo, B.A., Sagebiel, R.W. & Kashani-Sabet, M. Discordance in the histopathologic diagnosis of melanoma at a melanoma referral center. *J Am Acad Dermatol* **62**, 751-756 (2010).
99. Arginelli, F., *et al.* High resolution diagnosis of common nevi by multiphoton laser tomography and fluorescence lifetime imaging. *Skin Res Technol* **19**, 194-204 (2013).
100. Dimitrow, E., *et al.* Sensitivity and specificity of multiphoton laser tomography for in vivo and ex vivo diagnosis of malignant melanoma. *J Invest Dermatol* **129**, 1752-1758 (2009).
101. Seidenari, S., *et al.* Multiphoton laser tomography and fluorescence lifetime imaging of melanoma: morphologic features and quantitative data for sensitive and specific non-invasive diagnostics. *PLoS One* **8**, e70682 (2013).
102. Mackie, R. Melanocytic naevi and malignant melanoma. *Textbook of dermatology*, 1525-1560 (1992).
103. Schneider, C.A., Rasband, W.S. & Eliceiri, K.W. NIH Image to ImageJ: 25 years of image analysis. *Nat Methods* **9**, 671-675 (2012).
104. Massi, G. & LeBoit, P.E. *Histological diagnosis of nevi and melanoma,* (Springer Science & Business Media, 2013).
105. Pellacani, G., Cesinaro, A.M. & Seidenari, S. In vivo assessment of melanocytic nests in nevi and melanomas by reflectance confocal microscopy. *Mod Pathol* **18**, 469-474 (2005).
106. Koh, S.S. & Cassarino, D.S. Immunohistochemical Expression of p16 in Melanocytic Lesions: An Updated Review and Meta-analysis. *Arch Pathol Lab Med* **142**, 815-828 (2018).
107. Price, N.M., Rywlin, A.M. & Ackerman, A.B. Histologic criteria for the diagnosis of superficial spreading malignant melanoma: formulated on the basis of proven metastatic lesions. *Cancer* **38**, 2434-2441 (1976).
108. Fox, J.C., Reed, J.A. & Shea, C.R. The recurrent nevus phenomenon: a history of challenge, controversy, and discovery. *Arch Pathol Lab Med* **135**, 842-846 (2011).
109. Linck, R.D.M., Costa, R.L.P. & Garicochea, B. Cancer immunology and melanoma immunotherapy. *An Bras Dermatol* **92**, 830-835 (2017).
110. Balu, M., Saytashev, I., Hou, J., Dantus, M. & Tromberg, B.J. Sub-40 fs, 1060-nm Yb-fiber laser enhances penetration depth in nonlinear optical microscopy of human skin. *J Biomed Opt* **20**, 120501 (2015).
111. Tang, S., Krasieva, T.B., Chen, Z., Tempea, G. & Tromberg, B.J. Effect of pulse duration on two-photon excited fluorescence and second harmonic generation in nonlinear optical microscopy. Vol. 11 3 (SPIE, 2006).
112. Ji, N., Sato, T.R. & Betzig, E. Characterization and adaptive optical correction of aberrations during in vivo imaging in the mouse cortex. *Proc Natl Acad Sci U S A* **109**, 22-27 (2012).

113. Passeron, T. Melasma pathogenesis and influencing factors - an overview of the latest research. *J Eur Acad Dermatol Venereol* **27 Suppl 1**, 5-6 (2013).
114. Lee, A.Y. Recent progress in melasma pathogenesis. *Pigment Cell Melanoma Res* **28**, 648-660 (2015).
115. Moin, A., Jabery, Z. & Fallah, N. Prevalence and awareness of melasma during pregnancy. *Int J Dermatol* **45**, 285-288 (2006).
116. Handel, A.C., Lima, P.B., Tonolli, V.M., Miot, L.D. & Miot, H.A. Risk factors for facial melasma in women: a case-control study. *Br J Dermatol* **171**, 588-594 (2014).
117. Tamega, A.e.A., *et al.* Clinical patterns and epidemiological characteristics of facial melasma in Brazilian women. *J Eur Acad Dermatol Venereol* **27**, 151-156 (2013).
118. Goh, C.L. & Dlova, C.N. A retrospective study on the clinical presentation and treatment outcome of melasma in a tertiary dermatological referral centre in Singapore. *Singapore Medical Journal* **40**, 455-458 (1999).
119. Achar, A. & Rathi, S.K. Melasma: a clinico-epidemiological study of 312 cases. *Indian J Dermatol* **56**, 380-382 (2011).
120. Takeda, K., *et al.* Induction of melanocyte-specific microphthalmia-associated transcription factor by Wnt-3a. *J Biol Chem* **275**, 14013-14016 (2000).
121. Hsieh, J.C., *et al.* A new secreted protein that binds to Wnt proteins and inhibits their activities. *Nature* **398**, 431-436 (1999).
122. Kim, J.Y., Lee, T.R. & Lee, A.Y. Reduced WIF-1 expression stimulates skin hyperpigmentation in patients with melasma. *J Invest Dermatol* **133**, 191-200 (2013).
123. Sonthalia, S., Jha, A.K. & Langar, S. Dermoscopy of Melasma. *Indian Dermatology Online Journal* **8**, 525-526 (2017).
124. Sgouros , D., Pellacani, G., Katoulis, A., Rigopoulos, D. & Longo, C. Confocal Microscopy in Diagnosis and Management of Melasma: Review of Literature. *Pigmentary Disorders* **S1**(2014).
125. Kang, H.Y., *et al.* In vivo reflectance confocal microscopy detects pigmentary changes in melasma at a cellular level resolution. **19**, e228-e233 (2010).
126. Liu, H., *et al.* Histological classification of melasma with reflectance confocal microscopy: a pilot study in Chinese patients. *Skin Research and Technology* **17**, 398-403 (2011).
127. Ardigo, M., Cameli, N., Berardesca, E. & Gonzalez, S. Characterization and evaluation of pigment distribution and response to therapy in melasma using in vivo reflectance confocal microscopy: a preliminary study. *Journal of the European Academy of Dermatology and Venereology* **24**, 1296-1303 (2010).
128. Longo, C., Pellacani, G., Tourlaki, A., Galimberti, M. & Bencini, P.L. Melasma and low-energy Q-switched laser: treatment assessment by means of in vivo confocal microscopy. *Lasers in Medical Science* **29**, 1159-1163 (2014).
129. Goberdhan, L.T., Colvan, L., Makino, E.T., Aguilar, C. & Mehta, R.C. Assessment of a Superficial Chemical Peel Combined With a Multimodal, Hydroquinone-Free Skin Brightener Using In Vivo Reflectance Confocal Microscopy. *Journal of Drugs in Dermatology* **12**, s38-s41 (2013).
130. Bradley, D. & Roth, G. Adaptive Thresholding using the Integral Image. *Journal of Graphics Tools* **12**, 13-21 (2007).
131. Guitera, P., Li, L.L., Scolyer, R.A. & Menzies, S.W. Morphologic features of melanophages under in vivo reflectance confocal microscopy. **146**, 492-498 (2010).

132. Ochoa, M.T., Loncaric, A., Krutzik, S.R., Becker, T.C. & Modlin, R.L. "Dermal Dendritic Cells" Comprise Two Distinct Populations: CD1+ Dendritic Cells and CD209+ Macrophages. **128**, 2225-2231 (2008).
133. Majdzadeh, A., *et al.* Real-time visualization of melanin granules in normal human skin using combined multiphoton and reflectance confocal microscopy. *Photodermatology, Photoimmunology & Photomedicine* **31**, 141-148 (2015).
134. Pellacani, G., Longo, C., Malvehy, J. & et al. In vivo confocal microscopic and histopathologic correlations of dermoscopic features in 202 melanocytic lesions. **144**, 1597-1608 (2008).
135. Braverman, I.M. & Fonferko, E. Studies in Cutaneous Aging: I. The Elastic Fiber Network. *Journal of Investigative Dermatology* **78**, 434-443 (1982).
136. Kang, W.H., *et al.* Melasma: histopathological characteristics in 56 Korean patients. **146**, 228-237 (2002).
137. Torres-Álvarez, B., *et al.* Histochemical and Immunohistochemical Study in Melasma: Evidence of Damage in the Basal Membrane. *The American Journal of Dermatopathology* **33**, 291-295 (2011).
138. Brianezi, G., Handel, A.C., Schmitt, J.V., Miot, L.D.B. & Miot, H.A. Changes in nuclear morphology and chromatin texture of basal keratinocytes in melasma. *Journal of the European Academy of Dermatology and Venereology* **29**, 809-812 (2015).
139. Hernández-Barrera, R., Torres-Alvarez, B., Castanedo-Cazares, J.P., Oros-Ovalle, C. & Moncada, B. Solar elastosis and presence of mast cells as key features in the pathogenesis of melasma. **33**, 305-308 (2008).
140. Sarvjot, V., Sharma, S., Mishra, S. & Singh, A. Melasma: A clinicopathological study of 43 cases. *Indian Journal of Pathology and Microbiology* **52**, 357-359 (2009).
141. Fast, A., *et al.* Fast, large area multiphoton exoscope (FLAME) for macroscopic imaging with microscopic resolution of human skin. *Scientific reports* **10**, 1-14 (2020).
142. Dimitrow, E., *et al.* Spectral fluorescence lifetime detection and selective melanin imaging by multiphoton laser tomography for melanoma diagnosis. *Exp Dermatol* **18**, 509-515 (2009).
143. Dancik, Y., Favre, A., Loy, C.J., Zvyagin, A.V. & Roberts, M.S. Use of multiphoton tomography and fluorescence lifetime imaging to investigate skin pigmentation in vivo. *J Biomed Opt* **18**, 26022 (2013).
144. Chardon, A., Cretois, I. & Hourseau, C. Skin colour typology and suntanning pathways. *Int J Cosmet Sci* **13**, 191-208 (1991).
145. Jin, W., *et al. An iterative method to quantify epidermal melanin concentration using spatial frequency domain Imaging and a layered Monte Carlo model*, (SPIE, 2021).
146. Skala, M.C., *et al.* In vivo multiphoton microscopy of NADH and FAD redox states, fluorescence lifetimes, and cellular morphology in precancerous epithelia. *Proc Natl Acad Sci U S A* **104**, 19494-19499 (2007).
147. Lentsch, G., *et al.* In vivo multiphoton microscopy of melasma. *Pigment Cell Melanoma Res* **32**, 403-411 (2019).
148. Verdel, N., Lentsch, G., Balu, M., Tromberg, B.J. & Majaron, B. Noninvasive assessment of skin structure by combined photothermal radiometry and optical spectroscopy: coregistration with multiphoton microscopy. *Appl Opt* **57**, D117-D122 (2018).